



TECHNISCHE
UNIVERSITÄT
WIEN
Vienna | Austria

DISSERTATION

Study of the Damage Mechanisms and Limits of Superconducting Magnet Components due to Beam Impact

Ausgeführt zum Zwecke der Erlangung des akademischen Grades eines Doktors der
technischen Wissenschaften unter der Leitung von

PRIVATDOZ. DIPL.-ING. DR. TECHN. MICHAEL BENEDIKT

Institutsnummer: E141

Atominstitut der Österreichischen Universitäten

DR. DANIEL WOLLMANN

CERN, TE-MPE-PE

eingereicht an der Technischen Universität Wien
FAKULTÄT FÜR PHYSIK

von

VIVIEN RAGINEL

Matrikelnummer 1427067

Le Domaine Bat D, 226 rue de l'école, F-01280 Prevessin-Moëns

Wien, im Juni 2018

Abstract

The energy stored in the particle beams of an accelerator such as CERN's Large Hadron Collider (LHC) is substantial and requires a complex machine protection system to protect the equipment from damage. Despite efficient beam absorbers, several failure modes can lead to beam impact on superconducting magnets. The energy deposition from these beam losses can cause significant temperature rise and mechanical stress in the magnet coils, which can lead to a degradation of the insulation strength and critical current of the superconducting cables. An improved understanding of the damage mechanisms is important for the LHC when considering its planned increase in beam brightness, as well as for other accelerators using superconducting magnets.

In this thesis, for the first time the damage mechanisms and limits of Nb-Ti and Nb₃Sn superconducting magnet components are studied experimentally at room temperature. Several experiments have been performed to study the effect of heating over different time scales - hours, several seconds and tens of milliseconds - on the polyimide insulation of superconducting magnets and on superconducting multi-filament strands. The set-up of the different experiments are presented, results are discussed and first conclusions on the damage mechanisms and limits of the superconducting magnets are drawn.

À Elvira, Selma, Mathild et Mathys

Acknowledgements

I would like to thank professor Michael Benedikt for giving me the opportunity of being enrolled as a PhD student at TU Wien.

I wish to express my most sincere gratitude to my supervisor at CERN, Daniel Wollmann. During these three years I always felt followed, being at the same time free to work and take initiative. Thanks for the many fruitful discussions, for all your advices and critical comments, for the support to carry out the experiments and for your friendship.

In addition, I would like to thank all my colleagues for TE-MPE-PE and especially to Rüdiger Schmidt, Arjan Verweij, Bernhard Auchmann and Matthias Mentink for all the valuable discussions and for their availability to share their knowledge. A big thank you to Rüdiger Schmidt who has kindly read all these pages and commented upon them. The study on damage limits of superconducting magnets is still on-going and I wish the best to Andreas Will. I am looking forward to see the outcomes of the experiment at liquid helium temperature.

I am grateful to Carmine Senatore and Marco Bonura from University of Geneva for the magnetization measurements and for all the discussions on their interpretation.

A special mention to the two technical students that have been working with me on this project (David Kleiven and Karolina Kulesz). Thanks for your contribution!

All the experimental work done in this thesis would not have been possible without the help and support of many people. Therefore i would like to thank Christian Scheuerlein for all valuable discussions about this work, Angelo Bonasia and Sebastien Luzieux for providing the experimental samples, Roberto Lopez and Gianfranco Ravida for the use of their high voltage test stations, Adrian Fabich, Aymeric Bouvard and Vincent Clerc from HiRadMat team, Gijs de Rijk and Nicolas Bourcey for the use of their furnace,

Mickael Meyer and Stefano Sgobba for the microscopic observations, Mickael Guinchard, Oscar Sacristan de Frutos, Mateusz Bednarek, Reiner Denz, Mathieu Favre, Fabienne Boisier, Joaquim Mourao, Felix Rodriguez-Mateos, Julien Finelle and Damien Grenier for their advices and technical support to design and perform the experiments presented in this thesis.

I also would like to thank all the persons that I have shared an office with during these three years: Andrea Apollonio, Florian Burkart, Vera Chetvertkova, Tobias and Tina Griesemer, Yuancun Nie and Matthieu Valette.

Finally, I would like to thank my family.

Merci à Elvira, ma compagne avec qui je voyage depuis plus de 10 ans. Merci d'avoir toujours été à mes cotés. Merci d'avoir été particulièrement compréhensive et tolérante pendant cette période intense. Hvala puno my Elvi.

Merci à mes deux petites dragonnes d'avoir supporter un papa parfois ronchon.

Merci à mes parents. Sans leur soutien et confiance, je ne serais pas arrivé jusque là.

Contents

1	Introduction	1
2	Introduction to CERN accelerator chain	5
2.1	From Injectors to the Large Hadron Collider	5
2.2	LHC Injectors Upgrades and LHC Upgrades	9
2.3	Future Hadron Accelerators	9
3	Failure cases and Machine Protection in LHC and HL-LHC	11
3.1	Machine Protection for LHC and HL-LHC	11
3.1.1	Magnet quench and protection	12
3.1.2	Beam losses and protection	12
3.2	Ultra-fast failure cases for LHC and HL-LHC	14
3.2.1	Injection failures	14
3.2.2	Extraction failures	16
4	Beam-matter interaction	17
4.1	Particle-matter interaction	17
4.1.1	Hadronic interactions and showers	17
4.1.2	Electromagnetic interactions and showers	19
4.1.3	Stopping power and Energy deposition	20
4.1.4	Simulation tool - FLUKA	23
4.2	Thermo-mechanical effects	24
4.2.1	Temperature rise	25
4.2.2	Thermal stresses	26
5	Damage of Superconducting Magnets and their Components	29
5.1	General overview of superconductivity	29
5.1.1	Superconducting properties	29

CONTENTS

5.1.2	Nb-Ti and Nb ₃ Sn superconductor	34
5.2	Superconducting magnets	42
5.2.1	LHC Nb-Ti magnets	42
5.2.2	HL-LHC Nb ₃ Sn magnets	49
5.3	Damage mechanisms	50
5.3.1	Critical superconducting magnet components	50
5.3.2	Insulation degradation induced by temperature	52
5.3.3	Critical current reduction induced by temperature	54
5.3.4	Critical current reduction due to thermo-mechanical strain	55
6	Experimental Road Map	59
6.1	Experimental samples	59
6.1.1	Insulated Rutherford cable stacks	59
6.1.2	Superconducting Nb-Ti and Nb ₃ Sn strands	63
6.2	Measurements of insulation degradation due to heating during several hours	63
6.3	Measurements of superconductor degradation due to heating over seconds	66
6.3.1	Capacitive discharge set-up	66
6.3.2	Magnetization measurements	73
6.3.3	Microscopic measurements	73
6.4	Measurements of insulation and superconductor degradation due to beam impact	75
6.4.1	HiRadMat - Facility	75
6.4.2	Description of experiment	76
6.4.3	Temperature rise and cooling profile	81
6.4.4	Analysis of irradiated samples	89
7	Insulation degradation results and analysis	91
7.1	Dielectric strength measurements and visual inspection after heating	91
7.2	Mass loss	95
8	Critical current density degradation results and analysis	99
8.1	Nb-Ti results and discussion	99
8.1.1	Magnetization measurement results	99
8.1.2	Microscopic analysis results	105
8.1.3	Discussion	114
8.2	Nb ₃ Sn results and discussion	114
8.2.1	Magnetization measurement results	114

8.2.2	Microscopic analysis results	122
8.2.3	Discussion	128
9	Conclusion	131
A	Appendix: Technical drawings of the stainless steel moulds	133
B	Appendix: List of the superconducting strands used in the beam experiment	139
C	Appendix: Energy deposition simulation for the beam experiment	141
D	Appendix: Relation between relative resistance variation of a strand and its energy deposition profile	147
E	Appendix: Glossary	149
	References	151

CONTENTS

1

Introduction

High energy particle accelerators, like CERN's Large Hadron Collider (LHC), are major tools to perform experiments to improve our understanding of the universe. The goal of such machines is to deliver collision of high momentum particles at a high rate, measured as luminosity, allowing particle physicists to study particle physics.

The energy stored in the LHC beam can reach 362 MJ, sufficient to melt ~ 500 kg copper. An uncontrolled loss of a very small fraction (below 10^{-4} [1]) of the beam could already cause major damage to equipment and lead to significant downtime. Therefore a complex machine protection system is required to safely operate the accelerator. In addition studies of failure cases and of the damage limits of accelerator equipments are required to understand the risk for damage. This also provides essential information for the design of protection systems for future accelerators, such as the luminosity upgrade of the LHC (HL-LHC) or the Future Circular Collider (FCC). For example, studies on the so-called hydrodynamic tunnelling effect have shown that the full LHC proton beam would penetrate up to 35 m in solid copper and this would extend to ~ 350 m for the FCC beam [2].

In the LHC, beam losses can happen at very different time scales. The most critical beam losses are so-called ultra fast losses, faster than $360 \mu\text{s}$ (~ 4 LHC turns) and happen usually several times per year. Typically ultra fast losses are due to injection and extraction failures. Protection against such losses relies on passive protection elements such as collimators and absorbers. The interaction between the LHC beam and these passive devices generates particle showers which are intercepted by downstream elements such as superconducting magnets. The energy deposited in a superconducting magnet coil during such an event induces a temperature rise and mechanical stresses

1. INTRODUCTION

which can lead to a magnet quench or in the worst case to an irreversible damage of the magnet.

Damage mechanisms of superconducting magnets due to instantaneous energy deposition have never been studied in detail, including experiments. Nevertheless, it is possible to determine an energy deposition range below which damage of superconducting magnet components are excluded, and above which damage is certain. The melting of copper of the superconducting cables defines the upper boundary of this range. Once the copper starts to melt, the superconducting cables are assumed to be fatally damaged. Copper with an initial temperature of 2 K melts at an energy deposition of $\sim 6 \text{ kJ cm}^{-3}$. Experience from failures in the LHC as well as in other accelerators using superconducting magnets such as Tevatron, HERA and RHIC provide a lower boundary. From the worst ultra fast failures than happened in the LHC, an peak energy deposition of $\sim 6 \text{ J cm}^{-3}$ in the superconducting coils have been derived [3]. During this event, the magnets quenched but were not damaged.

HL-LHC requires an increase of the beam brightness (smaller emittance and higher intensity), this yields a factor two higher stored energy. As a consequence beam losses and in particular the ultra-fast ones become more critical. For instance studies of HL-LHC injection and extraction losses have shown that the energy deposition can reach 100 J cm^{-3} in superconducting magnet coils [4, 5]. Before this thesis, damage of superconducting magnets with these type of events could not be excluded. An improved understanding of the damage mechanisms and limits of superconducting magnets is therefore essential for the HL-LHC, as well as for other future accelerators using superconducting magnets.

In this thesis, for the first time the damage mechanisms and limits of superconducting magnet components are studied experimentally at room temperature. The magnet polyimide insulation and the Nb-Ti and Nb₃Sn superconducting multi-filament strands were identified as most critical components. An experimental program was defined to study the damage mechanisms and damage limits of these components. The experiments aimed to study the effect of heating over different time scales from hours down to tens of milliseconds on the dielectric strength of the insulation and the critical current density of the superconducting strands.

The experimental results are then analysed, interpreted and compared to known mechanisms.

Chapitre 2 of this thesis gives an overview of the CERN accelerator complex and present briefly its upgrade projects and the design of future colliders.

In chapter 3, the machine protection system of the LHC is presented and the known most critical beam losses in LHC and HL-LHC leading to significant energy deposition in superconducting magnets are discussed.

Chapter 4 describes the relevant processes during the interaction of beam with matter and the resulting effects in the matter.

In chapter 5, the basic concepts of superconductivity and the properties of Nb-Ti and Nb₃Sn superconductors are introduced. The design of the main LHC and HL-LHC superconducting magnets is presented. The most critical magnet components for damage due to instantaneous beam impact are identified and their damage mechanisms are discussed.

The experimental program and set-ups to study the damage mechanisms are presented in chapter. 6. The experimental results are discussed in chapter. 7 and in chapter. 8.

In chapter 9, the main results of the experimental study are interpreted and conclusions are drawn.

1. INTRODUCTION

2

Introduction to CERN accelerator chain

2.1 From Injectors to the Large Hadron Collider

The Large Hadron Collider (LHC) is the world's largest and most complex particle accelerator ever built. It has a circumference of 26.7 km and it is hosted in a tunnel, about 100 m deep in the underground of the swiss-french border region near Geneva [6]. The accelerator was designed to produce collisions between two proton beams with a particle momentum of $7 \text{ TeV } c^{-1}$. A magnetic field of 8.33 T is necessary to deflect protons with such high momentum, which requires the use of superconducting magnets. The LHC is also able to store and collide heavy ions such as lead (Pb^{82+}). The construction of the LHC was motivated by open questions in fundamental physics such as the predicted but not yet found particles of the so-called standard model of particle physics and other theories like super-symmetry, extra dimensions or the nature of the dark matter. On July 4th 2012, the discovery of the Higgs Boson was announced by the collaborations of LHC's two large experiments, ATLAS [7] and CMS [8], after less than three years of LHC operation.

A chain of smaller particle accelerators is used as pre-injectors to deliver the beam to the LHC. An overview of the CERN accelerator complex is given in Fig. 2.1. The proton source is located at the start of the second CERN linear accelerator (LINAC 2) in which the protons are accelerated up to a kinetic energy of 50 MeV. The particles are then injected in the four rings of the proton synchrotron booster (BOOSTER). The proton beams are bunched and accelerated up to an energy of 1.4 GeV before being recombined and extracted toward the Proton Synchrotron (PS). In the PS, the proton bunches are split and accelerated to 26 GeV before being injected in the Super Proton

2. INTRODUCTION TO CERN ACCELERATOR CHAIN

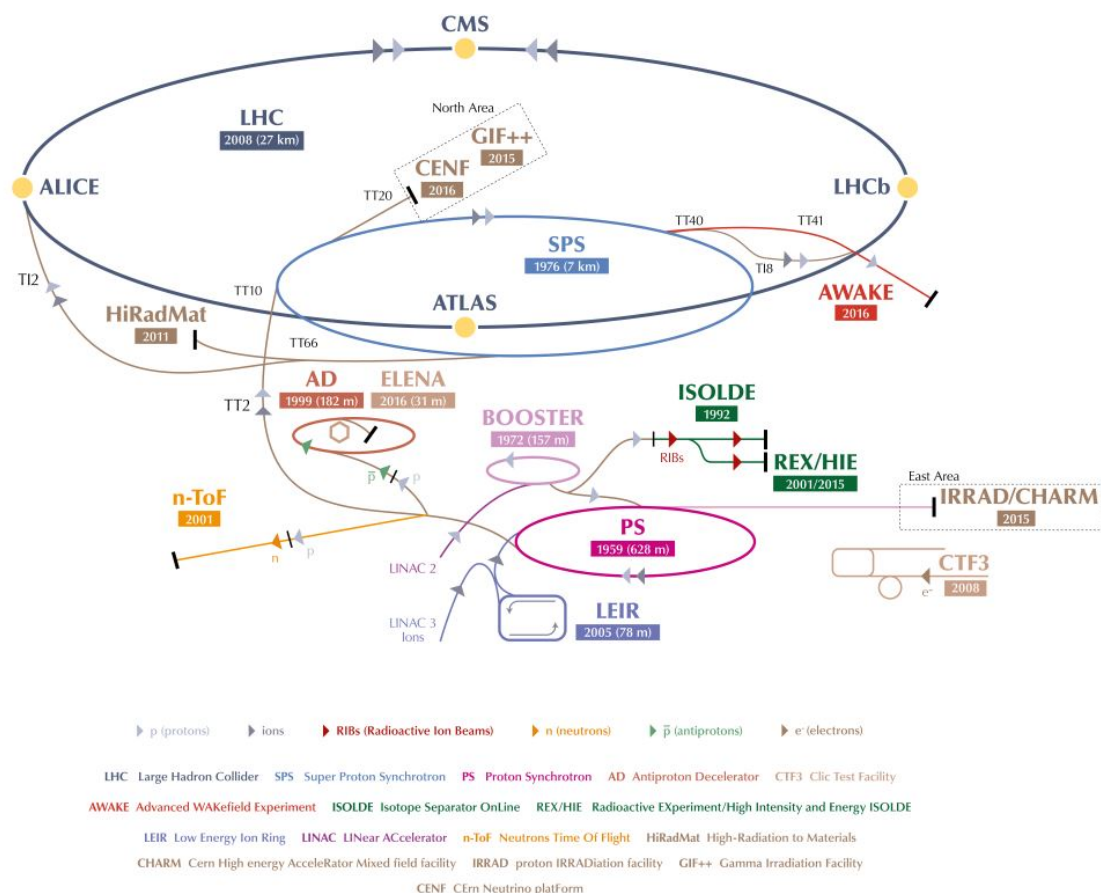


Figure 2.1: CERN accelerator complex. The LHC is the last ring (dark blue line) in a complex chain of particle accelerators. From the source, the protons travel through LINAC 2, Booster, PS, SPS before being injecting in the LHC. Heavy nuclei are delivered via LINAC 3, LEIR, PS and SPS.

Synchrotron (SPS) to further accelerate them to 450 GeV and inject them in the LHC through two transfer lines. The heavy nuclei travel starts in LINAC 3 and continue in the the Low Energy Ion Ring (LEIR), PS, SPS before being injected in the LHC.

The basic layout of the LHC, shown in Fig. 2.2, is formed by eight arcs and eight straight sections, the so-called Interaction Regions (IRs). The two counter-rotating beams circulate in separate vacuum chambers crossing each other at four points. The beams collide in the centre of the main experimental detectors of ATLAS (IR1), ALICE (IR2), CMS (IR5) and LHC-b (IR8). The beams are injected in IR2 (Beam 1) and IR8 (Beam 2) respectively and accelerated by superconducting 400 MHz radio frequency cavities positioned in IR4. After the acceleration, the beams are squeezed to reduce

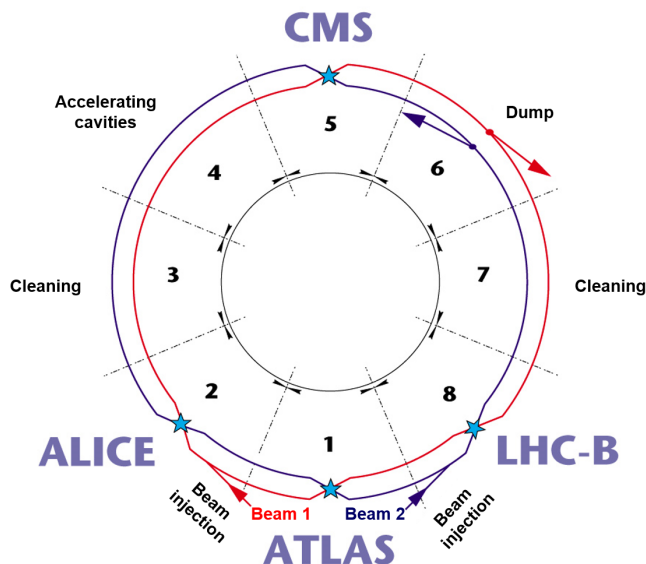


Figure 2.2: Schematic layout of LHC accelerator. The LHC is segmented in eight octants. The four major experiments are located in IR1, IR2, IR5 and IR8. The beams are injected in IR2 and IR8. The accelerating cavities are installed in IR4, the beam cleaning system in IR3 and IR7 and the beam dumping system in IR6. Beam 1 is circulating clockwise and Beam 2 counter clockwise.

their transverse sizes and then they are brought into collision. Typically the beams collide for several hours during a so-called physics fill. At the end of a fill or after the detection of a failure, the beams are extracted by the beam dumping system located in IR6 into specially designed absorber blocks. The two last IRs, IR3 and IR7, contain the beam collimation system responsible for beam cleaning and passive aperture protection.

In total about 8000 superconducting magnets, operated at temperatures of 1.9 K and 4.5 K, are present in the LHC to bend and focus the high momentum beams, among which are 1232 main dipoles (MB) and 386 main quadrupoles (MQ). The LHC superconducting magnets are built from Nb-Ti cables.

An overview of the nominal parameters of the LHC is presented in Table 2.1. The performance of the LHC can be quantified by the particle momentum at collision and by the number of collisions per unit time and area, called instantaneous luminosity L . The instantaneous luminosity can be expressed as:

$$L = \frac{n_b N^2 f_{rev}}{4\pi\beta^* \varepsilon_n} R \quad (2.1)$$

2. INTRODUCTION TO CERN ACCELERATOR CHAIN

Table 2.1: Main beam parameters of the LHC for 2012 [9], 2017 [10], nominal [6] and HL-LHC nominal [11]. The yearly integrated luminosity of 2012 and 2017 are from [12] and [13] respectively. The total integrated luminosity on the life-time of LHC (until ~ 2023) and HL-LHC (until ~ 2035) are from [11]. The integrated luminosity is expressed in femtobarn $^{-1}$ (10^{15} barn) which is equivalent to 10^{39} cm $^{-2}$.

	2012	2017	LHC nominal	HL-LHC nominal
Momentum at collision (TeV c^{-1})	4	6.5	7	7
Dipole field for peak momentum (T)	4.16	7.7	8.3	8.3
Protons per bunch ($\times 10^{11}$)	1.6	1.25	1.15	2.2
Transverse normalized emittance (μm)	2.5	1.8-2.1	3.75	2.5
Number of bunches per beam	1380	2556	2808	2748
Bunch spacing (ns)	50	25	25	25
Instantaneous luminosity (10^{34} cm $^{-2}$ s $^{-1}$)	0.7	2.2/1.5 ¹	1.0	19.54/5 ¹
Yearly integrated luminosity (fb $^{-1}$)	23.27	~ 50	-	250
Total integrated luminosity (fb $^{-1}$)	-	-	300	3000

¹ levelled luminosity

where n_b is the number of bunches per beam, N the number of particles per bunch, f_{rev} is the revolution frequency, β^* is the beta function at the collision point, ε_n is the transverse normalized emittance of the beam. R is the geometric reduction factor and can be developed as:

$$R = 1/\sqrt{1 + \frac{\theta_c \sigma_z}{2\sigma}} \quad (2.2)$$

where θ_c is the full crossing angle between the colliding beam and σ_z and σ are the beam longitudinal and transverse root mean square (r.m.s.) size. Therefore to increase the instantaneous luminosity of the LHC, the only parameters that can be optimized are N , ε_n , β^* and R . Increasing N and ε_n requires an upgrade of the LHC injector to deliver a beam with a higher brightness. Increasing β^* requires an upgrade of the quadrupole magnets at the interaction region. Increasing R by reducing θ_c would imply the implementation of crab-cavities to make the beams collide head-on. Such upgrades of the LHC and its injectors are discussed in the next section.

Luminosity levelling which already used in the LHC and will be part of the baseline for HL-LHC (see Table 2.1), consists in keeping the the instantaneous luminosity constant at the beginning of the physics fill to limit event pile-up for the particle detectors i.e. the maximum number of simultaneous interesting events that can be recorded by

the detectors.

2.2 LHC Injectors Upgrades and LHC Upgrades

To extend the discovery potential of the LHC, a major upgrade project of the LHC called High-Luminosity LHC (HL-LHC) is on-going and will be fully implemented by 2026 [11]. In order to provide the LHC with beams fulfilling the HL-LHC requirements (see Table 2.1), the LHC injector complex needs to be upgraded. Therefore the LHC Injector Upgrade project (LIU) is on going and the major upgrades will be implemented during the so-called second long shut down of the LHC (2019-2020) [14]. The existing LINAC 2 will be replaced by LINAC 4, an H^- linear accelerator with an output energy of 160 MeV. A charge exchange injection scheme will be implemented in the four rings of the Booster allowing the production of beams with twice higher brightness than presently. The extraction energy of the Booster will be increased to 2 GeV to allow higher beam brightness in the PS. The SPS radio frequency system will be upgraded to increase the allowed total beam intensity accelerated in the SPS.

The targets of HL-LHC is to increase the peak luminosity of LHC by a factor five to seven and to reach a yearly integrated luminosity of 250 fb^{-1} and a total integrated luminosity of 3000 fb^{-1} on the life-time of HL-LHC. Reaching these goals requires significant hardware upgrades for both experiment and accelerator equipments. For instance about 1.2 km of LHC magnets will be replaced. Among the new magnets, two magnet types will use superconducting cables made of Nb_3Sn filaments: the low- β single aperture triplet quadrupoles (Q1, Q2a, Q2b and Q3) called inner triplets and the so-called 11 T twin-apertures dipoles. In order to achieve smaller beam sizes at the IPs and, thus, increasing the luminosity, the inner triplets will have to feature of field gradient of 132.6 T m^{-1} with an aperture of 150 mm as compared to 200 T m^{-1} with an aperture 70 mm in today's LHC. An assembly of two 11 T dipoles with a warm collimator in between will replace one of the LHC dipole magnets in the dispersion suppressors left and right of IP7 to reduce losses into the cold apertures from the collimator region (see Fig 2.3).

2.3 Future Hadron Accelerators

Following a proposal of the European Strategy for Particle Physics in 2013, CERN together with partners across Europe is undertaking design studies of post-LHC accelerators. Among several studies, the High Energy LHC (HE-LHC) [16][17] and the Future Circular Collider (FCC) [18], both hadron colliders have launched an ambitious R&D

2. INTRODUCTION TO CERN ACCELERATOR CHAIN

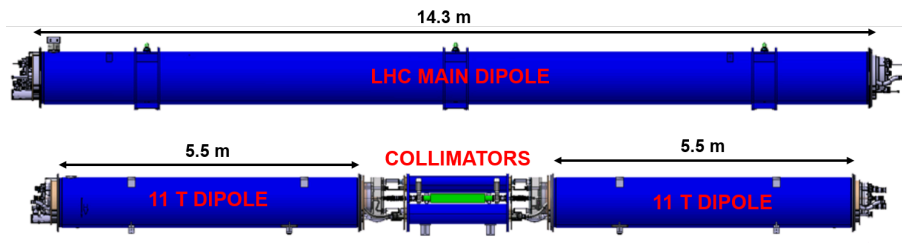


Figure 2.3: Schematic view of the assembly of two shorter 11 T dipoles with a collimator in between, which can replace one standard main dipole [15].

Table 2.2: Main parameters of HE-LHC and FCC

	HE-LHC [19]	FCC [20]
Momentum at collision ($\text{TeV } c^{-1}$)	13.5	50
Dipole field for peak momentum (T)	16	16
Circumference (km)	26.7	97.7
Peak Luminosity ($10^{34} \text{ cm}^{-2}\text{s}^{-1}$)	25	30

program to develop 16 T magnets based on Nb_3Sn superconductors. The HE-LHC project proposes to increase the nominal energy of the LHC to 13.5 TeV per beam by substituting all the present dipoles with new, more powerful ones, capable of operating at 16 T. The FCC study proposes the construction of a 50 TeV per beam collider in a tunnel with a circumference of about 100 km. The main parameters of both projects are given in Table 2.2.

3

Failure cases and Machine Protection in LHC and HL-LHC

The nominal stored energy in each of the two LHC proton beams is 362 MJ. With the HL-LHC upgrade, this will be closed to double to ~ 700 MJ. To protect the accelerator equipments from damage, a complex Machine Protection System (MPS) is required. The protection against the most critical failures causing beam losses, the so-called ultra-fast failures, which are faster than $360 \mu\text{s}$, relies on passive absorbers [1]. The interaction between a high-energy proton beam and these absorber blocks generates particle showers, which impact on downstream accelerator elements such as superconducting magnets. In such cases, the impacted superconducting magnets can quench. However, it is unknown, if with the HL-LHC beam brightness, superconducting magnets can be damaged after such events. In this chapter, the MPS of the LHC and HL-LHC is presented and two examples of the most critical failures in the LHC with HL-LHC beam parameters and the resulting energy deposited in the superconducting magnets are discussed.

3.1 Machine Protection for LHC and HL-LHC

In addition to the stored beam energy, the main dipole circuits have a stored energy of 1.2 GJ ($154 \text{ magnet} \times 7.6 \text{ MJ}$) at a nominal current of 12 kA. The primary goals of the MPS is to make sure that in case of equipment failures or beam instabilities leading to beam losses, these stored energies are deposited in a safe way.

3. FAILURE CASES AND MACHINE PROTECTION IN LHC AND HL-LHC

3.1.1 Magnet quench and protection

Quench (loss of superconductivity) of superconducting magnets can be initiated by several mechanisms. An energy deposition in the order of several tens of mJ cm^{-3} [21], for example due to beam losses, can initiate a quench. Some other mechanisms for inducing a quench are flux jumps, movements of the superconductor by several micrometer (friction and heat dissipation) or a failure of the cooling system. Without protection, the temperature in the resistive zone of a LHC dipole magnet after a quench would increase within less than 1 s to 1000 K and the magnet would be destroyed [1].

In the LHC as soon as a quench is detected by the Quench Protection System (QPS) [22] via monitoring the voltage across superconducting coils, the magnet circuit is switched off by triggering a fast power abort of the power converters. To dissipate the stored energy over a large volume and therefore to reduce the peak temperature, a large part of the quenched magnet coils is forced to quench either by firing quench heaters [23] or the Coupling Loss Induced Quench (CLIQ) system [24]. As the dipole magnets are powered in series, the energy stored in the non-quenching magnets is dumped in a resistor which is switched in series with the magnet string [25]. During the discharge, current in the quenched magnet is by-passed via a cold diode.

3.1.2 Beam losses and protection

Beam losses due to equipment failures can be classified as function of their time scale: ultra-fast losses occurring in less than four LHC revolution turns ($\sim 360 \mu\text{s}$, one revolution takes $89 \mu\text{s}$), fast losses between $360 \mu\text{s}$ and one second and steady state losses in more than one second.

Steady state losses

Steady state losses are unavoidable losses around the LHC ring and mostly intercepted by the collimation system [26].

Fast losses

Fast beam losses can have different origins: magnet power converter failures, quenches in superconducting magnets, failure of the normal conducting separation dipole (D1 [27]) in IP1 and IP5 [28], Unidentified Falling Object (UFOs) [29, 30]. UFOs are charged dust particles that can interact with the beam, generating particle losses that can induced a magnet quench [31].

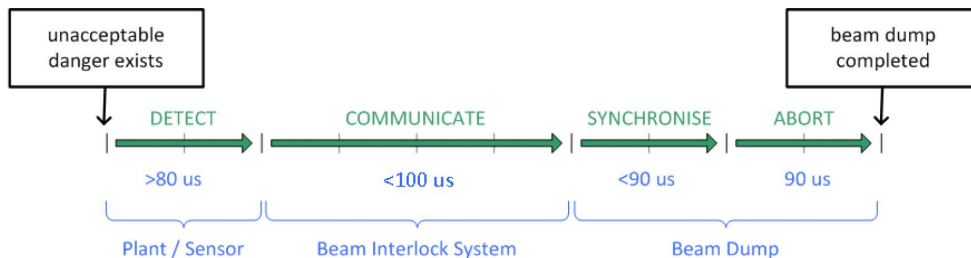


Figure 3.1: Current MPS response time from failure detection to completion of beam dump [15].

The protection from such losses is based on the early detection of failures within the equipments, as well as monitoring of the beam parameters with fast and reliable beam instrumentation. Once a failure is detected, the information is transmitted to the Beam Interlock System (BIS) [32] that triggers the extraction of the particles beams by the LHC beam dumping system (LBDS) [33].

The beam dumping system located in IR6 extracts safely the beam from the ring to transport it to the dump block. In order to extract the beam, 15 extraction kicker magnets located in the LHC ring kick the beam horizontally into the high-field gap of 15 septum magnets which deflect the beam vertically into the transfer line toward the dump block. In order to reduce the energy density in the dump block, the beam is distributed over a surface of $\sim 35 \times 35 \text{ cm}^2$ by several dilution kicker magnets during the transfer from the LHC ring to the dump block. The current rise time of the extraction kickers is $3 \mu\text{s}$, therefore a particle-free gap (called abort-gap) of the same duration must be left in the beam to avoid signification losses while extraction the beams.

Equipment failures or beam instabilities can be identified via different systems: QPS to detect magnet quench, Fast Magnet Current change Monitors (FMCM) to detect failure in normal conducting magnets [34], Beam Position Monitors (BPM) to detect fast movement of the beam orbit [35] and the Beam Loss Monitoring system (BLM) to monitor the particle losses all around the LHC [36, 37].

The BLM features the shortest failure detection time of $40 \mu\text{s}$. Adding the time required to transmit the detected failure through the BIS, the time required to synchronize the current rise of the extraction kickers with the abort-gap and the time needed to completely extract the beam from the LHC lead to a minimum response time of the MPS of $360 \mu\text{s}$ as shown in Fig. 3.1.

3. FAILURE CASES AND MACHINE PROTECTION IN LHC AND HL-LHC

Ultra-fast losses

Ultra-fast losses are due to failures at beam injection and extraction. Their time scale is smaller than the minimum response time of the MPS. The protection from such losses relies therefore on beam absorbers and collimators that need to be correctly positioned to capture the particles that are deflected accidentally. In the next section, examples of such failures and their consequences on the superconducting magnets are given for LHC and HL-LHC.

3.2 Ultra-fast failure cases for LHC and HL-LHC

Injection and extraction failures happen usually several times per year in the LHC, often inducing quenches in superconducting magnets. Particle-matter interaction simulations using the FLUKA code (see section 4.1.4) were performed to quantify the energy deposited in the superconducting magnet coils during such a failure with LHC and HL-LHC beam parameters. With the knowledge at that time (in 2014) on the damage limits of superconducting magnets, it was not possible to conclude if the superconducting magnets were sufficiently protected in case of ultra-fast failure with HL-LHC beam parameter. Thus it was decided to launch this study on the damage mechanisms and limits on superconducting magnets due to beam impact.

3.2.1 Injection failures

The beams are injected in LHC from the SPS with a momentum of $450 \text{ GeV } c^{-1}$ in the straight sections IR2 for Beam 1 and IR3 for Beam 2 (see Fig. 2.2). In order to fill the LHC ring with 2808 bunches, several injections per beam are necessary. At each injection, a train of 144 or 288 bunches is injected in the LHC.

The bunches coming from the transfer line from the SPS into the LHC are first deflected horizontally by five septum magnets (Magnet Septum Injection - MSI) and then vertically onto the LHC closed orbit by a series of four fast-pulsed magnet kickers (Magnet Kicker Injection - MKI). Misinjections (wrong deflection angle or no deflection of the injected beam) or accidental firing of one of the MKI (deflecting the LHC circulating beam) are protected by a system of beam intercepting devices such as the injection beam stopper (TDI). An additional absorber made of steel (TCDD) with similar aperture as the superconducting separation dipole magnet, D1, is installed downstream of the TDI. An schematic layout of injection protection devices and magnets in the region right of IP8 is shown in Fig. 3.2.

3.2 Ultra-fast failure cases for LHC and HL-LHC

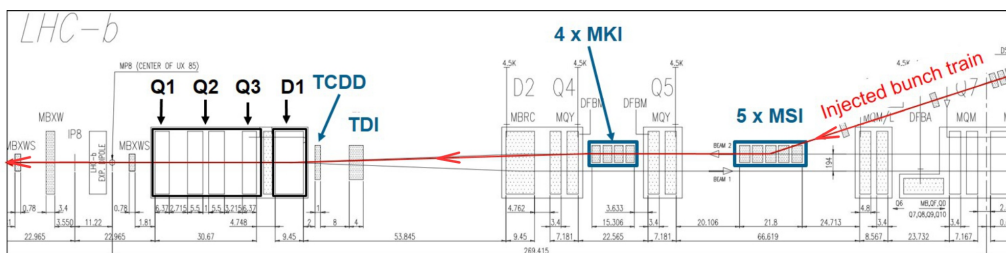


Figure 3.2: Schematic layout of the injection region of Beam 2, right of IP8 with the injection protection devices (TDI and TCDD) and the injection magnets (MSI and MKI). The superconducting separation dipole magnet D1 and the triplet quadrupole magnets (Q1, Q2, Q3) are highlighted in black [38].

The particle showers generated by the interaction between high energy protons and the TDI can impact the downstream superconducting magnets D1 and the triplet quadrupole magnets (Q1, Q2, Q3). Several of these events during the first three years of LHC operation have been reported [3]. For MKI failures leading to a missing deflection of the injected train, the full energy of the injected bunches was absorbed by the TDI. However for other cases such as deflection of the injected bunch train with a non-nominal angle and deflection of circulating bunches, the superconducting magnets downstream of the TDI quenched. The worst case observed up to now was an erratic firing of the MKI in IR2 causing the deflection of circulating bunches. As a consequence, ~ 176 bunches with a total intensity of $\sim 2.15 \times 10^{13}$ protons were lost in the accelerator, inducing quenches in D1 and in the triplet quadrupoles. The peak energy density deposited in superconducting D1 and Q3 magnet coils was estimated to about 6 J cm^{-3} . No damage was observed in the main magnets however three circuits of corrector magnets placed upstream of Q3 were found open after the event. It is believed to be a consequence of the neighbouring magnet quench rather than to the energy deposited by the particle shower.

The injection system including MKIs and TDI have to be modified to inject beam with the HL-LHC beam parameters [39]. Studies of injection failures during HL-LHC era were done to evaluate if D1 and the triplet quadrupole magnets needed more protection [4]. It was shown that the peak energy density in the superconducting D1 magnet could reach about 100 J cm^{-3} , equivalent to a temperature rise to about 120 K within few μs . At that time, it was not possible to conclude on the risk of damage of the D1 magnet during such event.

3. FAILURE CASES AND MACHINE PROTECTION IN LHC AND HL-LHC

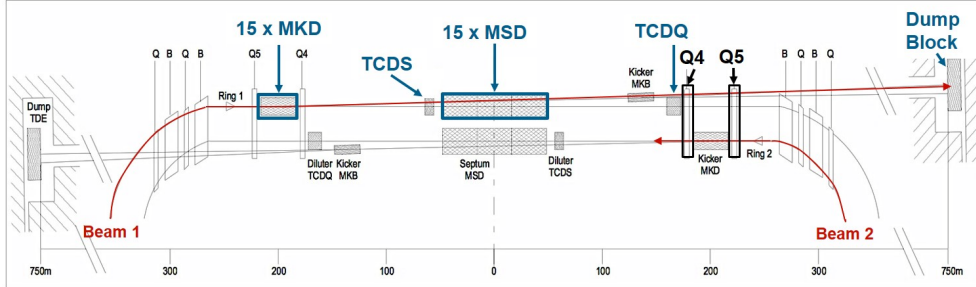


Figure 3.3: Schematic layout of the LHC beam dump system in IR6. Beam 1 (red arrow) is extraction from the LHC ring by 15 extraction kicker magnets (MKDs) and 15 septum magnets (MSD) toward the dump block. The extraction protection devices TCDS protect the MSDs and the TCDQ the quadrupole magnets Q4 and Q5 [33].

3.2.2 Extraction failures

In Fig 3.3, the layout of the LHC beam dump system in IR6 is shown. As explained in the previous section (see section 3.1), when the beams are extracted from the LHC ring toward the dump block, it is necessary that the rising of the extraction kickers (MKDs) is synchronized with the abort-gap. If the MKDs field rises when particles are present, particles are deflected with a wrong angles. This is called an asynchronous beam dump. The wrongly deflected particles should be absorbed by the TCDS to protect the septum magnets (MSD) and by the TCDQ to protect the Q4 and Q5 superconducting quadrupole magnets. Shower particles might escape from the TCDQ and interact with Q4 and Q5 inducing a quench. The LHC was designed to accept occasionally asynchronous beam dump. As for the injection, the beam dumping system will have to be reviewed for HL-LHC [40]. In case of an asynchronous beam dump with HL-LHC beam parameters, the peak energy densities deposited in Q4 and Q5 were estimated to $\sim 10 \text{ J cm}^{-3}$ and $\sim 30 \text{ J cm}^{-3}$ respectively [5].

4

Beam-matter interaction

As discussed in the previous chapter, in the LHC following an injection or extraction failure, a significant energy is deposited in superconducting magnet coils. In this chapter, the particle-matter interaction mechanisms relevant for high energetic incident protons and the consequences for the impacted materials (temperature rise and thermal stresses) are presented.

4.1 Particle-matter interaction

In the LHC when a proton with a high energy, i.e. from several hundreds of GeV up to several TeV, is deflected toward the aperture, it travels through matter with a certain probability to interact with the nuclei and the electrons of the medium. During these interactions, the proton can be scattered, can transfer parts of its energy to the medium and secondary particles can be produced. If the secondary particles have enough energy to trigger further interactions, it generates a particle shower. Depending on the particles mass, charge and energy, the dominant interaction mechanisms with the medium are different. The energy is deposited in the matter mostly via Coulomb interaction between the shower particles and the electrons and nuclei of the medium.

4.1.1 Hadronic interactions and showers

The incident high energetic protons can interact elastically and inelastically with the nuclei of the medium via the strong force. As long as protons have an energy above few tens of MeV, inelastic interaction play a major role. Secondary particles produced by such interaction have enough energy to trigger further interactions, giving rise to a hadronic shower. During such inelastic collision, the incident hadrons loose part

4. BEAM-MATTER INTERACTION

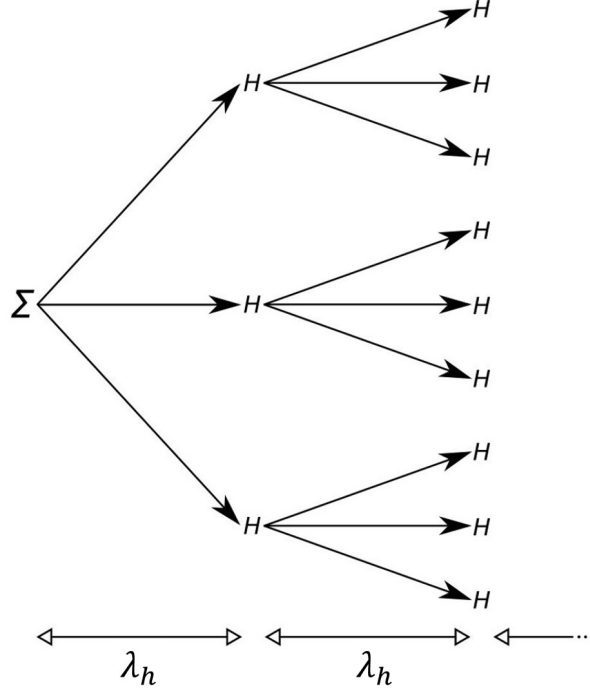


Figure 4.1: Development of an hadronic shower generated by a sigma baryon entering a block of lead, assuming that each hadron striking a lead atom produces three more hadrons. The absorption length λ_h defined as the mean distance travelled by a hadron in matter before it undergoes an inelastic collision [42].

of their energy and can be deflected. For hadrons with an energy above 290 MeV, inelastic interaction can lead to the production of π^0 pions. Such process is significant above 700 MeV [41]. The pions are decaying in two photons which can interact with the medium via various processes producing secondary particles (leptons and photons), generating an electromagnetic shower.

Fig 4.1 shows the development of a hadronic shower generated by a sigma baryon entering a block of lead, assuming that each hadron striking a lead atom produces three more hadrons. The mean distance travelled by a hadron in matter before it undergoes an inelastic collision is called the absorption length λ_h . Between each hadronic interaction the charged hadrons can interact with the atomic electrons via the Coulomb force, exciting atoms or causing ionization. Electron can be kicked out of their shell and the material get ionized. Through this process, the hadrons loose part of their energy. When hadrons have not sufficient energy to survive such losses along the absorption length they have to travel before they undergo the next hadronic interaction, the hadronic shower stops developing.

4.1.2 Electromagnetic interactions and showers

Electrons and photons produced by the interaction between the incident protons and matter can further interact with the target. During such interaction, energy is transferred to the medium and more secondary particles are produced initiating an electromagnetic shower.

Electrons and Positrons

The energy loss of high energy electrons and positrons is dominated by bremsstrahlung. Bremsstrahlung is the emission of a photon when a charged particle is deflected by an electric field (the Coulomb field of an atom). Low energy electrons and positrons interact with matter mostly via inelastic Coulomb scattering leading to ionization and excitation of the target atoms.

Photons

Photons can interact with matter through different processes: the photoelectric effect, Compton scattering and pair production. The photoelectric effect, which dominates at low energies leads to the emission of electrons from the medium after it is illuminated by light of a sufficient high frequency. The Compton scattering dominating at medium energies is the scattering of photons by atomic electrons. The scattered photons undergo a wavelength shift, which is independent of the initial wavelength and the medium. Pair production is the absorption of a photon resulting in a production of an electron and a positron and is dominating at high energies. The pair production cannot occur for photons having an energy below the energy of two electron masses, 1.02 MeV and must occur in the vicinity of an atomic nucleus. The total photon mass attenuation coefficients which is the combination of the coefficients of all three processes is shown in Fig. 4.2.

Electromagnetic showers

π^0 pions decay in two high energy photons that can further interact with the medium giving rise to an electromagnetic shower. A simple model of an electromagnetic shower is shown in Fig. 4.3. A photon generated by the π^0 pion decay, interacts with matter producing an electron-positron pair via pair production. After a radiation length X_0 , the newly produced electron and positron will then emit photons via bremsstrahlung. X_0 describes the distance along which a particle has lost $1/e$ of its initial energy by bremsstrahlung. This process will continue and grow exponentially until the energy

4. BEAM-MATTER INTERACTION

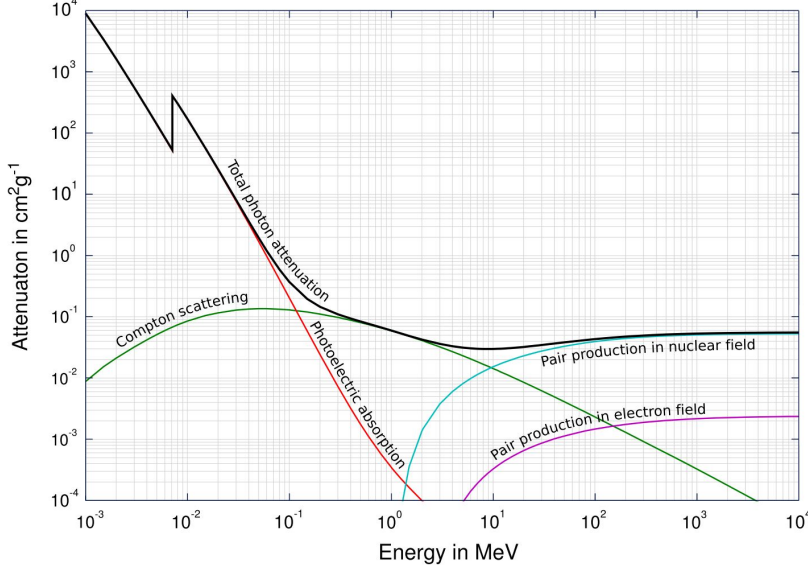


Figure 4.2: Photon mass attenuation coefficients and total attenuation in iron [42].

of electrons drop below the critical energy E_C when they dissipate their energy by ionization and excitation.

4.1.3 Stopping power and Energy deposition

The mean energy loss of a particle per unit length travelled $\langle \frac{dE}{dx} \rangle$ is called stopping power. It can be described depending of the type of particle.

Stopping power of heavy charged particles

For particles heavier than electron, the stopping power is described by the Bethe-Bloch equation [43]:

$$-\langle \frac{dE}{dx} \rangle = K \frac{Zz^2}{A\beta^2} \cdot \left[\frac{1}{2} \ln \left(\frac{2m_e c^2 \gamma^2 \beta^2 W_{max}}{I^2} \right) - \beta^2 - \frac{\delta(\beta\gamma)}{2} - \frac{C}{Z} \right], \quad (4.1)$$

$$K = \frac{N_A e^4}{4\pi \epsilon_0^2 m_e c^2}, \quad (4.2)$$

with the Avogadro constant N_A , the elementary charge e , the electron mass m_e , the vacuum permittivity ϵ_0 , the speed of light in vacuum c , the charge of the incident particle z , $\beta = \frac{v}{c}$ with v the speed of the incident particle, $\gamma = \frac{1}{\sqrt{1-\beta^2}}$, the atomic and nuclear number of the target Z and A , the mean ionization potential (material constant of the target) $I = 16Z^{0.9}$ [eV] if $Z > 1$, the maximum energy transfer in a single

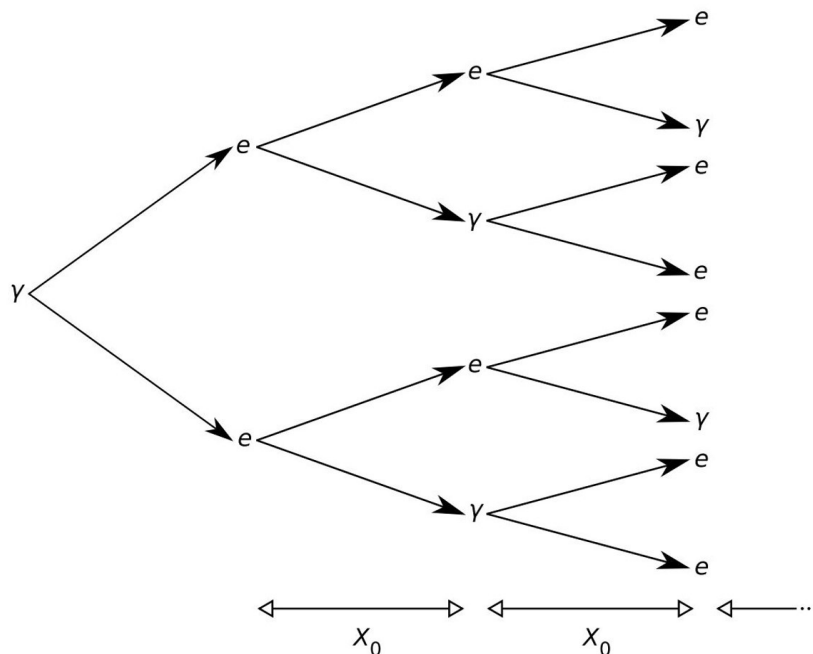


Figure 4.3: Development of an electromagnetic shower [42].

collision W_{max} , the density correction term for very high energy $\delta(\beta\gamma)$ and the shell correction for small particle velocities C . It is accurate within a few % for protons with a momentum between $\sim 100 \text{ MeV } c^{-1}$ and $1 \text{ TeV } c^{-1}$. The stopping power in several materials is shown in Fig. 4.4. The curves are characterized by a minimum between $\beta\gamma \equiv 3.0$ and 4 , called the minimum ionization loss [42]. For particles with a $\beta\gamma > 1000$, equivalent to a momentum $p = 1 \text{ TeV } c^{-1}$ in case of protons, radiative mechanisms (e.g. bremsstrahlung) become the dominating energy loss process. At low energy, the energy losses are described by the Anderson-Ziegler formula for $0.01 < \beta\gamma < 0.05$ and by the formula of Lindhard-Sharff below $\beta\gamma < 0.01$ [43]. As an illustration the stopping power of positive muons in copper as a function of their momentum is shown in Fig. 4.5. The different contributions of the energy loss are visible, with the total energy loss sum of all the contributions indicated as solid line.

Stopping power of electrons and positrons

The stopping power for electrons and positrons can be expressed as:

$$-\left\langle \frac{dE}{dx} \right\rangle = \frac{E}{X_0}, \quad [42] \quad (4.3)$$

4. BEAM-MATTER INTERACTION

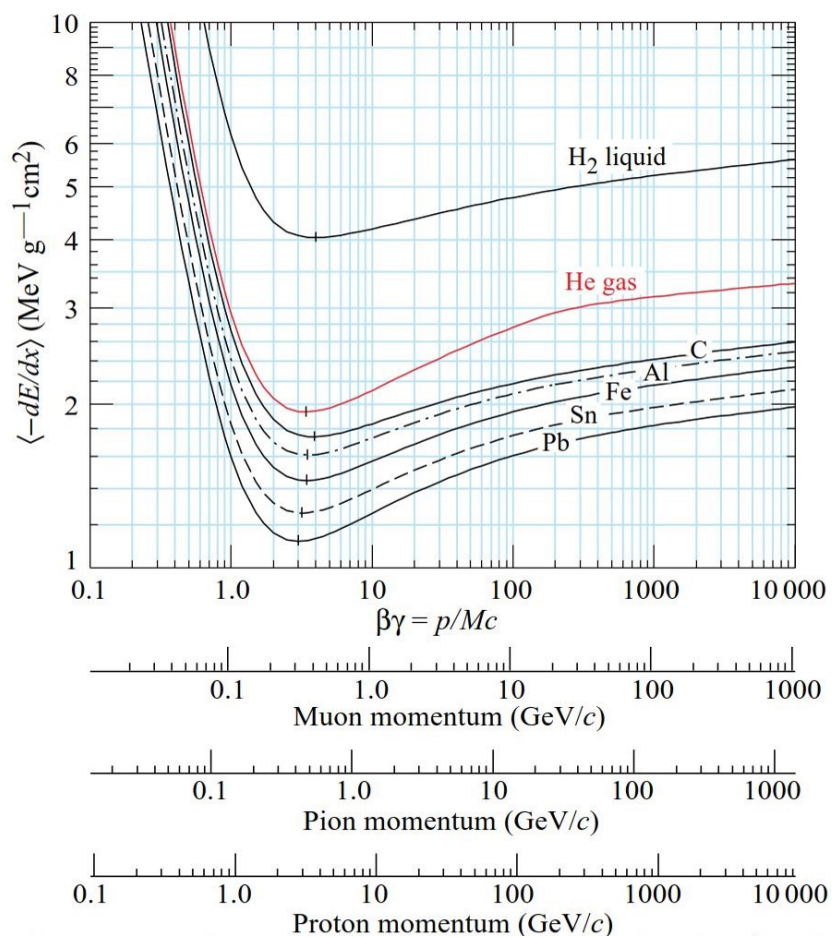


Figure 4.4: Mean energy loss rate in liquid hydrogen, gaseous helium, carbon, aluminium, iron, tin and lead for muons, pions and protons. Radiative effects, relevant above $\beta\gamma \geq 1000$ are not included [43].

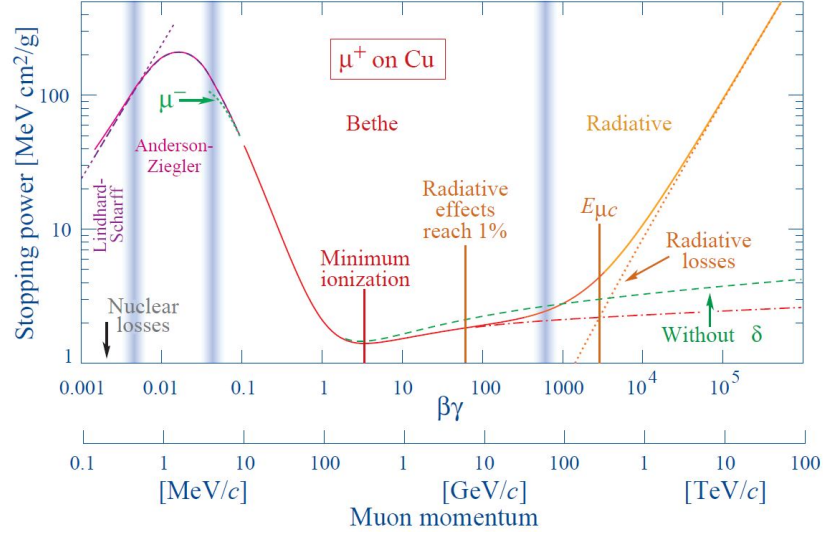


Figure 4.5: Stopping power for positive muons in copper as a function of $\beta\gamma = p/Mc$ with M the muon mass. The solid curve indicates the total stopping power sum of the different contributions [43].

with X_0 the radiation length and E the kinetic energy of the incident particle. An overview of the fractional energy loss per radiation length in lead as a function of the electron/positron energy is shown in Fig. 4.6. Below the critical energy of about 7 MeV, the ionization losses and above it bremsstrahlung's losses are dominating.

Energy deposition

The energy of the incident proton beam is mostly deposited in matter via inelastic Coulomb scattering between the shower particles and the electrons of the medium. The shower particles with the highest energy are concentrated around the beam axis. Their stopping power $\langle \frac{dE}{dx} \rangle$ and the electromagnetic shower associated with the π^0 pions dominate the energy profile around the beam axis. The radial tails of the energy deposition profile is defined by the neutrons stopping power. Neutrons interaction at moderate to low energy are dominating. The longitudinal shower development is ruled by shower particles, which carry a good fraction of the energy and have a longer interaction length.

4.1.4 Simulation tool - FLUKA

In this thesis, the FLUKA code [44, 45, 46] is used to calculate the energy deposited by a high-energy proton beam into several magnet components. FLUKA is a multi-purpose

4. BEAM-MATTER INTERACTION

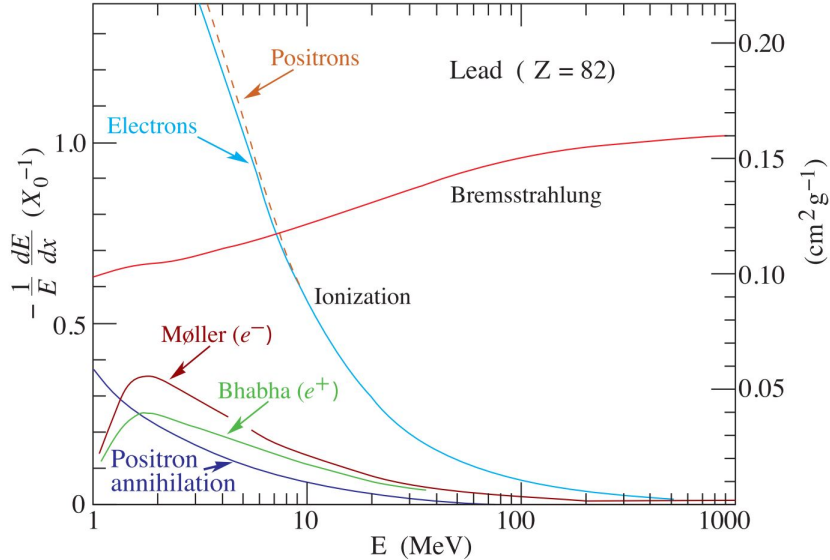


Figure 4.6: Fractional energy loss per radiation length in lead as a function of the electron/positron energy. The bremsstrahlung losses is dominating for energy above ~ 7 MeV. At low energies, other contributions are visible, Moller and Bhabha scattering and positron annihilation [43].

Monte Carlo simulation tool for calculations of particle transport and interactions with matter. Its applications cover an extended range from proton and electron accelerator shielding and target to detector design, to activation studies and dosimetry, to cosmic ray studies, to radiotherapy, etc. FLUKA is capable of simulating with high accuracy the interaction and secondary shower propagation in matter of about 60 different particles, including photons and electrons from 100 eV to thousands of TeV, neutrinos, muons of 1 keV to 1000 TeV, hadrons of energies from keV up to 20 TeV (up to 10 PeV by using the DPMJET code [47]) and all the corresponding anti-particles, neutrons down to thermal energies and heavy ions. The geometry of the target is described in combinatorial geometry. The detailed transport limits of secondary particles and primary particles, the models applied in FLUKA, and the bench-marking can be found in [44, 45, 46].

4.2 Thermo-mechanical effects

The energy deposited by a high energy beam in a target material induces a temperature increase and thermal stresses in the material that can lead to extensive damage of the

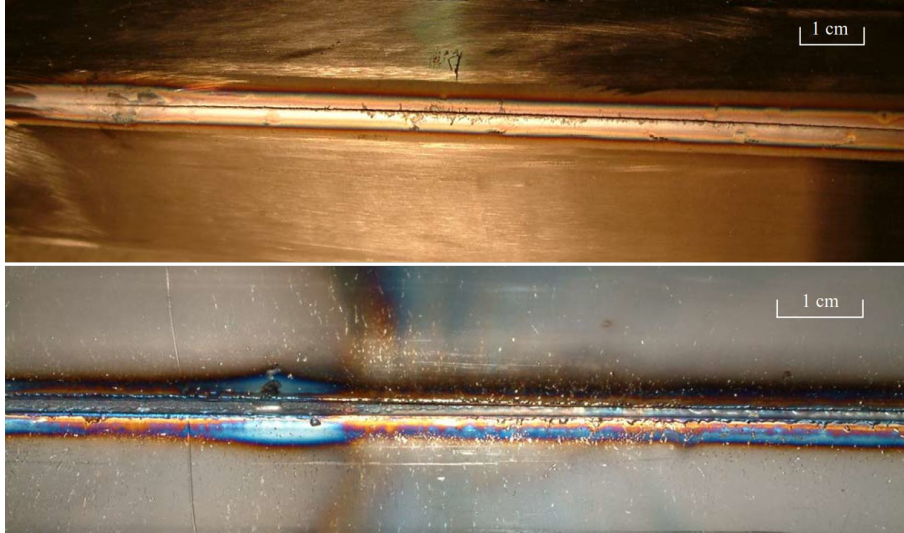


Figure 4.7: Damage observed on the outside (upper) and inside (lower) of the vacuum chamber after an uncontrolled loss of 3.4×10^{13} protons with a momentum of $450 \text{ GeV } c^{-1}$ in the transfer line from the SPS to the LHC. The chamber was damaged over approximately a length of 110 cm [48].

targeted material. The damage can be temperature induced like melting, vaporization and also stress induced such as deformations and cracks.

4.2.1 Temperature rise

The temperature rise inside the material is dependent on the beam parameters (transverse beam size, intensity and particle type) and on the properties of the target material (density and specific heat). As an illustration, Fig 4.7 shows a damaged vacuum chamber of a transfer line of the SPS after the loss of 3.4×10^{13} protons with a momentum of $450 \text{ GeV } c^{-1}$. Parts of the vacuum chamber were molten. A large vacuum leak was immediately observed after the incident and the coil insulation on the neighbouring normal conducting magnet was damaged. The magnet had to be exchanged for a spare, which led to a downtime of the SPS of about two days. Another example of high-energy particles inducing temperature rise in material is from the experiment performed to establish the existence of hydrodynamic tunnelling phenomenon [49], in which targets made of 10 cm long copper cylinders were impacted by $440 \text{ GeV } c^{-1}$ proton beam pulses. In Fig. 4.8, the front and back faces of one of the copper cylinders after the impact of 2.16×10^{13} protons with a momentum of $440 \text{ GeV } c^{-1}$ are shown. In the core of the cylinder, the copper reached vaporization temperature (2868 K).

4. BEAM-MATTER INTERACTION



Figure 4.8: Front face (left) and back face (right) of a copper cylinder after an impact of 2.16×10^{13} protons with a momentum of $440 \text{ GeV } c^{-1}$ [50].

4.2.2 Thermal stresses

The fast temperature rise due to the impact of high-energy particles can give rise to two types of thermal stresses: quasi-static stress caused by the thermal gradient in the impacted material and dynamic stresses due to mass inertia preventing the thermal expansion of the heated material.

In a freely suspended target which is slowly and uniformly heated, no thermal stresses will occur. A non-uniform heating of a target gives rise to quasi-static stresses. In a target heated by beam pulse, the maximum value of the quasi-static stress is reached at the end of the beam pulse. However if the beam pulse is longer than the thermal diffusion time in the material, typically some tens of milliseconds, the magnitude of the quasi-static stress will decrease with the decreasing temperature gradient. The maximum of the quasi-static stress also depends on the distribution of the heat when deposited by the beam. For smaller transverse beam sizes, the stress will be higher. For very fast heating times, τ_h , in the same order as the time required by sound to traverse the impacted material, $\tau_s = L/v_s$ where L is the length of the material and v_s is the speed of sound in the material, dynamic stresses are generated in addition to quasi-static stresses. They are the result of the fact that the impacted material cannot expand as rapidly as it is heated due to its mass inertia. In fact a compressive stress wave will travel at the speed of sound from the heated region towards the external faces of the material, where the expansion will begin. The compressive stress wave will then be reflected as a tensile stress wave travelling towards the centre



Figure 4.9: Beryllium rods for the neutrino target installed at the SPS designed to be impacted by 1×10^{13} protons with a momentum of $300 \text{ GeV } c^{-1}$. The device on top was accidentally hit by an off-axis beam, leading to permanent bending and failure of the rod [58].

of the material. If the propagation time of sound through the material, τ_s , is shorter than the heating time, τ_h , the dynamic stress is reduced by τ_s/τ_h .

The superposition of the quasi-static stresses and dynamic stresses can lead to damage or to destruction of the impacted material. As an example, a beryllium rod damaged due to thermal stresses induced by the impact of an off-axis beam with 1×10^{13} protons with a momentum of $300 \text{ GeV } c^{-1}$ is shown in Fig. 4.9. These phenomena were studied analytically in greater details for simple geometries in [51, 52, 53, 54] and compared to experimental measurements in [55]. Numerical methods are necessary to study cases with more complex geometries and cases in which it is expected that the stress levels reach the damage limits of the material [56, 57].

4. BEAM-MATTER INTERACTION

5

Damage of Superconducting Magnets and their Components

In this chapter, the basic concepts of superconductivity relevant for this thesis are introduced, followed by a description of the special properties of Nb-Ti and Nb₃Sn superconductors, and the design of the main LHC and HL-LHC superconducting magnets is presented. Finally, their most critical components are identified and the different degradation mechanisms due to instantaneous beam impact are discussed.

5.1 General overview of superconductivity

Superconductivity was discovered by H. Hamerlingh Onnes in 1911 [59], when he was investigating the electrical resistance of metals at very low temperature, using liquid helium. He and his co-worker observed that the resistance of a mercury wire disappeared when the sample was cooled to temperature slightly below 4.2 K [60]. The discovery of many superconducting metals, including alloys and compounds, followed.

5.1.1 Superconducting properties

From their magnetic properties, superconductors are classified into two groups: type I, mainly elementary metals and type II, hard metals, alloys or compounds. Superconductors for accelerator magnets belong to the type II superconductors.

When an external magnetic field is applied to a type I superconductors the field is expelled from its interior up to the critical field H_c . A thin surface layer carries the shielding currents, which expel the external field. This behaviour is called the Meissner effect [61]. The superconductor is said to be in the Meissner state. The critical field

5. DAMAGE OF SUPERCONDUCTING MAGNETS AND THEIR COMPONENTS

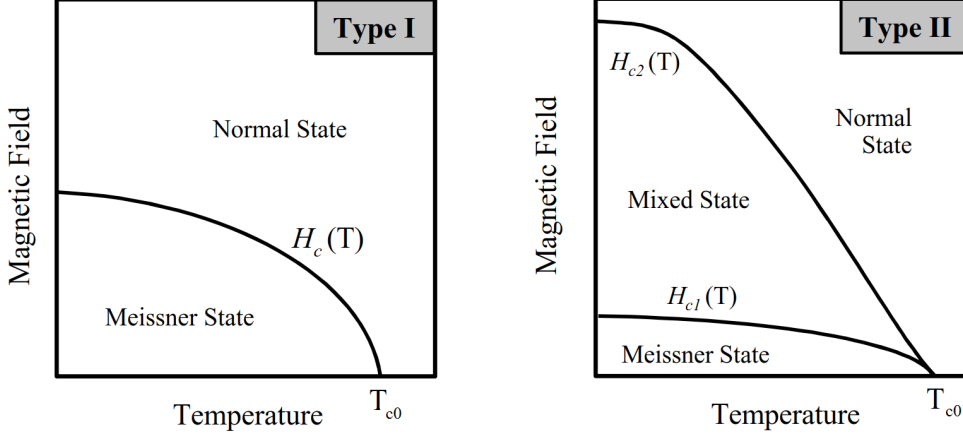


Figure 5.1: Schematics of the H - T phase space for type I (left) and type II superconductors (right). Type I has one critical field (H_c), while type II has a lower and upper critical field (H_{c1} and H_{c2} , respectively). Below $H_c(T)$ and $H_{c1}(T)$ lines, the magnetic field is completely excluded from the interior of the superconductor (Meissner state). Above $H_c(T)$ and $H_{c2}(T)$ lines, the material is no longer superconducting. Between $H_{c1}(T)$ and $H_{c2}(T)$ lines, magnetic flux can penetrate into the superconductor forming the so-called mixed state. T_{c0} is defined as the critical temperature at zero magnetic field. [63]

H_c depends on the temperature and reaches zero at the transition temperature T_{c0} . This behaviour is shown in Fig. 5.1(left). The critical field of these superconductors is usually low. In Tantalum, which exhibits the highest critical field, $\mu_0 H_c$ reaches only 83 mT at 0 K [62].

Type II superconductors are characterized by two critical fields, a lower H_{c1} and an upper H_{c2} as shown in Fig. 5.1(right). Below the $H_{c1}(T)$ line, type II superconductors are in the Meissner state and behave like a type I superconductor. When the external field is increased above the $H_{c1}(T)$ line, the superconducting state remains but the magnetic field can penetrate into the superconductor. This is called the mixed state. Above the $H_{c2}(T)$ line, superconductivity vanishes and the material is in the normal conducting phase. H_{c1} and H_{c2} are temperature dependent and zero at the critical temperature T_{c0} . H_{c20} is defined as the critical field at 0 K and zero current density and T_{c0} as the critical temperature at zero magnetic field and current density. $H_{c2}(T)$ of type II superconductors are usually much higher than of type I superconductors. For example $\mu_0 H_{c2}$ of Nb_3Sn at 4.2 K is about 22 T.

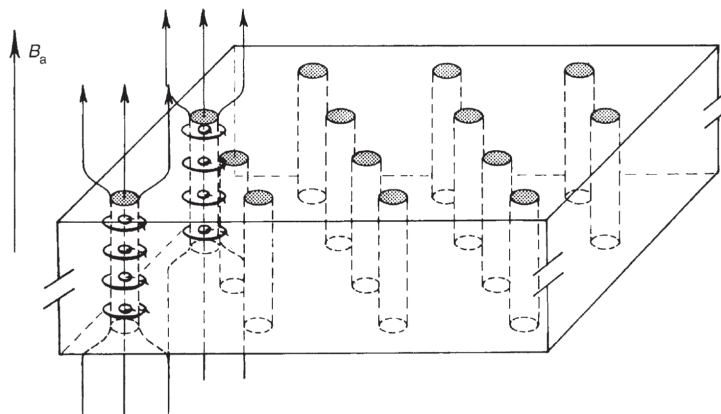


Figure 5.2: Schematics of a superconductor in the mixed state with the magnetic flux lines (arrows) and shielding currents (vortices around the flux lines). The magnetic field and the shielding currents are shown only for two fluxoids. [65]

Pinning force

In most applications, technical superconductors as for accelerator magnets, are operated in the mixed state, i.e. the magnetic field is above H_{c1} and the magnetic flux lines enter the superconductor in discrete quanta called fluxoids. Each fluxoid carries one magnetic flux quantum within a non-superconducting (normal) core of radius ξ surrounded by a vortex of shielding currents of radius λ . ξ and λ are called respectively the coherence length and the penetration depth deduced from the Ginzburg-Landau theory [64]. As the magnetic field is increased, the fluxoids move closer together up to H_{c2} , when the fluxoid normal cores overlap and superconductivity is lost. Fig. 5.2 shows schematically a superconductor in the mixed state with the magnetic flux lines and vortices of shielding currents.

When a transport current flows through the superconductor perpendicular to an applied field H , the fluxoids experience a Lorentz force F_L perpendicular to the applied field and the current direction. This force can result in a movement of fluxoids. Fluxoid motion causes energy dissipation, which results in the appearance of an electrical resistance [65]. In type II superconductors, fluxoids are energetically bound to favourable locations, so-called pinning centres. All kind of inhomogeneities can act as pinning centres, e.g. grain boundaries, precipitate, lattice dislocations, etc. As long as the Lorentz force F_L is smaller than the pinning force F_p , fluxoids can not move. This equilibrium holds up to the critical current density J_c when $F_L = F_p$, above J_c the fluxoids start to move and superconductivity is lost. At J_c , the pinning force F_p is

5. DAMAGE OF SUPERCONDUCTING MAGNETS AND THEIR COMPONENTS

given by [62]:

$$\vec{F}_p = \vec{J}_c \times \vec{B} \quad (5.1)$$

where \vec{B} is the magnetic flux density perpendicular to the current direction. The size and density of the pinning centres can be optimized during manufacturing to reach high F_p values and thus high J_c for a specific operation temperature and magnetic field.

Scaling laws

The pinning force F_p in the superconductor usually follows a magnetic field and temperature scaling law in the following form [66]:

$$F_p(H_\perp, T) = C(T)b^p(1 - b)^q, \quad (5.2)$$

where $b=H_\perp/H_{c2}(T)$ is the reduced field and $C(T)$, p and q are constants involving information on the micro-structure of the superconductor. Typically for Nb-Ti superconductor, p and q values vary between 0.5–0.9 and 0.75–1.1 respectively [67]. In the Kramer model [68], which describes well the pinning behaviour in Nb₃Sn, p and q are fixed to 0.5 and 2.

From this scaling law, it is also possible to obtain the critical surface of a superconductor. The critical surface describes the boundary between the superconducting state and the normal resistive state in a three dimensional space defined by the temperature, the magnetic field and the current density. An example of critical surface for Nb-Ti is given in Fig. 5.3, below the surface the material is superconducting above it is resistive.

The critical upper field H_{c2} also obeys a scaling law on temperature [69]

$$H_{c2}(T) = H_{c20}\left(1 - \left(\frac{T}{T_{c0}}\right)^n\right), \quad (5.3)$$

where n is equal to 1.7 for Nb-Ti [69] and 1.52 for Nb₃Sn [70].

Magnetization

To explain magnetization of a superconductor, consider a cylindrical infinite superconducting filament with a diameter d_f in a varying external magnetic field. The filament carries no transport current and is initially in a virgin state. A uniform magnetic field is applied perpendicularly to the filament axis and is ramped up. Shielding currents with a current density of J_c are induced in a shell at the outer layer of the filament with an elliptical inner boundary and circulate in opposite direction in the shell sides as represented in Fig. 5.4(a). If the magnetic field is further increased, the whole filament

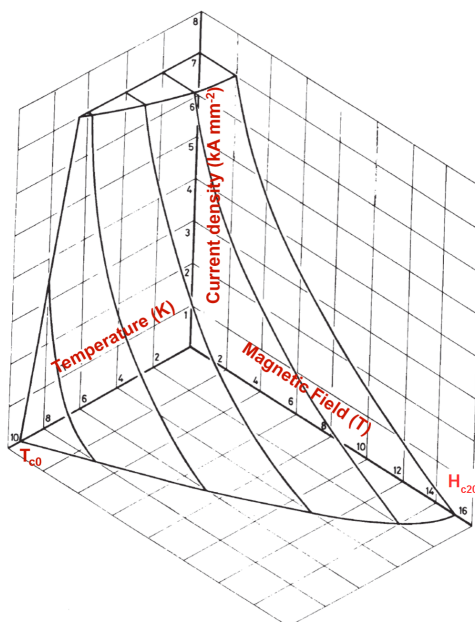


Figure 5.3: The critical surface for a Nb-Ti superconductor. Below the surface the material is superconducting and above it normal conducting. T_{c0} is about 9.2 K and H_{c20} about 14.5 T. [59]

is filled with shielding currents as in Fig. 5.4(b). The field at which this occurs is called the penetration field. For fine Nb-Ti or Nb₃Sn filaments such as the ones used in the LHC and its future upgrade, the penetration field is way below 1 T [71]. After reaching a maximum value above the penetration field, the magnetic field is decreased. A new shell is created in the outer layer of the filament where shielding currents flow in the opposite direction as in the inner shell, as in Fig. 5.4(c). If the field is further decreased, the outer layer grows until the current density is the negative of the Fig. 5.4(b). The induced shielding currents produce a magnetic moment and hence a magnetization that can be measured. Fig. 5.5 shows a typical magnetization per unit volume, M , of a superconducting filament. The superconductor is initially in a virgin state, and as the magnetic field is varied the shielding currents penetrate the superconductor as described previously in Fig. 5.4. ΔM describes the width of the magnetization hysteresis.

Based on the critical state model also called the Bean model [72], the magnetization per unit volume of fully-penetrated filament, M_f , can be expressed as:

$$M_f = \frac{2}{3\pi} J_c d_f \quad (5.4)$$

5. DAMAGE OF SUPERCONDUCTING MAGNETS AND THEIR COMPONENTS

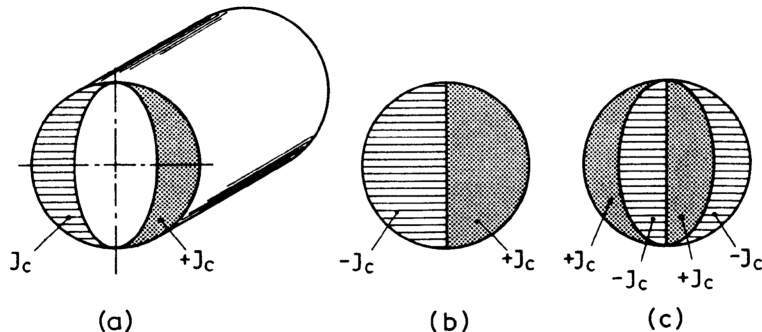


Figure 5.4: Model of superconducting filament magnetization. (a) After ramp up of the magnetic field applied perpendicularly to the filament axis from a virgin state, shielding current with a magnitude J_c are induced in a shell at the outer layer of the filament. (b) If the magnetic field is further increased, the filament is fully penetrate by shielding current. (c) Then the magnetic field is ramp down, a new shell of a shielding current is create in the outer layer of the filament with opposite direction as in the inner shell. [71]

where J_c is the critical current density and d_f is the effective filament diameter. If the filament is subject to an oscillating magnetic field, the filament magnetization curve shows an hysteresis whose width per unit volume, ΔM_f , can be estimated as

$$\Delta M_f = \frac{4}{3\pi} J_c d_f \quad (5.5)$$

For a composite superconductor strand such as the ones used in the LHC, the hysteresis width of the magnetization per unit volume, ΔM_s , can be written as

$$\Delta M_s = \frac{4}{3\pi(\alpha + 1)} J_c d_f \quad (5.6)$$

where α is the volumetric ratio of copper to superconductor [73][74].

5.1.2 Nb-Ti and Nb₃Sn superconductor

Accelerator magnets are built from cables made of cylindrical strands, made of superconducting filaments twisted together and embedded in an Oxygen-Free High-Conductivity (OFHC) copper. The LHC superconducting magnets use the metallic alloy Nb-Ti. For HL-LHC and other future accelerators such as FCC or HE-LHC, it is foreseen to implement magnets with superconducting cables based on the inter-metallic compound Nb₃Sn. Both Nb-Ti and Nb₃Sn are type II superconductors.

One of the earliest phenomena observed in superconducting magnets was flux jumping. In a rising magnetic field, if the heat produced by the fluxoid motions in the superconductor cannot escape rapidly enough, the temperature inside the superconductor

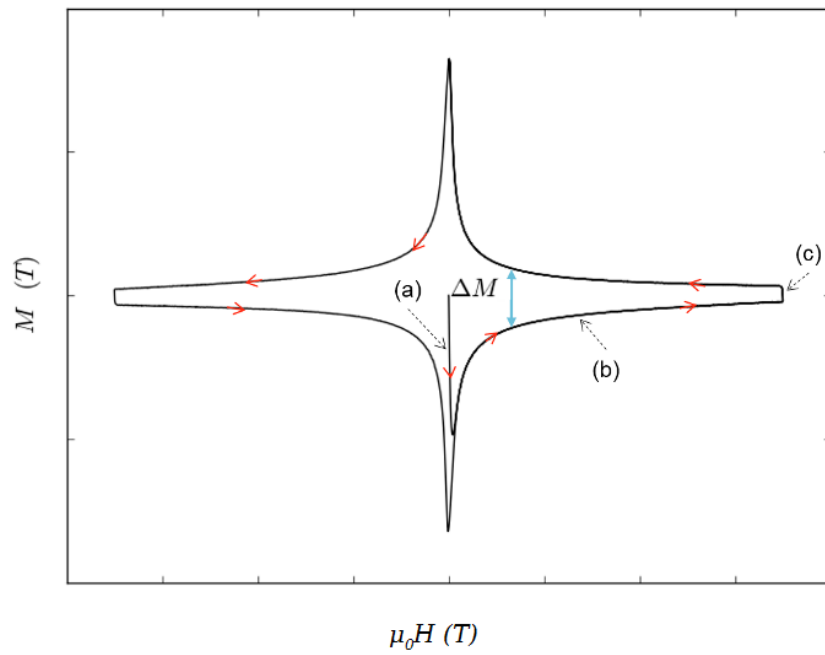


Figure 5.5: Magnetization curve, M , of a superconducting filament as function of the external field H perpendicular to the filament axis. The filament is initially in a virgin state. The red arrows indicate the direction of the magnetic field sweep. The width of the magnetization hysteresis ΔM is the difference between the upper and the lower branch of the curve as indicated by the blue arrow. (a), (b), (c) refer to the different illustrations in Fig. 5.4 where the shielding current distribution in the filament during the variation of the magnetic field is described.

5. DAMAGE OF SUPERCONDUCTING MAGNETS AND THEIR COMPONENTS

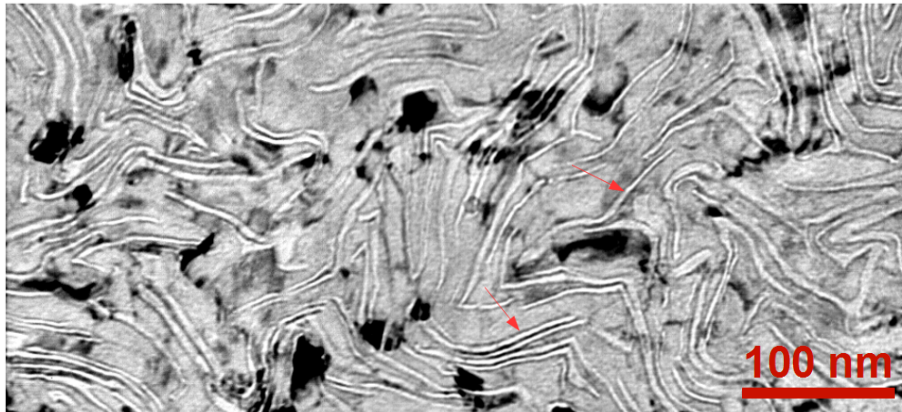


Figure 5.6: A transmission electron microscope image of the micro-structure of Nb-Ti filaments with a Ti weight fraction of %. The transverse cross-section reveals densely folded α -Ti phases (light grey and the red arrows indicate two titanium precipitates) which have a thickness of 1 nm to 4 nm and in between β -Nb-Ti phases (dark grey). [77]

increases and triggers a runaway condition known as flux jump, which can cause a magnet quench. The superconductor is driven into the resistive state at fields and currents low in comparison with its critical values. A solution to reduce flux jumps is to have fine superconductor filaments (few μm up to $\sim 100 \mu\text{m}$ diameter) such that the heat generate can be easily conducted to the filament surface.

At cryogenic temperatures, copper has a much lower resistivity and much higher heat conductivity than the superconductors in resistive state [75]. Therefore in case of a magnet quench, the copper provides a path for the magnet current and a efficient heat conduction, limiting the temperature rise and is used as a stabilizer

Nb-Ti alloy

Nb-Ti has a T_{c0} of about 9 K and a B_{c20} of about 14.5 T [67]. The superconductivity of Nb-Ti was discovered in 1961 by J. K. Hulm [76].

There are two stables phases in the Nb-Ti alloy, the body-centred cubic phase, referred as β -Nb-Ti phase and the hexagonal closed-packed phase rich in titanium (about 95% in weight) called α -Ti phase. When cooled down below the critical temperature, the β -Nb-Ti becomes superconducting while the α -Ti remains resistive and act as pinning centres. In Fig. 5.6, the micro-structure of a Nb-Ti alloy is revealed by transmission electron microscopy. The β -Nb-Ti phase is in dark grey and the α -Ti phase is in light grey with a thickness between 1 nm and 4 nm.

5.1 General overview of superconductivity

The critical current density J_c at a specific magnetic field and temperature depends strongly on the size and spacing of the α -Ti precipitates. Therefore during manufacturing the distribution of the α -Ti precipitates is optimized through multiple cycles of heat treatment and wire drawing. The micro-structure of Nb-Ti alloy during the different steps of manufacturing is shown in Fig. 5.7, the β -Nb-Ti phase in dark grey and the α -Ti phase in light grey. The heat treatments for several hours at temperature between 650 K and 700 K lead to diffusion and precipitation of Ti at the grain boundaries forming α -Ti precipitates. The longer the heat treatment is, the larger the α -Ti precipitates get. Between heat treatments, the micro-structure is deformed by wire drawing to reduce α -Ti precipitates dimensions and to increase the density of grain boundary thereby increasing the diffusion rates of Ti. Several cycles of strain/heat treatment are necessary to reach the optimum size and density of α -Ti precipitates. In the final state, the α -Ti phase represents typically 15% to 20% of the superconductor volume with typical thickness in nm ranges. [77, 78]

Like J_c , the pinning force density F_p depends on the distribution of the α -Ti precipitates. In Fig. 5.8, F_p is plotted as a function of the reduced field b measured at 1.8 K and 4.2 K on Nb-Ti samples processed with different conditions: only wire drawing (CW), one cycle of wire drawing and a heat treatment at ~ 700 K (HT) and one cycle of wire drawing, a heat treatment and a final wire drawing (HT+CW). The shape of the F_p - b curves and the F_p magnitude depend on the processing of the samples and thus on its micro-structure. Deforming Nb-Ti (CW) shifts the peak of the curve toward higher b while heat treatments (HT) shifts it toward lower b . The samples heat treated and deformed (HT+CW) exhibit the largest F_p with a peak value around $b=0.5$. [66]

The critical field and temperature Nb-Ti are mainly determined by the alloy composition. As shows in Fig. 5.9, H_{c2} peaks sharply between a Ti weight content of 40% and 50%, while the critical temperature shows a much smaller change and has a peak at Ti weight content of 25%.

Nb₃Sn compound

Superconductivity in Nb₃Sn was discovered in 1954 by B. Matthias [79]. Nb₃Sn is an inter-metallic compound belonging to the A15 crystallographic family. The A15 compounds with a chemical formula A₃B (where A is a transition metal and B can be any element) are characterized by their structure. The B atoms for a body-centered cubic crystal with two A atoms on each face, as shown for Nb₃Sn in Fig. 5.10. One important challenge for the use of Nb₃Sn is its brittleness and the strong dependence of

5. DAMAGE OF SUPERCONDUCTING MAGNETS AND THEIR COMPONENTS

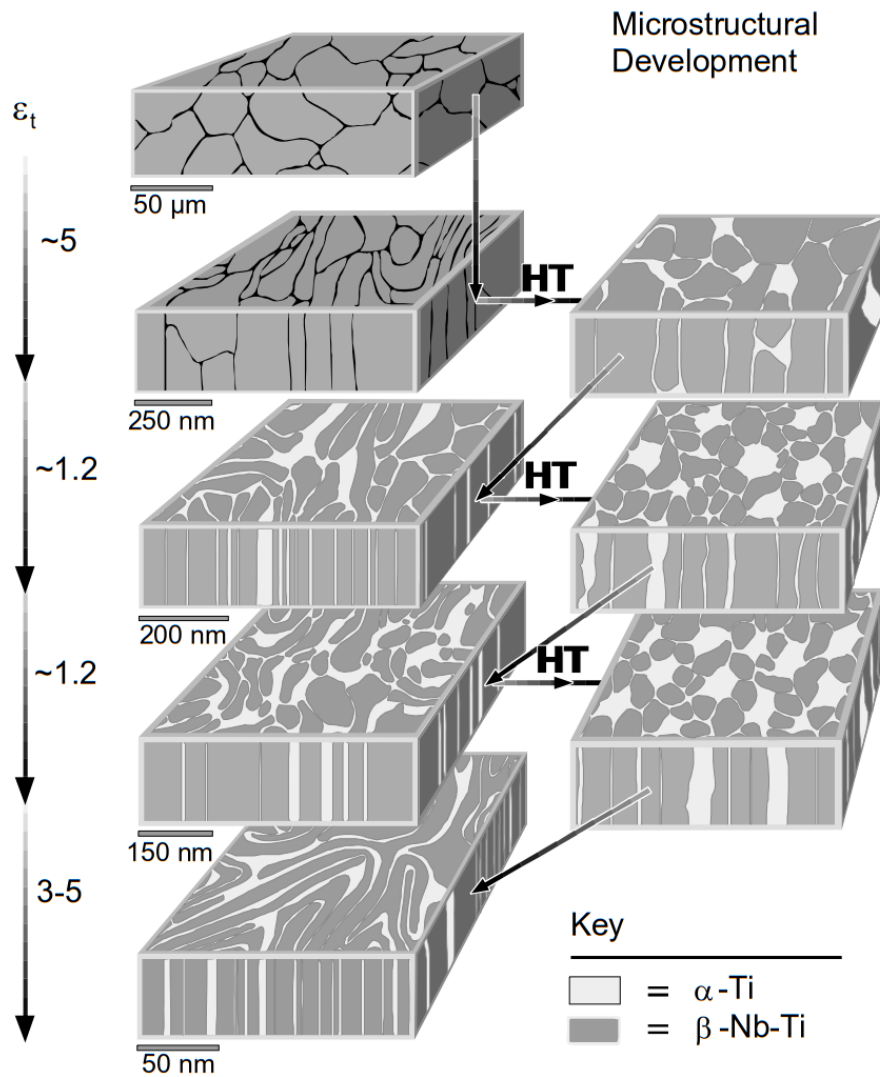


Figure 5.7: Development of the Nb-Ti micro-structure during the different steps of manufacturing. Several cycles of wire drawing with different strain, ϵ_t , and heat treatment (HT) are necessary to reach the optimum size and spacing of the α -Ti phases. Initially the alloy is composed only of β -Nb-Ti grains. While at the end the α -Ti phase represents $\sim 20\%$ of the volume with typical thickness in the order of nm. [77]

5.1 General overview of superconductivity

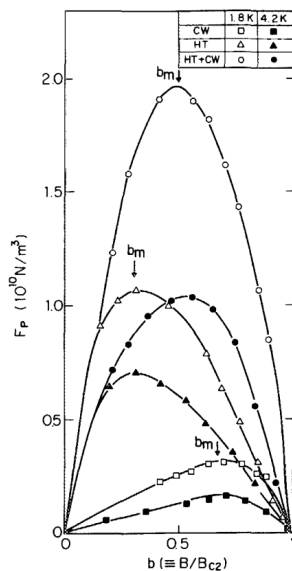


Figure 5.8: Pinning force density measured at 1.8 K and 4.2 K in several Nb-Ti samples as a function of reduced field b . The samples were manufacture with different steps: only wire drawing (CW), wire drawing + heat treated at $\sim 700 \text{ K}$ (HT) and wire drawing + heat treated at $\sim 700 \text{ K}$ (HT) + final wire drawing (HT + CW). [66]

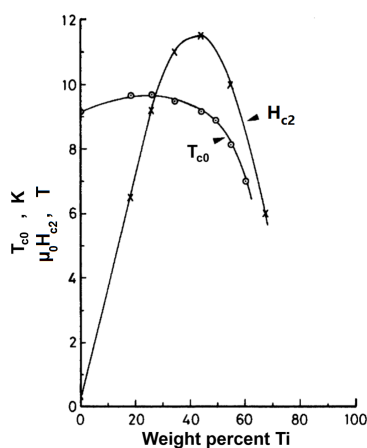


Figure 5.9: Influence of Ti content on critical temperature, T_{c0} and on upper critical field at 4.2 K, H_{c2} of Nb-Ti alloy [62].

5. DAMAGE OF SUPERCONDUCTING MAGNETS AND THEIR COMPONENTS

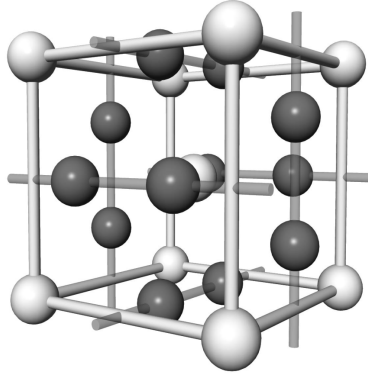


Figure 5.10: The A15 crystal structure of Nb_3Sn . The dark spheres are Nb atoms and the light spheres are Sn atoms. The Sn atoms form a body-centred cubic crystal structure with 2 Nb atoms forming mutually orthogonal chains across the faces. [63]

J_c on the applied stress and strain. This will be discussed in greater detail in section 5.3. Nb_3Sn has a T_{c0} of about 18 K and a B_{c20} of about 29.5 T [80].

T_c and H_{c20} have been shown to depend strongly on the Sn content. As illustrated in Fig. 5.11, the critical temperature peaks at about 18 K for with 25% of atomic Sn content and H_{c20} at about 30 T with 24-24.5% of atomic Sn content.

Regarding J_c , the general understanding is that the grain boundaries function as the primary pinning centres. This is supported by strong experimental evidence in which the maximum pinning force density is related to the reciprocal grain size and, thus, the grain boundary density. Fig. 5.12 shows the measured pinning force density as a function of the average and reciprocal grain size. Hence to achieve high F_p and, thus, J_c , Nb_3Sn must be processed such to obtain a fine and homogeneous grain structure. The grain size also impacts on the magnetic field strength at which the F_p is reaching its maximum. In Fig. 5.13, the reduced pinning force (F_p/F_{pmax}) is plotted as a function of the reduced field b for samples with different grain sizes. One can see that the peak of reduced pinning force moves towards lower reduced field as the grain size grows.

There are different processes to manufacture Nb_3Sn wires. The three main ones are: bronze process, internal-tin process (IT) and the Powder-in-Tube (PIT) process (Fig. 5.14). The so-called restacked-rod process (RRP) is an internal-tin type. They require heat treatment of several hours with temperatures up to 900 K to form the Nb_3Sn [83]. A diffusion barrier is requested to prevent the diffusion of Sn in the surrounding copper. As the reacted Nb_3Sn compound is brittle, the coil winding is performed before the heat treatment.

5.1 General overview of superconductivity

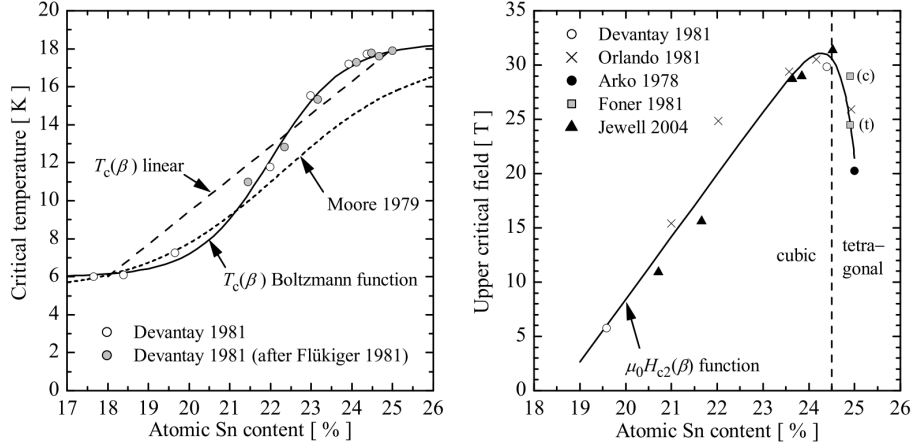


Figure 5.11: The critical temperature T_{c0} (left plot) and upper critical field at zero temperature H_{c20} (right plot) as function of Nb-Sn composition. The $T_c(\beta)$ Boltzmann function and the $\mu_0 H_{c2}(\beta)$ function are empirical relations. [81]

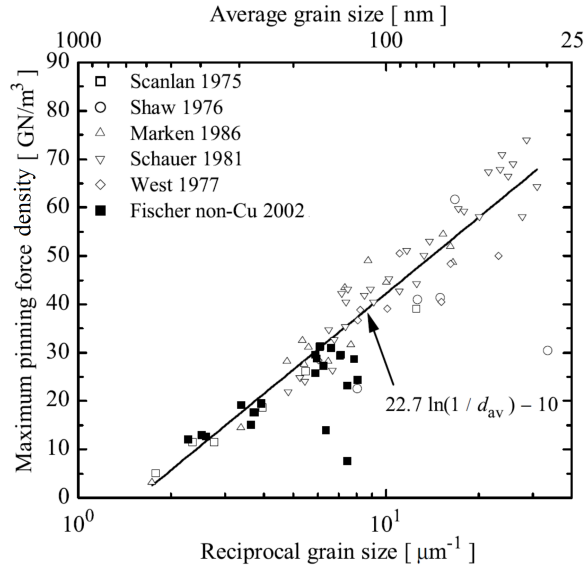


Figure 5.12: Maximum pinning force density F_p measured at ~ 5 T and 4.2 K as function of reciprocal grain size in Nb_3Sn . The line shows the results of data fitting with the obtained fit equation. Data compiled by A. Godeke [81].

5. DAMAGE OF SUPERCONDUCTING MAGNETS AND THEIR COMPONENTS

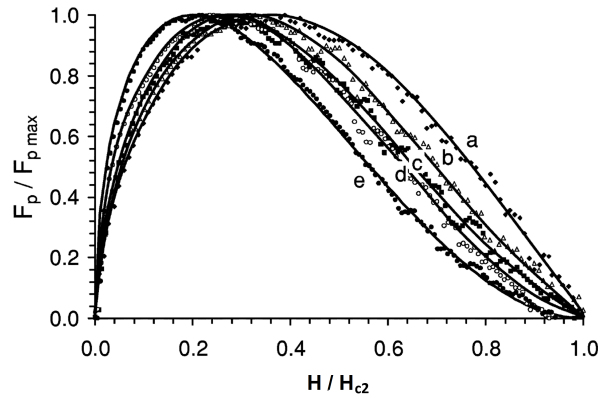


Figure 5.13: Reduced pinning force density ($F_p/F_{p,max}$) as function of the reduced field ($b=H/H_{c2}$) for several Nb_3Sn wires (a to e) with different manufacturing process parameters at a temperature such that the upper critical field H_{c2} is close to 1 T. Sample *a* had the shortest heat treatment time thus the smallest grain size, while sample *e* had the longest heat treatment time thus the largest grain size. The solid lines were obtained with a scaling law. [82]

5.2 Superconducting magnets

In this section, the design of the superconducting magnets of LHC and HL-LHC are presented.

5.2.1 LHC Nb-Ti magnets

The LHC superconducting magnets are all based on copper stabilized Nb-Ti superconductor operating at 1.9 K or 4.5 K. The LHC superconducting magnets can be classified in two types:

- The magnets using Rutherford superconducting cables insulated with polyimide films, as for examples the main dipoles (MB), main quadrupoles (MQ), matching quadrupoles (MQM), wide aperture quadrupole (MQY) and single bore dipoles and quadrupoles in the insertion regions.
- The corrector magnets ranging from dipoles to dodecapoles using enamel insulated ribbon superconducting cables impregnated with epoxy resin.

The design of the several types of LHC magnets using Rutherford superconducting cables is based on the same concept. The magnets are composed of several coils wound with superconducting cables around the beam pipe. The coil's shape is optimized to maximize the magnetic field on the beam axis and achieve a high field quality. The

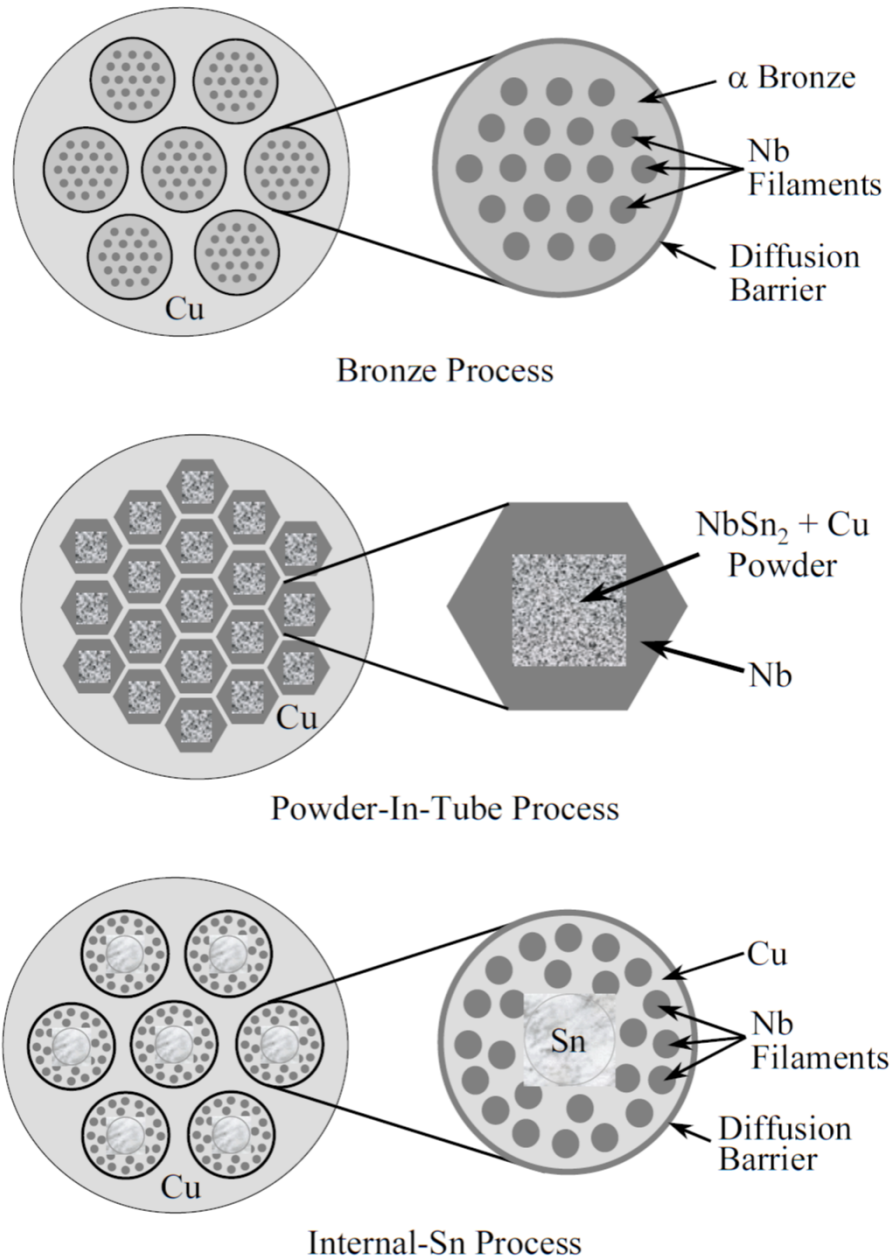
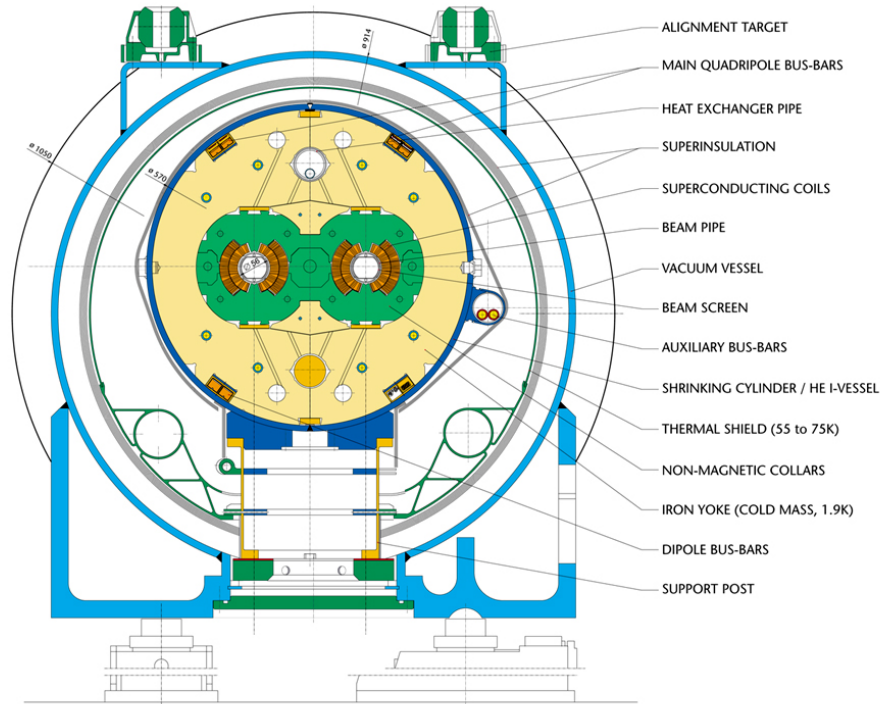


Figure 5.14: Schematics of the three main Nb₃Sn wire fabrication techniques: bronze, Powder-in-Tube (PIT) and internal-Sn (IT). All processes use diffusion to form Nb₃Sn from a Sn source. [63]

5. DAMAGE OF SUPERCONDUCTING MAGNETS AND THEIR COMPONENTS

LHC DIPOLE : STANDARD CROSS-SECTION



CERN AC/DI/MM - HE107 - 30 04 1999

Figure 5.15: Cross section of LHC main dipole. The two particle beams are circulating in opposite direction in the two beam pipes equipped with beam screens. The superconducting coils (orange) are on each side of the two beam pipes. The steel collars (green) and the iron yoke (yellow) guarantee the mechanical stability and rigidity of the coils. The cryostat (dark blue) is filled with super-fluid helium. The overall assembly is enclosed in a vacuum vessel (light blue).

mechanical stability and rigidity of the coils are guaranteed by steel collars and an iron yoke. The overall is enclosed in a cryostat for cooling the magnet to the operating temperature. To protect the coils from the consequences of a quench, quench heater strips are placed between the steel collars and the coils [23]. As an illustration, the cross section of the LHC MB is shown in Fig. 5.15. The MB magnet is a twin-aperture magnet with a 56 mm coil aperture diameter. The beams are circulating in the two beam pipes equipped with beam screens. The beams screen reduces the heat load to the super-fluid helium bath. The superconducting coils are visible (orange) on each side of the two beam pipes surrounded by the steel collars (green) and the iron yoke (yellow). The cold mass is placed in a cryostat (dark blue) filled with super-fluid helium. The overall assembly is enclosed in a vacuum vessel (light blue). The MB is operating at

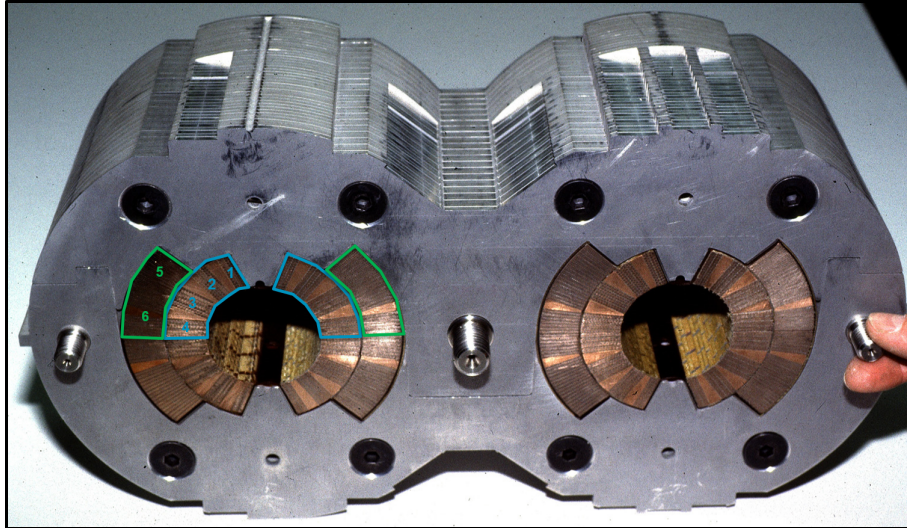


Figure 5.16: Prototype of the MBs with the two apertures and the four coils (two per apertures). Each coils is composed of six-conductor blocks - numbered from 1 to 6 - organized in two layers, inner layer (blue) and outer layer (green).

1.9 K and was designed to reach a nominal central magnetic field of 8.33 T at a nominal current of about 11.6 kA.

The coil layout of the MB is based on six-conductor blocks arranged in two nested layers, the so-called inner and outer layers, wound with Rutherford cables. A MB prototype with the two apertures and the four coils (two per aperture) is shown in Fig. 5.16. The six-conductor blocks per coils are numbered from 1 to 6, each conductor block is composed of several turns of cables.

The Rutherford cables consist of several multi-filamentary Nb-Ti strands and are insulated with three layers of polyimide. Fig. 5.17(a) shows a picture of a cable of the outer layer of the MBs with the Nb-Ti filaments visible at the left end of the cable. A cross section of the cable with 36 strands is shown in Fig. 5.17(b). Fig. 5.17(c) depicts the cross section of one of the strands with the Nb-Ti filaments in grey and the copper in light brown. A zoom on a group of filaments is shown in Fig. 5.17(d). The characteristics of the cable used in the MBs are detailed in Table 5.1, for other magnets such as MQ it can be found in [6] and for the insertion region magnets such as MQX and MQY in [84].

The cables of the MBs are insulated with three layers of polyimide as illustrated in Fig. 5.18. The two inner layers having a thickness of $50.8 \mu\text{m}$ are wrapped around the cable with an overlap of 50%. The third layer, with a thickness of $68.6 \mu\text{m}$, is wrapped in opposite direction with a spacing of 2 mm. The outer side of the third layer has

5. DAMAGE OF SUPERCONDUCTING MAGNETS AND THEIR COMPONENTS

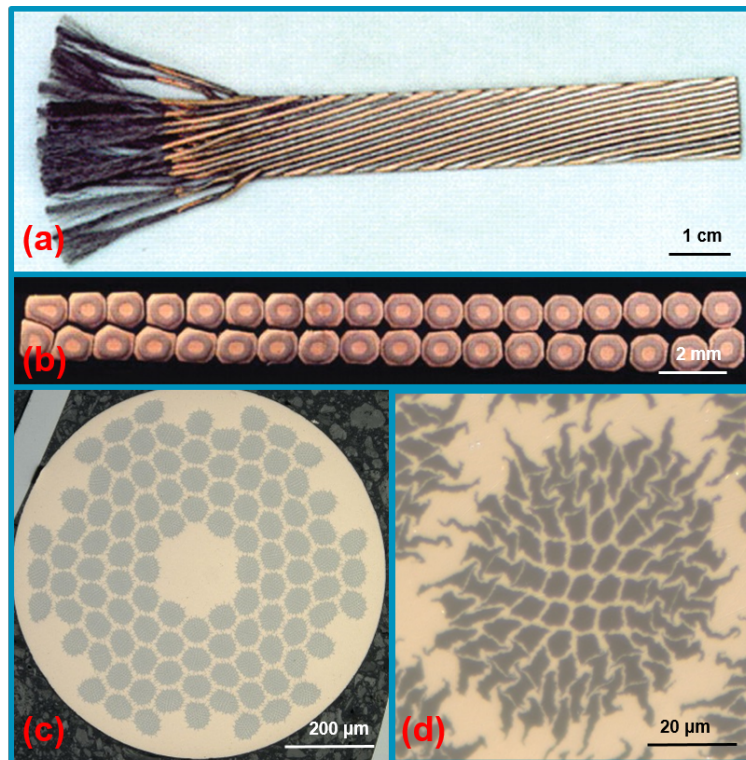


Figure 5.17: (a) A LHC MB outer layer cable with partially etched strands which show the Nb-Ti filaments at the left end of the cable. (b) Cross section of the cable with the 36 strands. (c) Cross section of one of the strands, the Nb-Ti filaments are visible in grey and the copper in light brown. (d) Zoom on one group of filaments. The average filament diameter is 6 μm .

Table 5.1: Strand and cable characteristics of the LHC main dipole [6]. The Nb-Ti superconductor has Ti weight content of 47% (Nb-47 wt.%Ti)

	Inner layer	Outer layer
Strand		
Diameter (mm)	1.065 ± 0.0025	0.825 ± 0.0025
Copper to superconductor ratio α	1.65 ± 0.05	1.95 ± 0.05
Filament diameter d_f (μm)	7	6
Number of filaments	~ 8900	~ 6500
Critical current (A) 10 T, 1.9 K	≥ 515	
9 T, 1.9 K		≥ 380
ΔM_s at 0.5 T and 1.9 K (mT)	≤ 30	≤ 23
Cable		
Number of strands	28	36
Cable dimension (at room temperature)		
Mid-thickness at 50 MPa (mm)	1.900 ± 0.006	1.480 ± 0.006
Thin edge (mm)	1.736	1.362
Thick edge (mm)	2.064	1.598
Width (mm)	15.10	15.10
Keystone angle (degree)	1.25 ± 0.05	0.90 ± 0.05
Critical current (A) 10 T, 1.9 K	≥ 13750	
9 T, 1.9 K		≥ 12960

5. DAMAGE OF SUPERCONDUCTING MAGNETS AND THEIR COMPONENTS

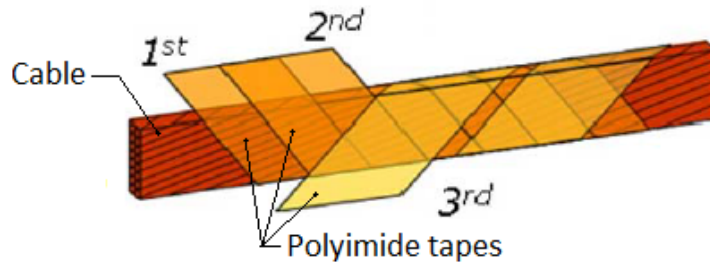


Figure 5.18: Superconducting cable insulated with its three layers of polyimide tape [85].

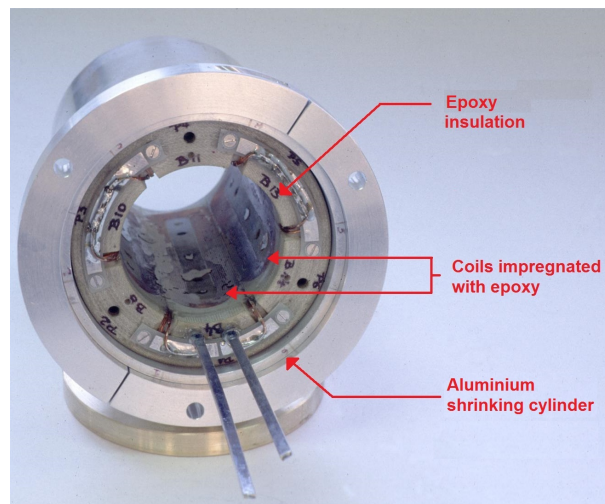


Figure 5.19: Prototype of a sextupole corrector magnets (MCS). The impregnated coils are packed in a layer of epoxy insulation placed into an iron yoke (not visible) and pre-stressed by means of an aluminium shrinking cylinder.

a polyimide based adhesive coating. The adhesive coating bonds itself at a minimum temperature of 458 K [6].

The LHC corrector magnets with nominal currents ranging from 50 A to 550 A are necessary for the correction of field errors and for the control and steering of the beams. A typical corrector magnet is composed of a number of coils wound from enamel insulated conductors impregnated with epoxy resin. These coils were assembled on a cylindrical surface packed in a layer of epoxy insulation and placed into the iron yoke and pre-stressed by means of an aluminium shrinking cylinder (see Fig. 5.19) [86][87]. The corrector magnets were fabricated using four different multi-filamentary Nb-Ti strand types coated with a layer of insulating enamel.

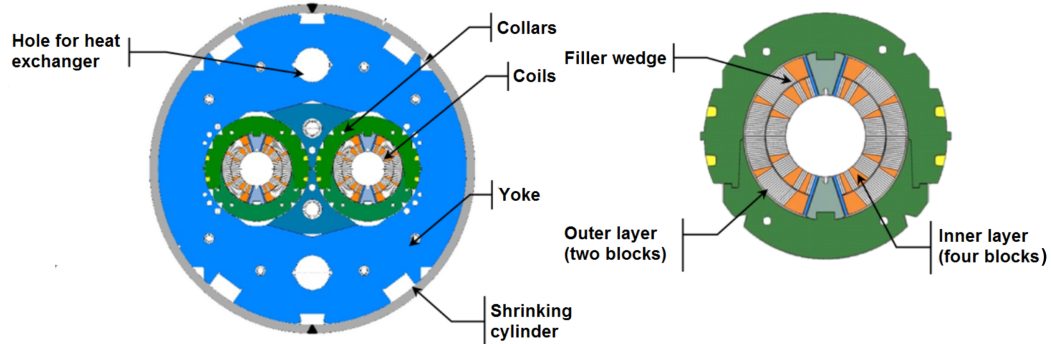


Figure 5.20: The left picture is a cross section of the 11 T dipole magnet for HL-LHC on the right: The coils are on each side of the two apertures maintained by the collars and the yoke. Inside the yoke, a hole is foreseen for the heat exchanger and around the yoke is the shrinking cylinder. The right picture is a zoom on the collar and coils of one aperture: the design of the coils is based on Nb_3Sn cables wound in two nested layers (inner and outer) arranged in six-conductor blocks.

5.2.2 HL-LHC Nb_3Sn magnets

In order to reach the performance goals of HL-LHC, new magnets have to be built. The most challenging are the Nb_3Sn short twin-aperture dipoles (so-called 11 T dipoles) and the low- β single aperture triplet quadrupoles.

The short twin-aperture dipole is required to replace one normal 14.3 m long LHC dipole by two 5.5 m long 11 T dipoles, to gain space for collimators. Therefore it needs to reach a nominal field of 11 T with a 56 mm aperture, operating at a current of 11.6 kA and a temperature of 1.9 K. Short models have already been manufactured and tested [88]. The cross-section of the 11 T magnet with its main elements (coils, collar and yoke) is shown in Fig. 5.20. The design of these magnets is based on Nb_3Sn cables wound in two nested layers and arranged in six-conductor blocks.

The Nb_3Sn low- β single aperture quadrupole to be installed in the insertion regions of IP1 and IP5 will feature a 150 mm aperture and an operating gradient of 132.6 T m^{-1} , which entails 11.4 T peak field at the coils at a current of 14.5 kA [89]. The cross-section of the quadrupole magnets is shown in Fig. 5.21. The mechanical stability of the Nb_3Sn coils is guaranteed by the aluminium shell, the iron yoke and the aluminium collars. The super-fluid helium is contained in the stainless steel vessel.

Both magnets are based on Rutherford cable composed of up to forty Nb_3Sn strands. Two types of strands are still considered: RRP and PIT. A stainless steel strip is embedded between the two layers of strands in the cable to reduce the effect of persistent

5. DAMAGE OF SUPERCONDUCTING MAGNETS AND THEIR COMPONENTS

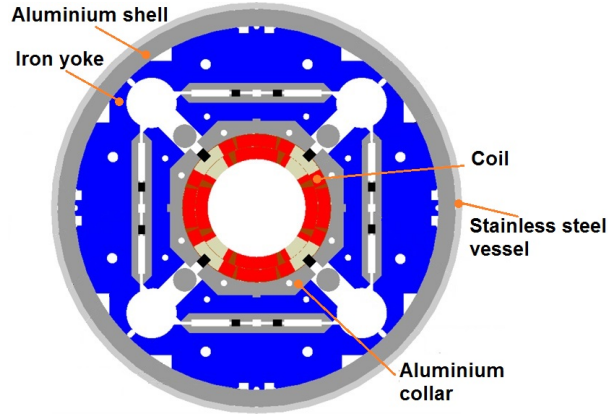


Figure 5.21: Cross section of the low- β single aperture triplet quadrupoles for HL-LHC. The aluminium shell and collars and the iron yoke guarantee the mechanical stability of the coils made of Nb₃Sn cables. The super-fluid helium is contained in the stainless steel vessel

currents. It is foreseen to insulate the cable either with E-glass tapes or Mica tapes. The coils are impregnated with an epoxy resin after reaction of the Nb₃Sn.

5.3 Damage mechanisms

In this section, the most critical components of superconducting magnets and their damage mechanisms are discussed.

5.3.1 Critical superconducting magnet components

The most critical components of superconducting magnets of the LHC and HL-LHC were identified as a function of their sensitivity to beam induced damage and the impact of their failure on the magnet performance.

The first critical components are the Nb-Ti and Nb₃Sn superconducting strands. If their critical current I_c is reduced, it will reduce the quench margin of the magnet meaning that at nominal current, usually acceptable perturbations (temperature fluctuation, beam losses, etc) could cause the magnet to quench. In the worst case the magnet will not reach its nominal magnetic field. The second critical component is the insulation of the superconducting cables. Damaged insulation could cause a short cable to ground or a short between cables (e.g. inter-turn short). In case of a short to ground, a replacement of the impacted magnet would most likely be required stopping the accelerator operation for several weeks [1]. An inter-turn short could be fatal for



Figure 5.22: Coil damage due to a inter-turn short in a LHC pre-series dipole.

the magnet during a quench or a fast power abort of the power converters. During a fast power abort, the current in the magnet drops inducing an inductive voltage in the magnet. If the turn to turn voltage is high enough, the current can flow through an inter-turn short with the risk of damaging the coils. In Fig. 5.22 is shown a picture of a coil damaged due to a inter-turn short in a LHC pre-series dipole.

As discussed in chapter 4, the impact of high energy particles can cause a fast temperature rise leading to stresses in the magnet. Several damage mechanisms have been studied in this work: the degradation of the polyimide insulation due to temperature increases and the degradation of the critical current of the superconducting cables due to heat and due to stresses. These mechanisms will be discussed in more detail in the following sections.

Damage induced by radiation impact due to integrated dose effect in the magnet components is not in the scope of this work. Nevertheless it is important to compare the radiation levels at which damage has been reported to the radiation levels expected during an instantaneous beam impact. The dielectric strength of the polyimide insulation degrades as function of the integrated dose. A loss of about 20% of the dielectric strength has been measured after an irradiation with 21 MeV protons and a fluence of 3×10^{22} protons m^{-2} [90]. Several studies report a degradation of J_c of Nb-Ti wires optimized for high field application after being exposed to radiation [91][92]. As an example, a 10% degradation of the J_c has been measured after exposure to a fluence of about 10^{22} protons m^{-2} with 15 MeV [92]. On the contrary for Nb₃Sn, it has been shown that J_c increases with integrated dose up to a maximum value and then decreases [93, 94]. An increase of more than 20% of the J_c of a RRP Nb₃Sn wire was measured after an

5. DAMAGE OF SUPERCONDUCTING MAGNETS AND THEIR COMPONENTS

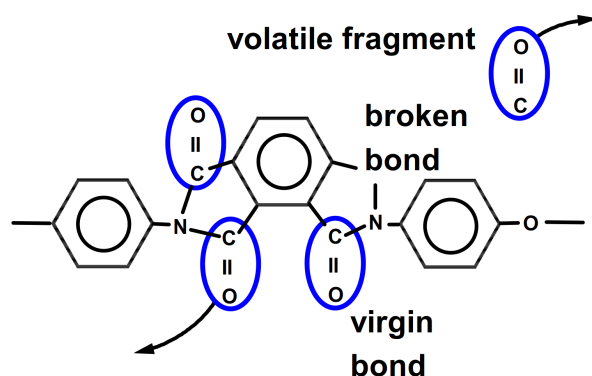


Figure 5.23: Monomer of the polyimide Kapton[®]. The polymer chain is first destroyed via the breaking of the imide rings, producing carbon monoxide (CO) [97].

irradiation fluence of 2.5×10^{20} protons m^{-2} with 65 MeV [95]. The radiation levels reported in these experiments are several orders of magnitude higher than what it is expected in case of an injection or extraction failure in the LHC ($\sim 10^{16}$ protons m^{-2} at 450 GeV c^{-1} and 7 TeV c^{-1}) and in the experiment with proton beam performed in the present study ($\sim 10^{18}$ protons m^{-2} at 450 GeV c^{-1}). Thus, changes due to the integrated dose are not expected as a consequence of an instantaneous beam impact.

5.3.2 Insulation degradation induced by temperature

When exposed to high temperature, the polyimide insulation of the superconducting cables can start to degrade. Manufacturers typically specify their polyimide films to be used up to 673 K [96].

Polyimide is a molecule made of monomers. Such a monomer is shown as example for the polyimide Kapton[®] in Fig. 5.23. When it is exposed to high temperature, a chain of chemical reactions is induced in the polyimide leading to its decomposition. The first step of this decomposition is the breaking of the imide rings, which contain nitrogen atoms, producing carbon monoxide (CO). The polyimide decomposition generates, furthermore, several gaseous and solid products. 95% of the solid products is carbon in the form of glassy carbon, which has a good conductivity [98]. Therefore the polyimide loses its insulating property during this process.

Mass loss is a good indication of the decomposition process [99]. A model of the temperature dependency of the mass loss was developed based on the reaction rate of the polyimide. A reaction model from [100] was fitted to experimental data on Kapton[®] provided by Dupont [96]. The mass loss was measured while the temperature was increased at a constant rate of 3 K min^{-1} within an helium atmosphere. The reaction

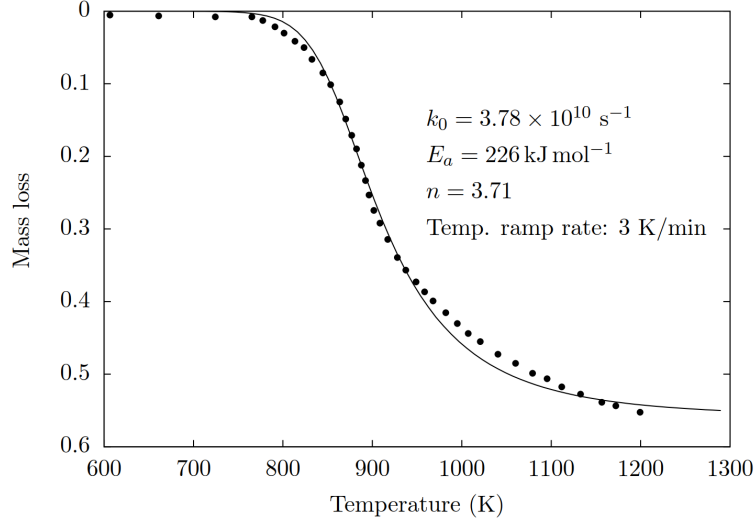


Figure 5.24: Fitting of the reaction rate model (equation (5.7)) in solid line to Kapton[®] data from Dupont [96] in round markers.

rate can be expressed as

$$\frac{1}{\alpha_f} \frac{d\alpha}{dt} = -k_0 \exp\left(-\frac{E_a}{RT}\right) \left(1 - \frac{\alpha}{\alpha_f}\right)^n, \quad (5.7)$$

where $\frac{d\alpha}{dt}$ is the reaction rate, α is the actual mass loss and α_f is the mass loss after the full degradation of the polyimide, which was set to 0.55. R is the ideal gas constant, T the temperature and k_0 , E_a and n are fitting parameters. The results of the fitting is shown in Fig. 5.24. The round markers are the data provided by Dupont and the solid line is the fitted reaction rate model. The mass loss is defined as

$$\alpha = \frac{(m_0 - m)}{m_0}, \quad (5.8)$$

where m is the actual mass and m_0 is the initial mass.

At constant temperature the solution of equation (5.7) is given by

$$\alpha(t) = \alpha_f - \alpha_f \left(1 - (1 - n)k(T)t\right)^{\frac{1}{1-n}}, \quad (5.9)$$

where $k(T) = k_0 \exp(-E_a/RT)$ and t is the exposure time in seconds. The exposure time at a constant temperature T required to obtain a certain mass loss α is then derived as

$$t_\alpha = \frac{1 - (1 - \alpha/\alpha_f)^{1-n}}{(1 - n)k(T)} \quad (5.10)$$

5. DAMAGE OF SUPERCONDUCTING MAGNETS AND THEIR COMPONENTS

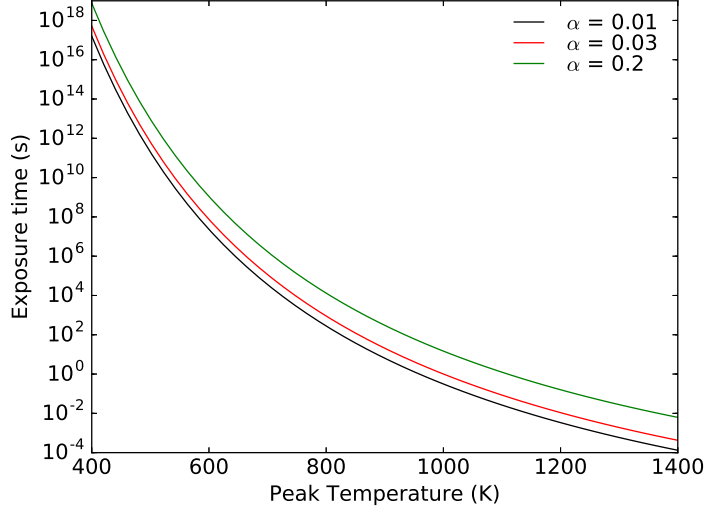


Figure 5.25: Exposure time as function of temperature to reach mass loss α of 0.01 (black), 0.03 (red) and 0.2 (green) for an isothermal exposure.

For $\alpha/\alpha_f \ll 1$, equation 5.10 simplify as:

$$t_\alpha = \frac{\alpha/\alpha_f}{k(T)} \quad (5.11)$$

For an isothermal exposure, the exposure time as a function of the temperature required to reach mass loss α of 0.01, 0.03 and 0.2 is shown in Fig. 5.25. The equivalence between different exposure times and temperatures can be clearly seen. As an example, an exposure to 750 K for 1000 s is equivalent to an exposure to 1300 K over 1 ms. Both are leading to a mass loss of 0.03.

5.3.3 Critical current reduction induced by temperature

An upper boundary for the degradation of the critical current of a superconducting cables when exposed to heat is the melting of the copper matrix. Once the copper starts to melt at 1358 K, it is assumed to be fatally damaged.

In Nb-Ti, the titanium can start to diffuse within the alloy at lower temperatures of about 650 K, resulting in a growth of the α -Ti precipitates. Size and spacing of the α -Ti precipitates have been optimized to maximize the strand J_c , thus, any modification of its micro-structure leads to a reduction of J_c . It was observed that a 5 minutes heat treatment of LHC main dipole Nb-Ti strands at 673 K causes a reduction of the critical current by more than 20% [101].

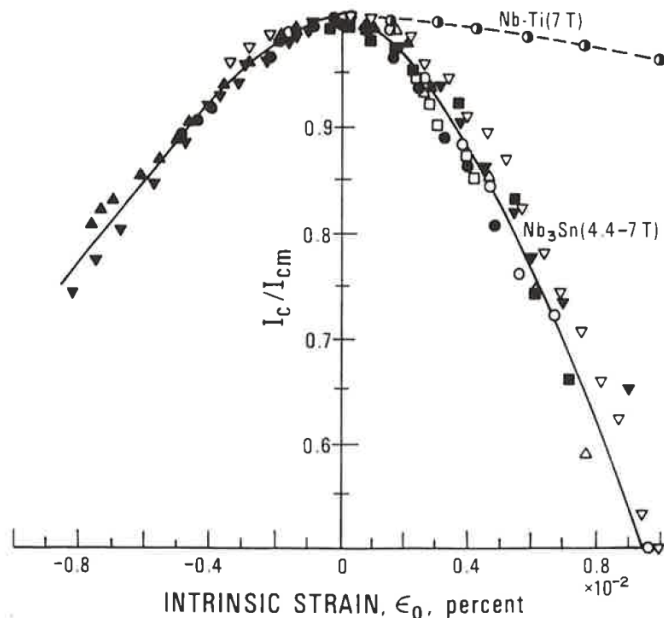


Figure 5.26: Compilation of measurements of the critical current of multi-filamentary Nb-Ti and Nb₃Sn wires as a function of the intrinsic strain ϵ_0 performed at field between 4.4 T to 7 T. I_c is normalized to its maximum value (strain free). Negative strain values indicate compression while positive values indicate tension [62].

In case of Nb₃Sn, the exposure to temperatures of about 900 K causes grain growth leading to a reduction of the pinning force F_p and critical current density J_c . In addition, Tin might diffuse from the filaments to form an alloy with the copper matrix, reducing the Tin content inside the filaments, which is critical for T_c and H_{c2} and, therefore, also affecting J_c .

5.3.4 Critical current reduction due to thermo-mechanical strain

As seen in chapter 4, temperature rise in a material induces thermal stresses and strains, which affect the critical current I_c of superconducting materials [102].

Fig. 5.26 shows the effect of strain on the critical current of Nb₃Sn and Nb-Ti wires for external field of 4.4 T to 7 T. It can be seen that Nb₃Sn is much more affected by strain than Nb-Ti.

If the strain applied on the superconductor wire stays below the so-called irreversible strain ϵ_{irr} , the decrease of the superconducting properties is reversible. If the strain is higher, then only partial recovery is observed. The recovery of critical current after application of a strain is higher in Nb-Ti than in Nb₃Sn [103, 104]. Fig. 5.27 shows the

5. DAMAGE OF SUPERCONDUCTING MAGNETS AND THEIR COMPONENTS

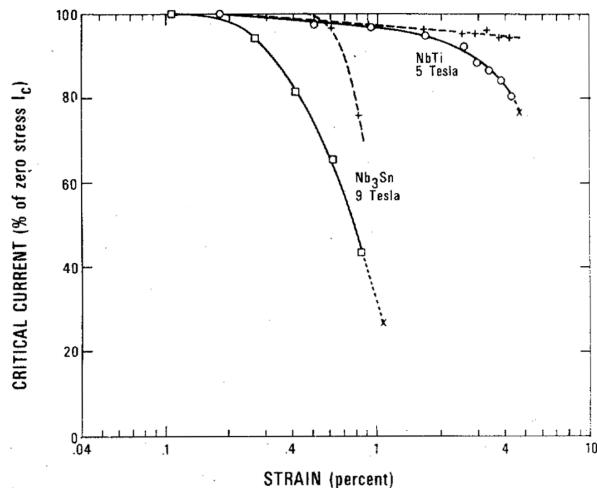


Figure 5.27: Critical current I_c degradation induced by strain measured in Nb-Ti and Nb₃Sn wires at 4 K and at 5 T for Nb-Ti and 9 T for Nb₃Sn. The dashed lines for each case indicate the critical current recovery value after unloading [104].

degradation of the critical current as function of intrinsic strain on Nb-Ti and Nb₃Sn superconductors and the recovery of the critical current after unloading. The recovery of Nb-Ti critical current is about 95% for strain up to several %. On the contrary Nb₃Sn recovers only 70% of its initial critical current after the application of 0.9% strain.

Critical current degradation below ε_{irr} can be explained by a variation of the intrinsic properties of the superconductor (i.e. H_{c2} and T_c) through strain induced lattice instabilities [81]. The strain dependency of T_{c0} , H_{c2} and I_c of a Nb₃Sn superconductor wire is shown in Fig. 5.28. I_c was measured at 16 T and 4.2 K and B_{c2} at 4.2 K. The intrinsic strain experienced by the superconductor is $\varepsilon_0 = \varepsilon_t - \varepsilon_m$, where ε_t is the tensile strain applied on the wire and ε_m is the compressive strain initially experienced by the superconductor ($\varepsilon_m = 0.5\%$). ε_m is caused by the difference of thermal contraction of the copper matrix and the superconductor during cool-down from heat treatment temperature (~ 900 K) to 4.2 K. I_c reaches its maximum when $\varepsilon_0 = 0$ and thus, when $\varepsilon_t = \varepsilon_m$. For $\varepsilon_t = 0.8\%$, i.e. $\varepsilon_0 = 0.3\%$, T_c is decreased from 17.4 K to 17.1 K, B_{c2} from 20 T to 19 T and I_c from 48 A to 30 A.

For large strain above ε_{irr} , the I_c degradation is either due to filament breakage or to residual strain on the superconductor filaments induced by the plastically deformed copper matrix. The intrinsic irreversible strain ε_{irr} of Nb₃Sn has been measured in [106] on several type of Nb₃Sn wire and varies between 0.04% and 0.25%.

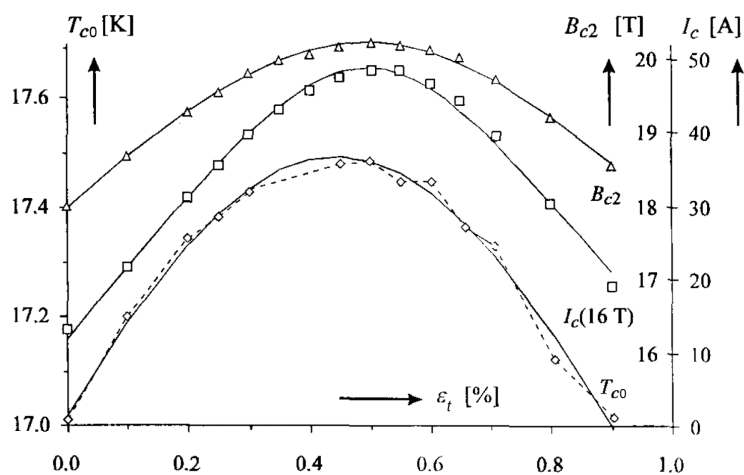


Figure 5.28: T_{c0} (diamond markers), B_{c2} (triangular markers) and I_c (square markers) as function of an applied uniaxial tensile strain ε_t in a Nb_3Sn superconductor wire. The lines are obtained from a strain dependence model of the superconducting properties of Nb_3Sn . I_c was measured at 16 T and 4.2 K and B_{c2} at 4.2 K. Initially the superconductor is under a compressive pre-strain ε_m due to the difference of thermal contraction of the copper matrix and Nb_3Sn during cool-down from the heat treatment at ~ 900 K to 4.2 K. This pre-strain is compensated at $\varepsilon_t \sim 0.5\%$ when I_c reaches its maximum [105].

5. DAMAGE OF SUPERCONDUCTING MAGNETS AND THEIR COMPONENTS

6

Experimental Road Map

In order to study the damage mechanisms discussed in section 5.3 at different timescales, an experimental road map was developed and followed. The degradation of the polyimide insulation when exposed to high temperature has been studied at two timescales: hours heating in a furnace and millisecond heating due to the impact of a proton beam at room temperature. The effects of heating on Nb-Ti and Nb₃Sn superconducting strands were studied in the second timescale by means of capacitive discharges and in the millisecond timescale by irradiation with high intensity proton beam pulses at room temperature. In this chapter the experimental samples and set-ups are described. The results are discussed in chapter 7 and chapter 8.

6.1 Experimental samples

6.1.1 Insulated Rutherford cable stacks

To study the degradation of the polyimide insulation due to exposure to high temperature, compressed stacks of superconducting Nb-Ti LHC main dipole cables with a length a 240 mm were used. The cables were alternately stacked to compensate for the keystone angle, forming a rectangular stack as shown in Fig. 6.1. Out of the 240 mm, 100 mm of the cable stacks were compressed in a stainless steel mould, with a pressure of about 80 MPa, which is comparable to the maximum pressure experienced in a LHC dipole during nominal powering. Pictures of the mould used for the furnace experiment with and without cable stack are shown in Fig. 6.2. The mould is an assembly of several parts with a cavity to host the cable stack. In order to measure the pressure on the stack, the bar below the stack is equipped with strain gauges (not visible on the picture). The furnace experiment was performed with stacks of six LHC dipole inner

6. EXPERIMENTAL ROAD MAP

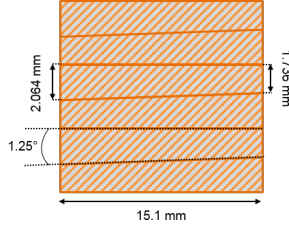


Figure 6.1: Schematic drawing of the cross section of a stack made of six LHC dipole inner layer cables. The cables are 15.1 mm wide and have a keystone angle of about 1.25° .

layer cables and the beam experiment with stacks of thirty dipole outer layer cables. The insulation of the two types of cable is the same, thus results of both experiment are fully comparable.

The moulds were manufactured in stainless steel (304L). Technical drawings can be found in Appendix A. The design of moulds used for both experiments differs only by the height of the cavity hosting the cables stack. The height of the cavity was derived from measurements of the cable stack height as function of the applied pressure. Fig. 6.3 shows these measurements for the inner layer cable. At 80 MPa during the loading phase the height of the six cables stack is about 13.3 mm. Similar measurements performed with outer layer cables can be found in [107]. The mould cavity heights were set to 12 mm for the furnace experiment and to 51 mm for the beam experiment.

The pressure on the cable stacks was applied via with eight bolts arranged in two parallel lines and measured via five pairs of mechanically independent strain gauges placed evenly along the length of the bar below the stack. The strain gauges were glued on each side of the five fingers of the bar as shown in Fig. 6.4. A calibration of the pressure applied on the cable stack as function of the torque of bolts was performed for each mould. The applied torque was the same for the eight bolts. Once the calibrations were performed, the instrumented bar was replaced by a similar bar without strain gauge. In Fig. 6.5, examples of calibration curves for two moulds used in the furnace experiment are shown. The pressure measured at the five fingers is plotted as a function of the applied torque on the bolts. The height of each finger is not exactly the same, thus the pressure finger to finger is expected to vary. The mechanical tolerance on the finger height was set to $50 \mu\text{m}$. From the linear part of the loading curve Fig. 6.3, one can see that $50 \mu\text{m}$ difference in height is equivalent to 10 MPa difference in pressure which is about the maximum difference of pressure between the fingers for a determined torque. Similar curves have been obtained for all the moulds, leading to the conclusion that an average pressure of 80 ± 10 MPa can be achieved by applying 60 Nm to each of the eight bolts.

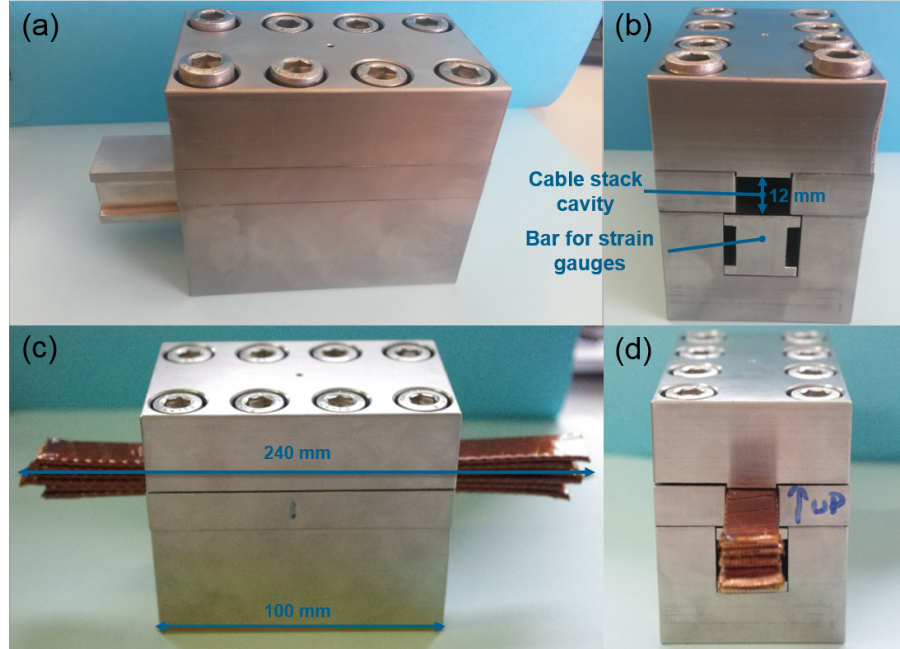


Figure 6.2: Stainless steel mould used in the furnace experiment without (a-b) and with (c-d) stack of six LHC dipole inner layer cables compressed with 80 MPa. The cavity for the cable stack with height of 12 mm and the bar for the installation of the strain gauges are visible in (b).

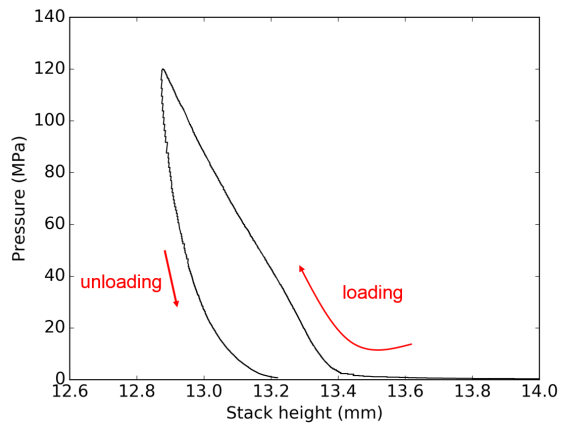


Figure 6.3: Height of a stack of six insulated LHC dipole inner layer cables as function of the applied pressure using a hydraulic press. During the loading, the stack height decreases linearly with pressure from ~ 5 MPa. After unloading the cable stacks does not come back to its initially height immediately.

6. EXPERIMENTAL ROAD MAP

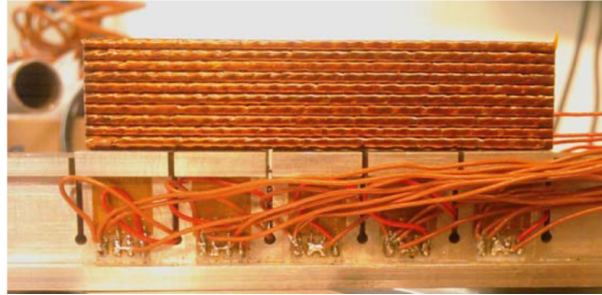


Figure 6.4: Side view of the bar placed below the cable stack instrumented with strain gauges to measure the pressure applied on the cable stacks. The five pairs of strain gauges are glued on each side of the five fingers.

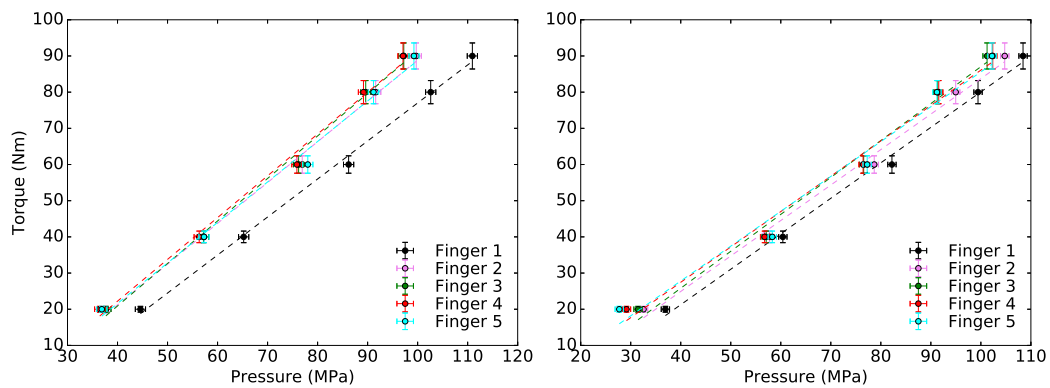


Figure 6.5: Torque of the bolts vs. pressure applied on the cable stack measured at five different locations along the stack obtained for two moulds (left and right). The spread in measured pressure between the fingers can be explained by the mechanical tolerance on the height of the finger ($50 \mu\text{m}$). An average pressure of 80 ± 10 MPa can be achieved by applying a 60 Nm torque. Linear fits for each finger are shown in dashed curves.

6.2 Measurements of insulation degradation due to heating during several hours

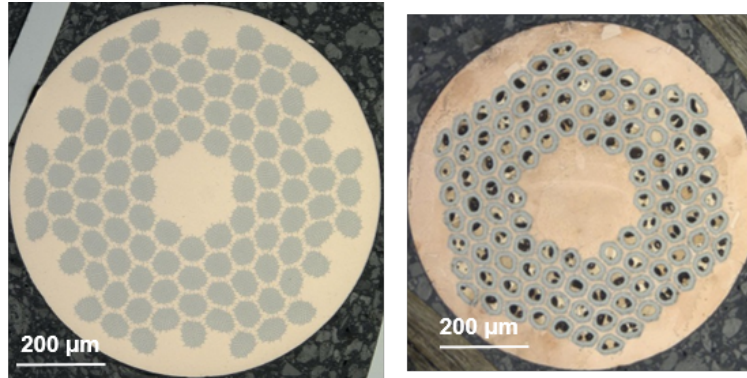


Figure 6.6: Cross section of a LHC main dipole inner coil Nb-Ti strand with a diameter of 1.065 mm (left) and of a RRP Nb₃Sn strand with a diameter of 0.85 mm designed for the future HL-LHC triplet and 11 T dipole magnets (right).

6.1.2 Superconducting Nb-Ti and Nb₃Sn strands

Multi-filamentary Nb-Ti and Nb₃Sn strands were used to study the degradation of critical current induced by heat and in a limited way by mechanical stress, deformation and cracks:

- The Nb-Ti strands from the LHC main dipole inner coil cables have a diameter of 1.065 mm and a filament diameter d_f of 7 μm . The copper to superconductor ratio α is 1.65. The superconductor has a Ti content of 47% by weight.
- Two types of Restacked-Rod Process (RRP) Nb₃Sn strands were used with a diameter of 0.7 mm and 0.85 mm, and a filament diameter d_f of 41 μm and 55 μm . The copper to superconductor ratio α is 1.04 and 1.2 respectively.

Cross section of a Nb-Ti strand and a Nb₃Sn strand with a diameter of 0.85 mm are shown in Fig. 6.6.

6.2 Measurements of insulation degradation due to heating during several hours

The aim of this experiment was to measure the insulation degradation due to exposure to high temperature for several hours. Compressed stacks of six LHC dipole inner coil cables were heated in a furnace reaching peak temperatures of 461 K to 864 K. After each heat treatment, the cable to cable dielectric strength was measured by applying high voltage. The results are discussed in detail in chapter 7.

6. EXPERIMENTAL ROAD MAP



Figure 6.7: Furnace used for the heat treatment of the cable stack. Argon was flowing in the oven during the heat treatment. Two stacks could be treated at once.

The heat treatment was performed within an Argon atmosphere, i.e. oxygen-free as in the LHC superconducting magnets. A picture of the furnace is shown in Fig 6.7. The temperature ramp rate was set to 150 K h^{-1} , with a flat top of 5 minutes. Each heat treatment was performed on two identical cable stacks. The temperature profiles of the cable stacks were measured and recorded with temperature sensors inserted through a 2 mm diameter hole on the top of the moulds to allow contact with the cable stacks. All the temperature profiles are compiled in Fig. 6.8, a fast temperature drop at the end of several curves is visible due to the opening of the furnace door to accelerate the cooling. For the heat treatment at $T_{peak}=461 \text{ K}$, the temperature recording was interrupted during the cooling due to a malfunction of the temperature acquisition system. The cooling time constant $t_{1/2}$ defined as the time when the sample was cooled to half the peak temperature is estimated to about 7 hours.

In addition to the moulds, polyimide tape samples with a thickness of 50 and $125 \mu\text{m}$ were heated in the furnace to determine their mass loss during the heat treatment. Each heat treatment was performed on ten tape samples, five of each thickness. The mass of the samples were measured before and after heat treatment with an hydrostatic balance. The resolution of the balance was 0.1 mg.

Dielectric strength measurements were performed cable to cable after each heat treatment. A schematic of the set-up is shown in Fig. 6.9 with the power supply, the voltage and current acquisition system and the cable stack. The insulation of the cable was removed for a length of about 1 cm at the cable extremities to allow to apply the voltages. To prevent breakdown between the non-insulated cable extremities, extra insulation sheets were used. To reduce the probability of a breakdown between the mould and the cables two u-shaped $125 \mu\text{m}$ thick polyimide sheets were introduced between the stacks and the mould. The power supply was limited to 20 kV and a

6.2 Measurements of insulation degradation due to heating during several hours

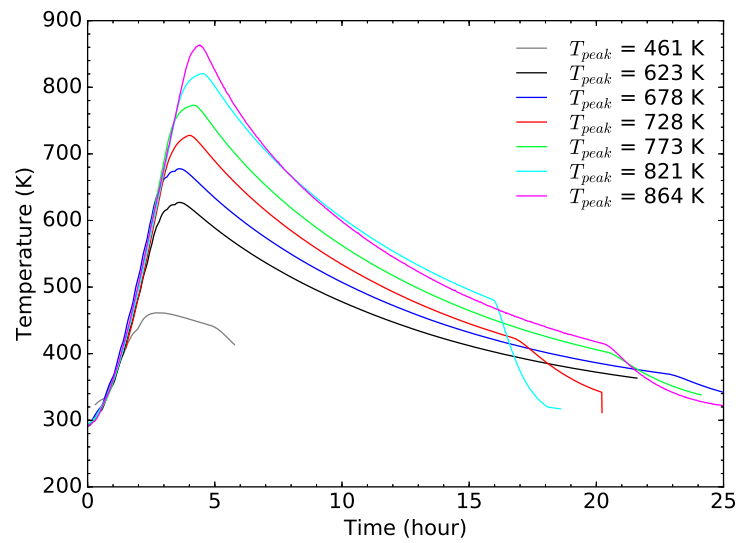


Figure 6.8: Temperature profiles of the cable stacks during the heat treatment. The drop at the end of several curves (cyan, red, pink, green and blue) is due to the opening of the furnace door to accelerate the cooling when temperature was below 500 K. Due to a malfunction of the temperature acquisition, the end of the cooling of the heat treatment reaching $T_{peak}=461$ K (brown curve) was not recorded. The cooling time constant $t_{1/2}$ defined as the time when the sample was cooled to half the peak temperature is estimated to about 7 hours (except for the brown curve).

6. EXPERIMENTAL ROAD MAP

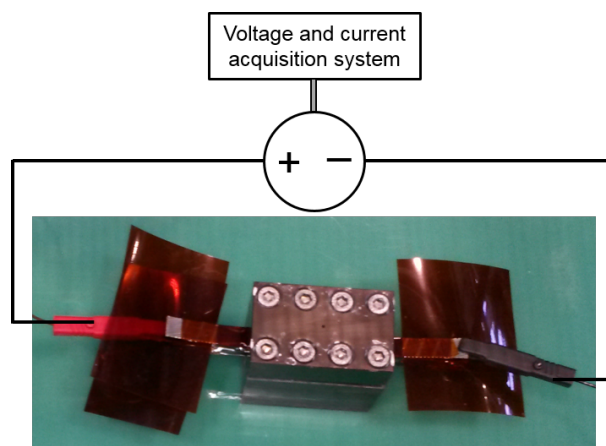


Figure 6.9: Schematic of the set-up to measure the dielectric strength cable to cable. In the present picture, the measurement was done between the two upper cables. Voltage and current outputs of the power supply were monitored. The insulation of cable extremities were removed to connect the cable and in order to prevent breakdown between the non-insulated cable extremities, extra insulated sheet were inserted.

maximum current of about 3 mA. For each peak temperature, six measurements were performed - three per stack. The mould and the non measured cables were kept floating. An example of such a measurement is show in Fig. 6.10 with the voltage in blue and the current in red. The voltage is risen until 19 kV when the breakdown happened, the voltage goes to zero and current to its maximum.

6.3 Measurements of superconductor degradation due to heating over seconds

To study the degradation of the critical current density of Nb-Ti and Nb₃Sn superconductors due to heating over second, strands were heated up by means of a capacitive discharge. The critical current density was then measured via magnetization measurement and change of the microscopic structure of the strand were observed with optical and electron microscopy. The results are discussed in detail in chapter 8.

6.3.1 Capacitive discharge set-up

Superconducting Nb-Ti and Nb₃Sn strands with a length of 8 cm were heated up in air from room temperature to peak temperatures ranging from 649 K to 1264 K within a few millisecond using capacitive discharges. The schematic and a picture of the

6.3 Measurements of superconductor degradation due to heating over seconds

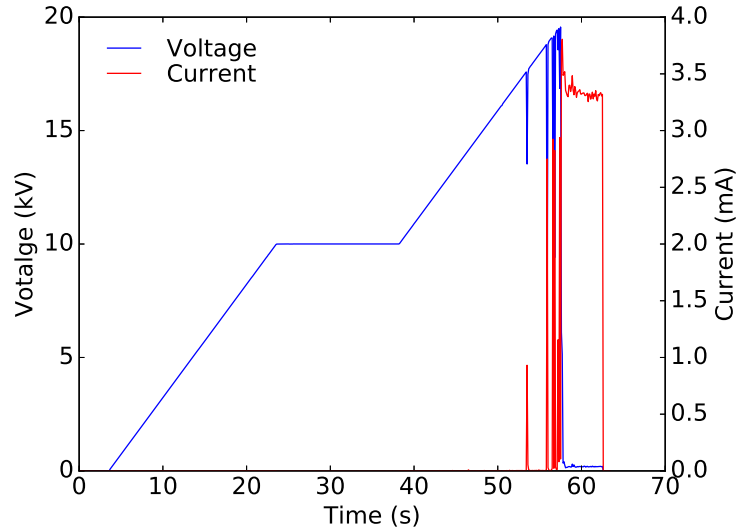


Figure 6.10: Power supply voltage and current output recorded during a dielectric strength measurement cable to cable. Breakdown happened at about 19 kV when the voltage goes to zero and current to its maximum.

experimental set-up are shown in Fig. 6.11 and Fig. 6.12. The capacitor bank made of several capacitors with a total capacitance of 80 mF and a maximum voltage of 500 V was discharged into the strand in series with a 35 m Ω resistor. The energy deposition in the strand and the peak temperature depend on the charging voltage of the capacitors. The peak temperature was reached after ~ 11 ms. The superconducting strand with a resistance of about 3 m Ω at room temperature was clamped at its extremities between copper plates fixed on a fibre glass plate. A protective cover was placed above the heated set-up to stop possible hot debris. The 35 m Ω resistor was used to limit the current in the circuit. The current was measured with a current transformer [108]. The current and the voltage drop over the strand during the discharge were recorded with a Tektronix DPO 5054 oscilloscope. The signals were recorded at 500 kHz and reduced to 10 kHz by an averaging filter to increase signal-to-noise ratio. An example of a current discharge is shown in the pictures Fig. 6.13. At $t=0$ s a Nb-Ti strand clamped between the copper plates with the cables coming for the capacitor bank (red and blue) and the two voltage probes (red and black) are visible. A peak temperature of 1157 K is reached in the strand after 11 ms, the entire strand is glowing. 2 s after the discharge, the extremities of the strand have already significantly cooled down, i.e. not glowing any more. After 4 s, only the central part of the strand is still glowing.

The peak temperatures of the strands were derived from the measured voltage drop

6. EXPERIMENTAL ROAD MAP

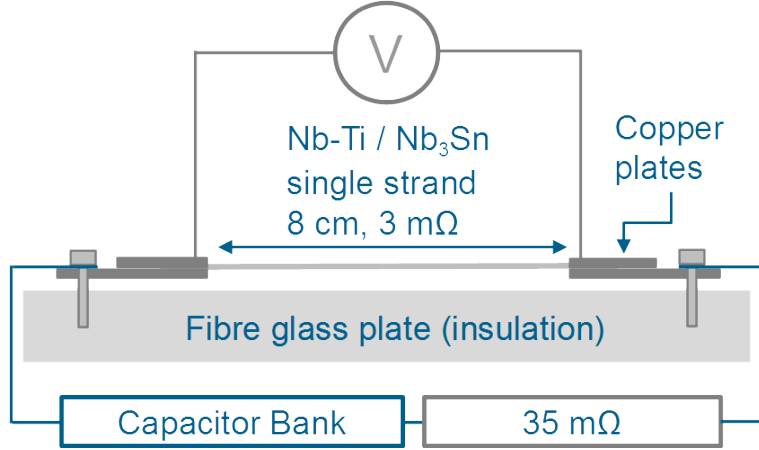


Figure 6.11: Sketch of the set-up for the capacitive discharge experiment. The 80 mF capacitor bank was discharged into the Nb-Ti or Nb₃Sn 8 cm long strand in series with a 35 mΩ resistor. The strand is clamped at its extremities between copper plates fixed on a fibre glass plate. The current and voltage drop over the strand during the discharge were recorded.

over the strand, $U_d(t)$, the current in the strand, $I_d(t)$, and with the temperature dependent resistivity of the copper ρ_{Cu} . The resistance of a single strand is dominated by the resistivity of the copper. The resistivity of Nb-Ti and Nb₃Sn in normal conducting state is more than one order of magnitude higher than the one of copper [75] and therefore can be neglected. Thus the strand resistivity $\rho_s(t)$ can be expressed as the following,

$$\rho_s(t) = \rho_{Cu}(t) = \frac{U_d(t)}{I_d(t)} \frac{\sigma_s \alpha}{l_s(1 + \alpha)} \quad (6.1)$$

where σ_s , l_s and α are the cross section, the length and the copper to superconductor ratio of a strand. The temperature is then deduced from the temperature dependence of the copper resistivity as shown in the equation 6.2 [109]:

$$\rho_{Cu}(T) = 10^{-8}(3.239 \times 10^{-1} + 6.955 \times 10^{-3}T - 7.594 \times 10^{-7}T^2 + 9.749 \times 10^{-10}T^3), \quad (6.2)$$

where T is the temperature in K. In the same way the temperature error bar was derived from the resistivity uncertainty which was calculated as following:

$$\frac{\Delta \rho_s}{\rho_s} = \frac{1}{2} \left(\frac{\Delta U_{dpp}}{U_d} + \frac{\Delta I_{dpp}}{I_d} \right) \quad (6.3)$$

where ΔU_{dpp} and ΔI_{dpp} are the measured peak to peak noise level on the 10 kHz signals.

The measured currents and voltages and the resulting strand temperatures are shown for the lowest and highest peak temperatures reached in Nb-Ti strands in

6.3 Measurements of superconductor degradation due to heating over seconds

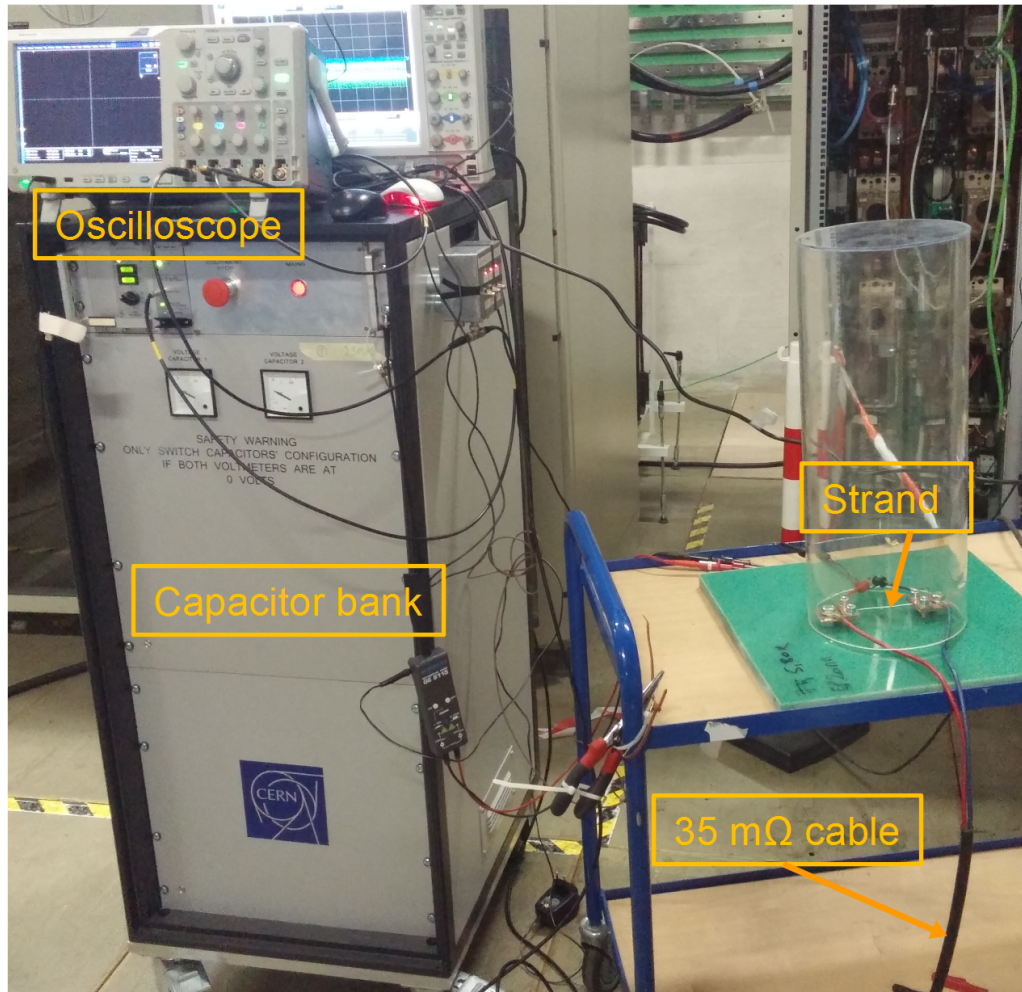


Figure 6.12: Picture of the experimental set-up with the capacitor bank connected to the strand via a 35 mΩ cable. The voltage and current were recorded with an oscilloscope. A protective covered was placed above the heated set-up to stop possible hot debris.

6. EXPERIMENTAL ROAD MAP

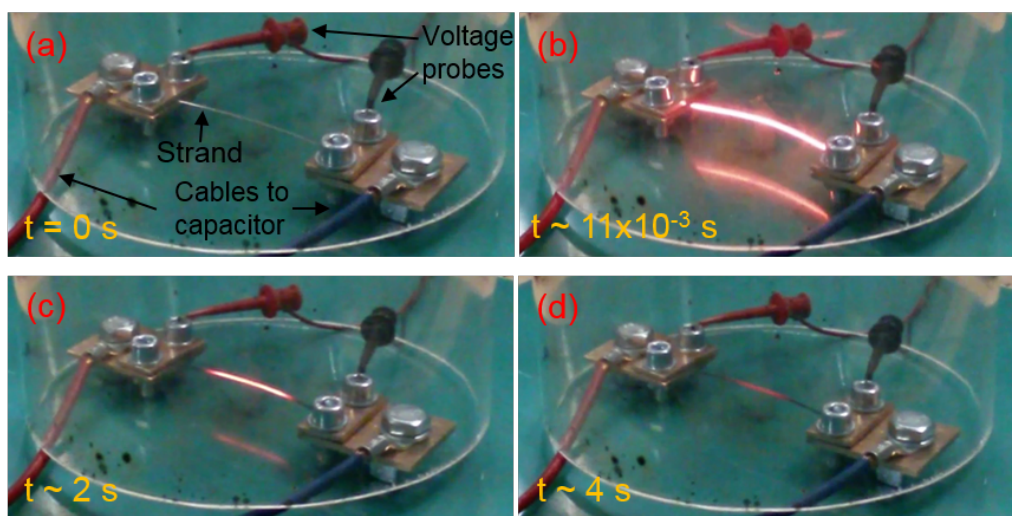


Figure 6.13: (a) Nb-Ti strand before the discharge, clamped between the copper plates with the cables coming for the capacitor bank (red and blue) and the two voltage probes (red and black). (b) Same as (a) but 11 ms after the start of the discharge when the peak temperature is reached (1157 K). The entire strand is glowing. (c & d) Same as (b) but during the cooling of the strand in air 2 s and 4 s after the discharge. The heat is mostly evacuated by heat conduction through the strand in the copper plates.

Fig. 6.14 and for Nb_3Sn strand in Fig. 6.15. The maximum temperatures were reached within 11 ms after the start of the discharge. To achieve temperatures of 649 K and 1068 K in a Nb-Ti strands, the capacitor was loaded to 170 V and 225 V and the peak currents during the discharge were about 3 kA and 4 kA. As Nb_3Sn have a smaller diameter than Nb-Ti strands, lower currents were needed to heat them up. To reach 1264 K, the capacitor bank was charged to 155 V and the peak current was less than 2 kA.

The cooling of the strands after the discharge was simulated in ANSYS. The main cooling mechanism was identified to be the heat conduction along the strand. The copper plates were considered as a infinitely big heat sink at room temperature. The temperature at different positions along the strand as function of time is shown in Fig. 6.16. The curves of the temperature at the strand centre (0 mm) and 2 mm away from the strand centre are overlapping, with a largest difference below 2 K. Therefore the temperature along the central 4 mm of the strand is considered to be homogeneous with a maximum thermal gradient below 1 K mm^{-1} . The cooling constant $t_{1/2}$ of the central part of the strand is estimated to ~ 6 s.

6.3 Measurements of superconductor degradation due to heating over seconds

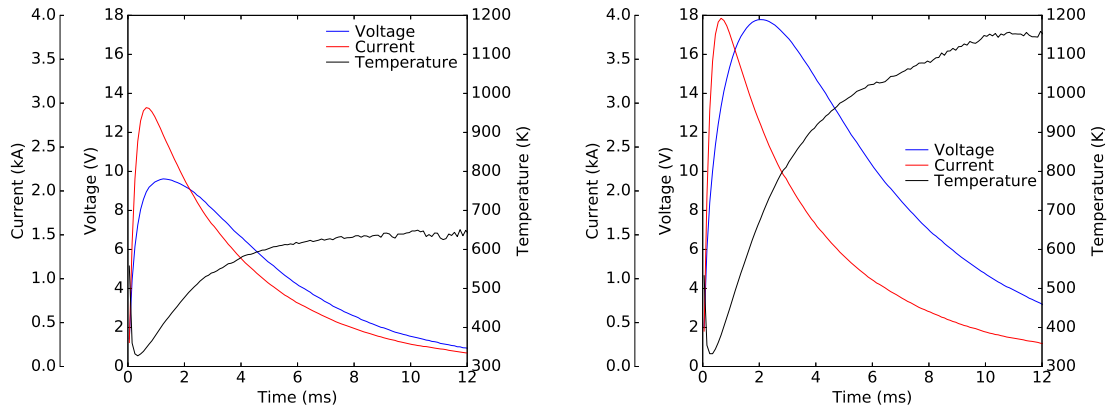


Figure 6.14: Measured current (red) and voltage drop (blue) over a Nb-Ti strand during the discharge with the capacitor bank initially charged to ~ 170 V (left) and ~ 225 V (right), leading to a heating of the strand to 649 ± 20 K (left in black) and 1068 ± 18 K (right in black).

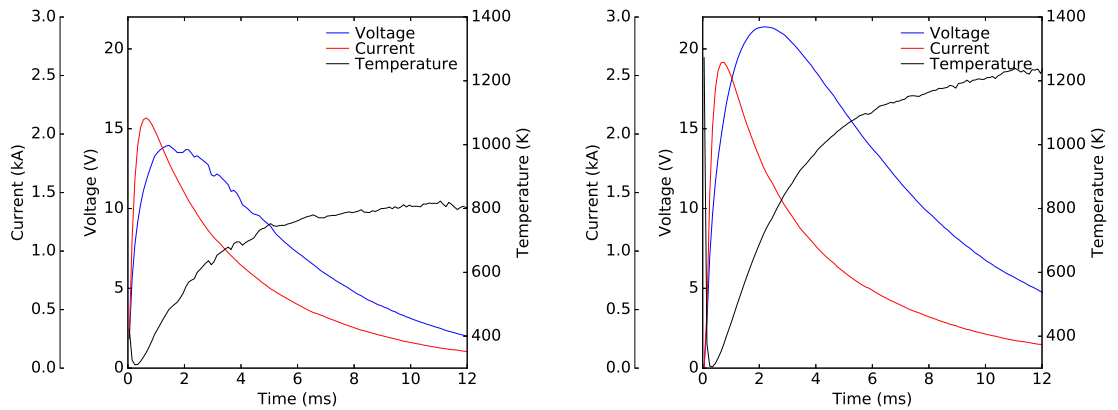


Figure 6.15: Measured current (red) and voltage drop (blue) over a Nb₃Sn strand during the discharge with the capacitor bank initially charged to ~ 130 V (left) and ~ 155 V (right), leading to a heating of the strand to 823 ± 18 K (left in black) and 1264 ± 20 K (right in black).

6. EXPERIMENTAL ROAD MAP

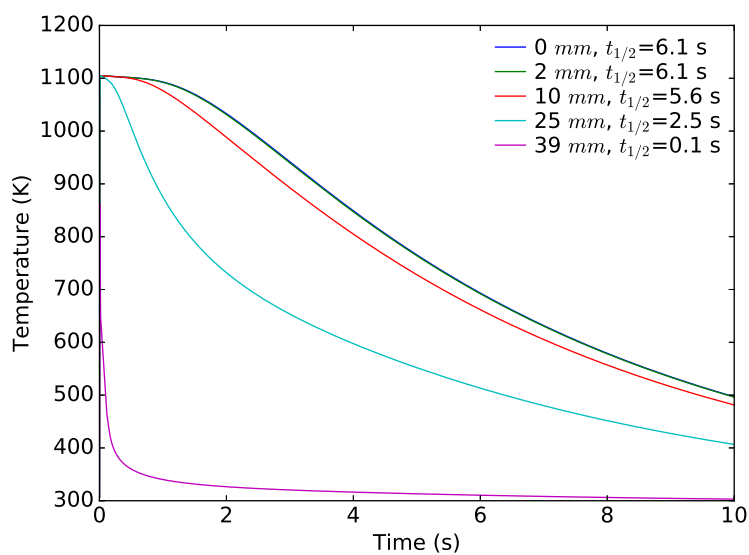


Figure 6.16: Temperature at different longitudinal position of the strand as a function of time since the peak temperature was reached, as obtained from ANSYS simulation. The positions along the strand are referring to its centre, 0 mm being the strand's centre (blue) and 39 mm (violet) being 1 mm away from the copper plates. The 2 mm curve is overlapping with the 0 mm curve, the largest difference between the two curves is below 2 K. The cooling time constant $t_{1/2}$ of the central 4 mm of the strand was derived as ~ 6 s.

6.3 Measurements of superconductor degradation due to heating over seconds

6.3.2 Magnetization measurements

The degradation of the critical current was measured via magnetization measurements. Magnetization measurements were chosen in order to simplify the experimental set-up and the sample preparation (especially for the activated sample in the beam experiments). Furthermore, it has been shown that magnetization measurements and direct critical current measurements provide very similar critical current values for Nb-Ti [73] and Nb₃Sn strands [74]. The magnetization measurements were performed on the strands central parts of 4 mm length, where the temperature profile was assumed to be homogeneous. The 4 mm long central part of the strands were extracted from the 8 cm long strand. First the strands were cut using a wire cutter to keep only the central part of ~ 5 mm length. Then about 0.5 mm on both extremities of the central parts were polished away in order to removed any possible damage induced by the cutting.

The magnetization measurements were performed at the University of Geneva using a Superconducting Quantum Interference Device Vibrating Sample Magnetometer (SQUID VSM). In such device, the sample is placed within sensing coils which are coupled to a SQUID via a superconducting flux transformer. An external magnetic field H_{\perp} is applied to the sample such that a magnetic moment m is induced in the sample. The sample vibrates inducing a variation of the magnetic flux through the sensing coils. The flux change results in an output voltage generated by the SQUID which is proportional to the magnetic moment m of the sample. The magnetization M expressed in T is derived from the magnetic moment m of the sample expressed in A m² kg⁻¹ with the following equation:

$$M = m \times \rho \times \mu_0 \times 10^{-3}, \quad (6.4)$$

where ρ is the density of the sample in kg m⁻³ and μ_0 is the vacuum permeability.

The measurements were performed under an applied field H_{\perp} perpendicular to the strand axis reaching a maximum of 7 T with a sweep rate of 0.3 T min⁻¹ and at temperatures of 2 K, 4 K and 6 K for Nb-Ti and 2 K, 4 K, 10 K and 15 K for Nb₃Sn.

6.3.3 Microscopic measurements

Changes in the structure, microstructure and chemical composition of the samples were observed via optical microscope and Scanning Electron Microscope (SEM). Two types of analysis were performed with the SEM either using the backscattered electron (BSE) or the energy dispersive X-ray spectrometry (EDX).

6. EXPERIMENTAL ROAD MAP

The BSE are electrons from the electron beam that are reflected or back-scattered out of the sample by inelastic scattering interaction. Heavy elements backscatter electron more strongly than light elements and appear brighter in the images. BSE provide qualitative information on the chemical composition of the different area of the sample.

The EDX analysis is based on the X-rays produced by the sample after its interaction with the electron beam. The electron beam may excite electrons from the inner shell of the atoms of the sample and eject them from the shell creating electron holes. Electrons from outer shell may fill the holes. During this transition from a higher-energy shell to a lower-energy shell, the energy can be released in the form of an X-ray. The flux and energy of the X-rays are characteristics of the atomic structure of the emitting element. EDX allows to measure the chemical composition of the sample expressed either in atomic percent (at.%) or in weight fraction (wt.%). For the measured samples, the accuracy of the EDX analysis is within 1 at.% with a resolution of $\sim 1 \mu\text{m}^3$.

6.4 Measurements of insulation and superconductor degradation due to beam impact

For the first time the effect of high intensity microsecond beam impact on superconducting magnet components has been measured. Stacks of insulated LHC dipole cable and single superconducting Nb-Ti and Nb₃Sn strands were exposed at room temperature within an inert Argon atmosphere to pulses of a 440 GeV c^{-1} proton beam in the HiRadMat facility at CERN. Temperatures inside the samples were rising up to 1026 K within 0.6 μ s. Following few weeks of radioactive cool-down the samples were removed and analysed.

6.4.1 HiRadMat - Facility

The High-Radiation to Materials (HiRadMat) facility at CERN was designed to provide high intensity beam pulses, extracted from the Super Proton Synchrotron (SPS) to an irradiation area where material samples can be tested [110, 111]. HiRadMat is not an irradiation facility where large doses on equipment can be accumulated but a test area to evaluate the effect of high-intensity beam pulses on material. Several experiments have already been performed on accelerator components such as collimators [56] and targets [112] to assess their damage limits and also on copper targets to evaluate the damage potential of LHC beam [49, 50].

HiRadMat is located in the TNC tunnel in the SPS BA7 area. The beam is delivered from the SPS using the TT60 and TT66 transfer lines. The experimental area covers the last 10 m of the TT66 line with three experimental tables in front of a beam dump. The beam is extracted with a particle momentum of 440 GeV c^{-1} and with intensities from $\sim 3 \times 10^9$ to $\sim 1.7 \times 10^{11}$ protons per bunch. A maximum of 288 nominal (i.e. total $\sim 4.89 \times 10^{13}$ protons) can be extracted. The bunch spacing is adjustable within 25, 50, 75 or 150 ns. The beam size at the experiment can be tuned from $1 \sigma_{r.m.s.} = 0.1$ mm to 2 mm [113]. To minimize the radiation dose taken by the personal for the installation and removal of experiments, the experimental set-ups are installed on a standardized support plate. It can be remotely manipulated with a crane and positioned with an accuracy of 0.1 mm. Services like electrical power and signal cables are delivered via plug-in connectors. Signal cables to the control room on the surface or to the adjacent tunnel TT61 where equipment can be installed are provided. Two feed-throughs between the experimental tunnel and the adjacent tunnel are available for cables, pipes and optical paths. Beam instrumentation is installed along the SPS ring and the transfer line to measure the beam parameters like the transverse beam position

6. EXPERIMENTAL ROAD MAP

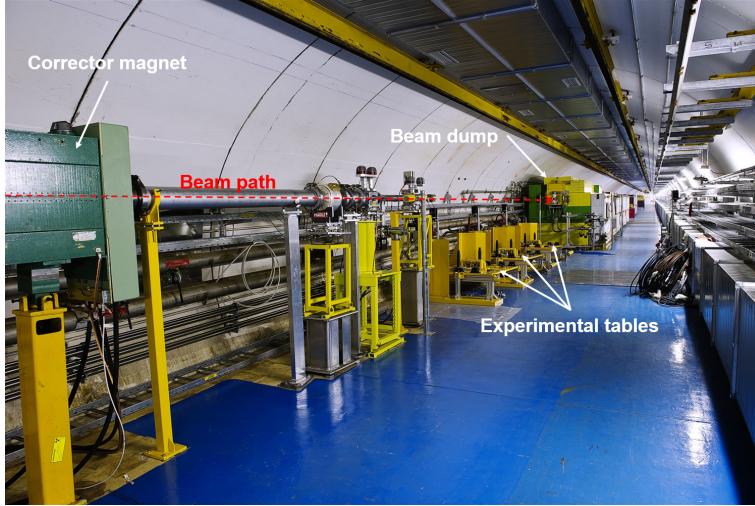


Figure 6.17: HiRadMat tunnel with the last corrector magnet (green), the platforms for the experimental table (yellow) and the beam dump (green and yellow) at the end of the tunnel.

with Beam Position Monitors (BPMs) and Screens (BTVs). The transverse beam emittances are measured in the SPS ring with vertical and horizontal wire scanners. The pulse intensity is measured by Beam Current Transformers (BCTs) in the transfer line and in the SPS ring. To monitor the transverse beam position at the experimental table, a screen can be installed in front of the HiRadMat support plate.

Fig. 6.17 shows a picture of the HiRadMat tunnel with the last corrector magnet (green) and the platforms for the experimental table. A schematic drawing of the HiRadMat tunnel area is shown in Fig. 6.18. The experimental tunnel is labelled TNC and the adjacent tunnel with the bunker for the electronic equipment of the users for data acquisition is TT61.

6.4.2 Description of experiment

Twelve compressed stacks of thirty insulated LHC dipole outer layer cables and thirty-four single superconducting Nb-Ti and Nb₃Sn strands were exposed at room temperature within an inert atmosphere to several 440 GeV proton beam pulses. A picture of one of the cable stacks in its steel mould is shown in Fig. 6.19. The strands were divided in two sets, clamped on insulated stainless steel plates as shown on Fig. 6.20. The strands were vertically positioned every 5.2 mm. For the six strands with the highest beam intensities additional strands 1.2 mm above and below were installed. The resistance of the strands were monitored during the irradiation to measure the peak

6.4 Measurements of insulation and superconductor degradation due to beam impact

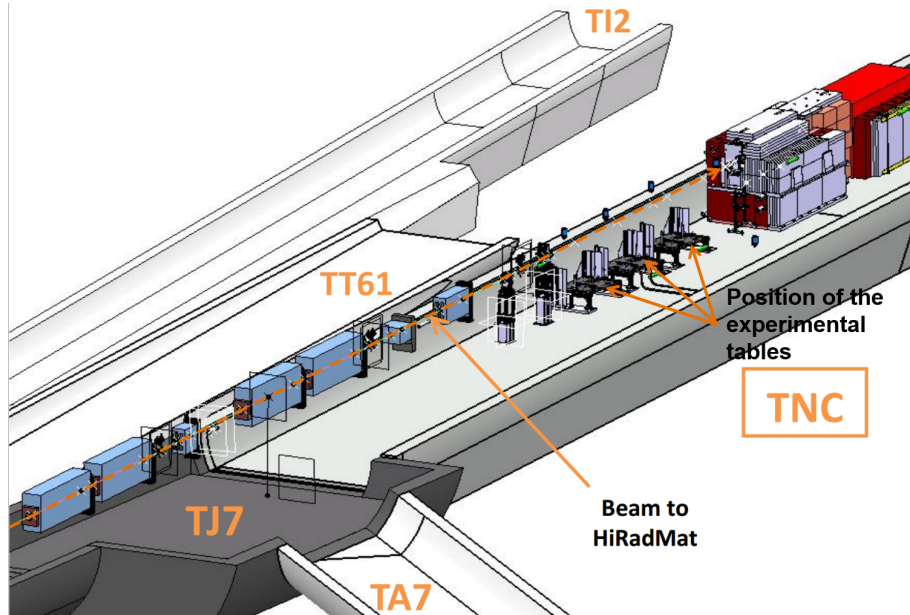


Figure 6.18: Schematics drawing of the HiRadMat tunnel area, entrance area (TJ7), experimental tunnel (TNC), adjacent tunnel (TT61) where the bunker for the user electronic equipments for data acquisition is located (not visible on the drawing).

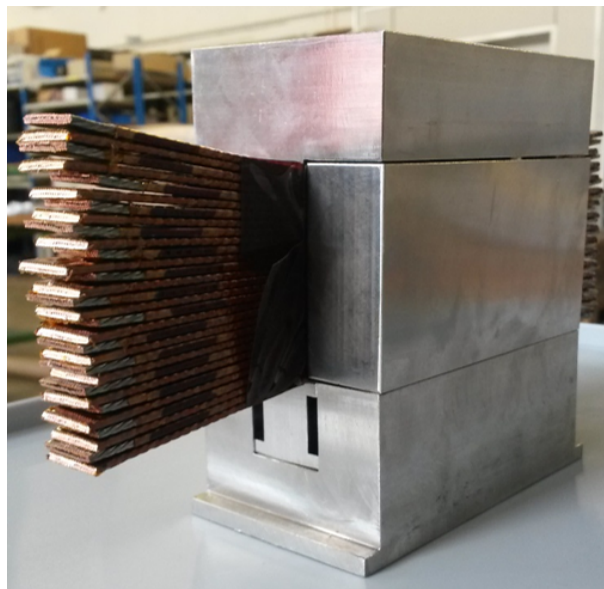


Figure 6.19: One of the stack of thirty insulated LHC dipole outer layer cables under a pressure of 80 MPa in a steel mould.

6. EXPERIMENTAL ROAD MAP

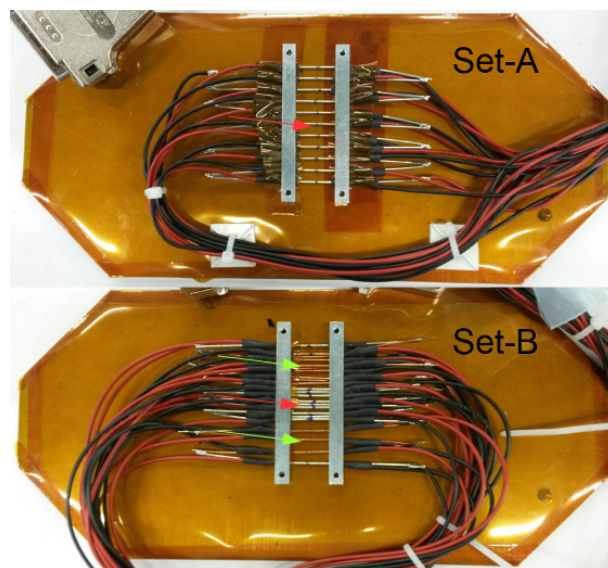


Figure 6.20: The two sets of strands (upper one set-A, lower one set-B) clamped on the insulated stainless steel plates. The Nb-Ti strands are the silvery looking ones (indicated by red arrows) and the Nb₃Sn are the coppery looking ones (indicated by green arrows). The cables to connect the strand in series and measured the voltage drop are visible.

temperatures. The samples were arranged in an air-tight tank on two levels with the strand sets inserted between the cable stacks (see Fig. 6.21). Eighteen pulses with three different intensities (six pulses per intensity) were shot onto the samples, as sketched by the dashed yellow arrows in Fig. 6.21. Between each pulse, the tank was moved vertically by 5.2 mm, such that each beam pulse would hit a virgin zone of the cable stacks and a new strand. For each pulse, the strand in the beam axis will be later on referred as the targeted strand. The list of the strands with their label, type and the beam intensity by which they were impacted is shown in Appendix B. Results of FLUKA energy deposition simulations (see Appendix C) were used to choose pulse intensities and beam size required to reach peak temperatures in the samples between 350 K and 1100 K. The chosen beam pulse intensities and the measured $1 \sigma_{r.m.s.}$ transverse beam size can be found in Table 6.1.

Tank design

An anticorrosive aluminium alloys (AW-6082 [114, 115]) was preferred to stainless steel as tank material for several reasons: its mechanical strength, its low density implying that the beam will deposit less energy in the tank walls and its chemical composition to reduce activation. To make sure that the samples were kept within an inert atmosphere

6.4 Measurements of insulation and superconductor degradation due to beam impact

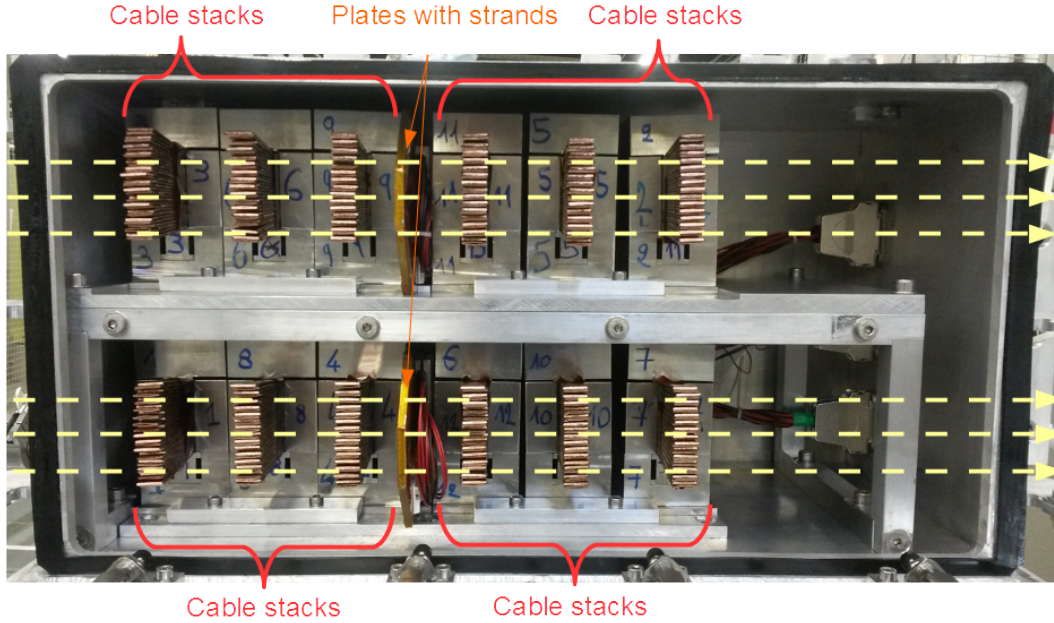


Figure 6.21: Open tank with the samples arranged on two levels. The twelve cable stacks and two plates with the superconducting strands are visible. The dashed yellow arrows indicate the trajectory of six sample beam pulses.

Table 6.1: Transverse beam size in $\sigma_{r.m.s.}$ measured for each pulse intensity used during the beam experiment

Intensity (protons)	σ_x (mm)	σ_y (mm)
6×10^{11}	1.23	1.13
1.3×10^{12}	1.07	0.99
2.6×10^{12}	1.17	1.11

6. EXPERIMENTAL ROAD MAP

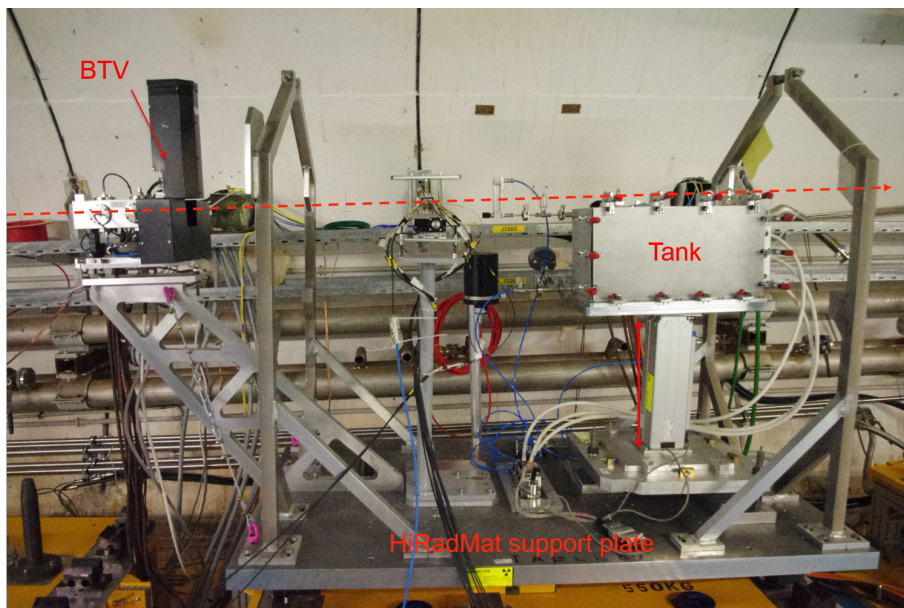


Figure 6.22: Experimental set-up on the HiRadMat support plate installed in the experimental area. The tank with the samples mounted on the moveable table is in out-of-beam position. The screen and camera (BTV) used to measure the transverse beam position are in the black boxes. The red dashed arrow indicates the beam path.

during the experiment, a constant flow of Argon gas of about 5 l h^{-1} was circulating through the tank. The Argon was provided by a pressurized bottle located in the adjacent tunnel and its flow was measured with a flow-meter positioned at the tank gas inlet. To prevent any contamination of the experimental area with radioactive dust, a high efficiency particulate air (HEPA) filter [116] was placed at the tank gas outlet. Three electrical feed-throughs were mounted on the back of the tank hosting the instrumentation cable for the resistance measurements. The closed tank was mounted onto a vertically movable table and the overall set-up was installed on the standardized HiRadMat lifting support plate as shown in Fig. 6.22.

Set-up of strand resistance measurement

A sketch of the set-up of the strand resistance measurement for one of the two sets of strands is shown in Fig. 6.23. The strands of each set were connected in series with a shunt precision resistor and with an dual power supply delivering a constant current of 1 A. Voltages across about 3 cm of each strand were recorded with a multifunction data acquisition (DAQ) at a frequency of 2 kHz. The voltage drop across the shunt precision resistor was also recorded in order to monitor the current delivered by the power supply.

6.4 Measurements of insulation and superconductor degradation due to beam impact

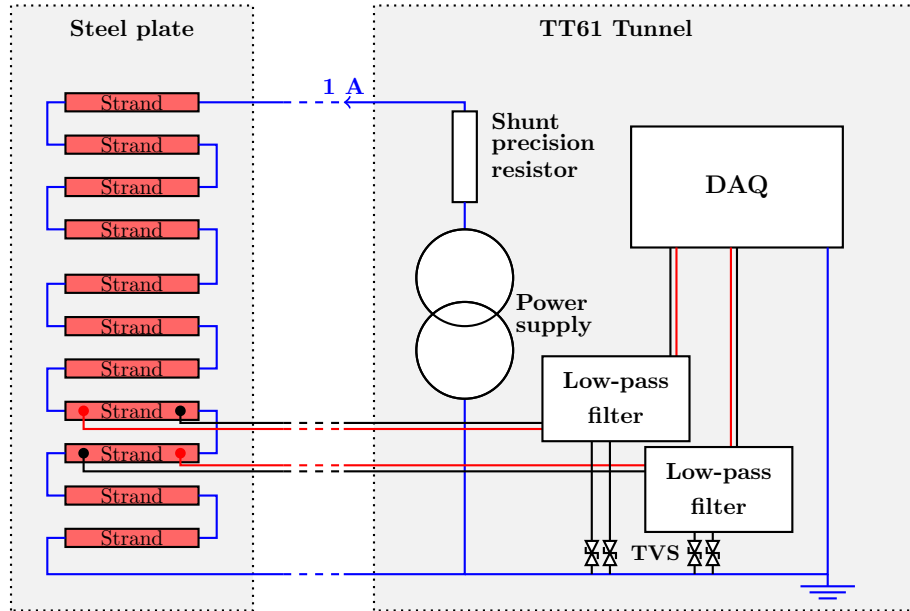


Figure 6.23: Sketch of the set-up of the strands resistance measurement. Only one set with strands is shown. On the present strand set, every strand was equipped with voltage tabs to measure the voltage drop over the strand, however to simplify the sketch they are only shown for two cases. For the other strand set, the six strands with the highest intensities are not equipped with voltage tabs but the strands 1.2 mm above and below are.

The resistance of the strand was then deduced from the voltage across the strand and the current in the circuit. Each voltage channel was equipped with a passive low-pass filter to reduce the noise level and with two Transient Voltage Suppressor diodes (TVS) to protect the DAQ from possible voltage spikes induced by the beam. To be protected from radiation, all the acquisition equipment was located in a bunker adjacent to the experimental area.

6.4.3 Temperature rise and cooling profile

Temperature rise

The peak temperatures reached in the samples were derived from strand resistance measurements and numerical energy deposition simulations done with FLUKA (see Appendix C).

For each beam pulse, the voltage drop over the strands and over the shunt precision resistor was measured. An example of such a measurement during the impact of

6. EXPERIMENTAL ROAD MAP

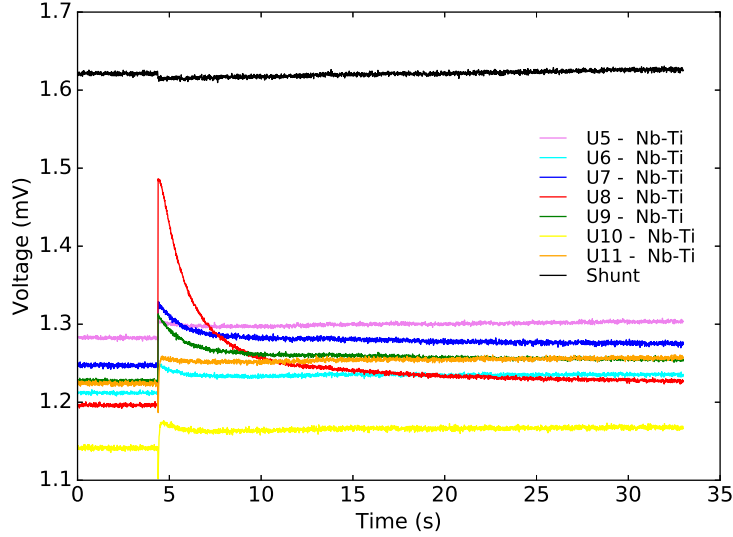


Figure 6.24: Voltage drop measured over about 3 cm of the strands and over the shunt precision resistor before and after the impact of 1.3×10^{12} protons beam pulse. The beam impacted the strands at ~ 5 s. The targeted Nb-Ti strand U8 (red) shows the highest voltage rise (0.29 mV) thus the highest temperature rise. The further the strands are from the targeted strand, the lower their voltage rise is. After the beam impact, the voltage drop over the strands decreases as the strands cool down. The noise level peak to peak is below $5 \mu\text{V}$ on all the channels.

1.3×10^{12} protons on the strand U8 (red) is shown in Fig. 6.24. The voltage rise was the highest in strand U8 and smaller rises could be observed for the neighbouring strands up to several millimetres from the beam axis. After the beam impact, all the voltages were decreasing as the strands were cooling down. From the voltage measurements, the relative resistance variation of each strand $\frac{\Delta R}{R_i}$ was calculated with the following equation:

$$\frac{\Delta R}{R_i} = \frac{U_f}{U_i} \cdot \frac{U_{i_{m\Omega}}}{U_{f_{m\Omega}}} - 1 \quad (6.5)$$

where U_i and $U_{i_{m\Omega}}$ are the voltage drop over the strand and the shunt precision resistor before the beam impact and U_f and $U_{f_{m\Omega}}$ are the voltage drop at the time of the beam impact. Thus for each pulse, the relative resistance variation of the strands versus their vertical position y_s was obtained. An example of such result is given in Fig. 6.25 derived from the voltages measured in Fig. 6.24, where y_s is referred to the targeted strand (U8 $y_s = 0$ mm).

The relative resistance variation of a strand is proportional to the average temperature rise along the strand. To determine the peak temperature in the strands from such

6.4 Measurements of insulation and superconductor degradation due to beam impact

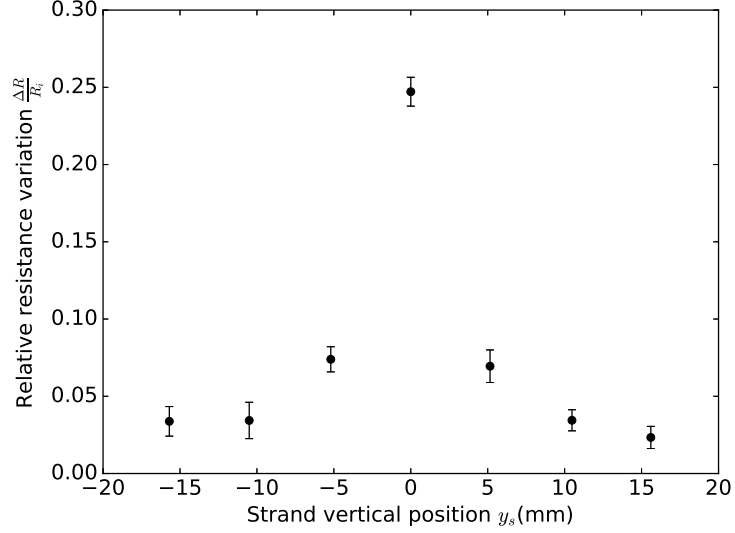


Figure 6.25: Strands relative resistance variation induced by the beam with 1.3×10^{12} protons as function of their vertical position y_s with reference to the targeted strand. The relative resistance variation were calculated from the voltages measured in Fig 6.24 using equation 6.5.

measurements two assumptions had to be made. First, based on the FLUKA simulation the energy deposition along the strands $E(x_s, y_s)$ was found to be well described by the Cauchy-Lorentz distribution:

$$E(x_s, y_s) = \frac{K}{\pi\gamma} \frac{\gamma^2}{((x_s - x_0)^2 + (y_s - y_0)^2 + \gamma^2)}, \quad (6.6)$$

where y_s is the vertical position of the strand, x_s is the horizontal position along the strand, (x_0, y_0) is the beam position in the transverse plane, γ is the half-width at half-maximum and $\frac{K}{\pi\gamma}$ is the maximum energy density located at $x_s = x_0$ and $y_s = y_0$. In Fig. 6.26, the energy deposited per proton along three strands with different vertical positions y_s as obtained by FLUKA is compared to the one obtained by fitting equation 6.6. The obtained fitting parameters K , γ and $y_0=0$ mm can be found on the figure. The second assumption was to consider that the beams were round in the transverse planes. In the experiment, the beam is maximum 8% larger in the horizontal axis. According to the FLUKA simulations, this assumption leads to an overestimation of 5% of the strand peak temperature.

A relation exists between the profile of the energy deposited in a strand and its relative resistance variation $\frac{\Delta R}{R_i}$ (see Appendix D). Thus for each beam pulse, a unique set of K , γ and y_0 can be found such that the $\frac{\Delta R}{R_i}$ of several strands calculated based on

6. EXPERIMENTAL ROAD MAP

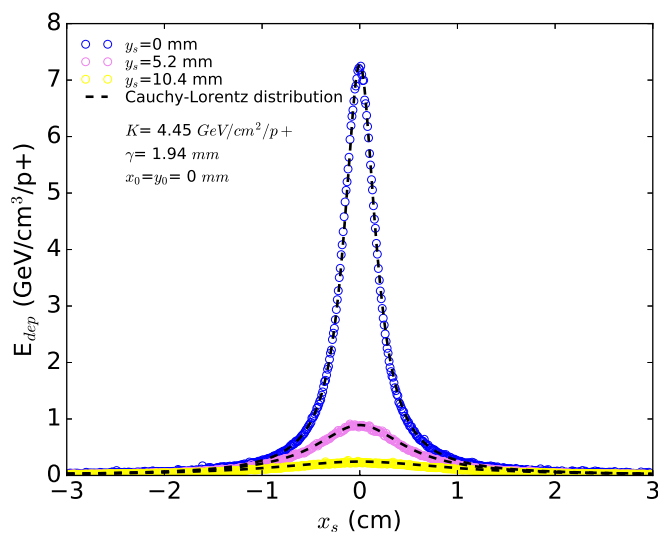


Figure 6.26: Comparison of the horizontal energy deposition per proton profile of three strands with different vertical positions y_s (0 mm, 5.2 mm, 10.4 mm) relative to the beam axis, induced by a beam with a $1 \sigma_{r.m.s.}$ transverse size of 1 mm obtained by FLUKA simulation (round markers) and by the fitting of a Cauchy-Lorentz distribution (dashed lines). The fitted parameters K , γ and y_0 of the Cauchy-Lorentz distribution given in the plot were found to describe well ($R^2=99.9\%$) the energy deposition as obtained by FLUKA in all three strands.

6.4 Measurements of insulation and superconductor degradation due to beam impact

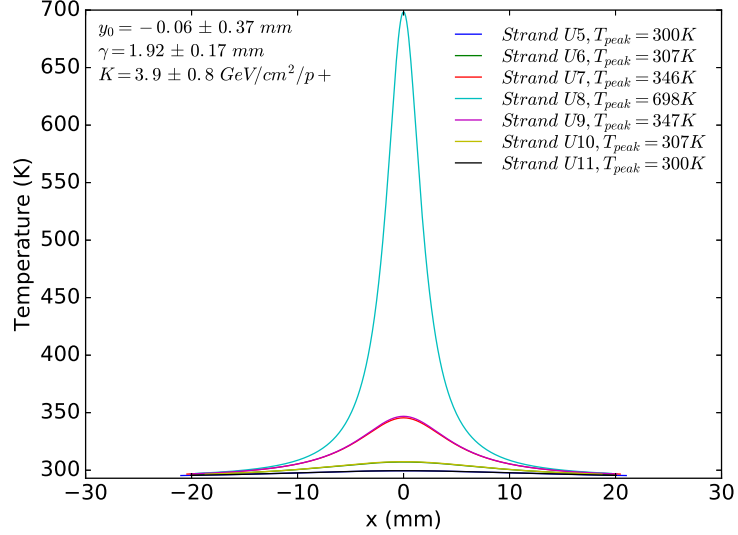


Figure 6.27: Temperature profile of several strands after the impact of 1.3×10^{12} protons. The profile were obtained from the relative resistance variation measurements shown in Fig. 6.25. The peak temperature for each strand is given, with the highest temperature of 698.5 K for strand U8 (cyan). The fitted parameters of the Cauchy-Lorentz distribution are shown with their uncertainties.

the Cauchy-Lorentz distribution describing the energy deposition in the strands $E(x, y)$, matched the measured $\frac{\Delta R}{R_i}$. The strand temperature profile and peak temperatures were then calculated from the energy deposition profile via their heat capacity. An example of the obtained strand temperature profiles after the impact of 1.3×10^{12} protons (same beam pulse as for Fig 6.25) is shown in Fig 6.27. The peak temperature reached in the targeted strand (U8 in cyan) is about 698 K and is below 350 K in its six closest neighbouring strands (U5 to U11). The fitted parameters K , γ and y_0 with their respective uncertainties are shown in the figure. The temperature along each strand is not homogeneous and the thermal gradient within the few millimeters surrounding the beam impact was estimated to 80 K mm^{-1} . In other words, if the strand hot spot temperature is about 700 K, the temperature 2 mm away from the hot spot is expected to be about 540 K.

The uncertainties on the strand peak temperature were derived from the uncertainties on the fitting parameters K , γ and y_0 . The upper bound of the peak temperature was obtained from the energy deposition profile using the upper bound of K , the lower bound of γ and the closest value of y_0 to zero. The lower bound was obtained using the lower bound of K , the upper bound of γ and the y_0 with the largest absolute value,

6. EXPERIMENTAL ROAD MAP

and subtracting 5% from the round beam assumption. The uncertainties of the relative variation of the strand resistance, $\Delta(\frac{\Delta R}{R_i})$, were included in the fitting and can be expressed as the following:

$$\Delta\left(\frac{\Delta R}{R_i}\right) = \frac{U_{i_{m\Omega}}}{U_i^2 U_{f_{m\Omega}}} (U_i + U_f) \Delta U_{pp} + \frac{U_f}{U_{i_{m\Omega}} U_i} (U_{i_{m\Omega}} + U_{f_{m\Omega}}) \Delta U_{m\Omega_{pp}} \quad (6.7)$$

where ΔU_{pp} and $\Delta U_{m\Omega_{pp}}$ are the measured peak to peak noise levels varying between 2 and 4 μV depending on the channel.

The energy deposition in each of the cable stacks E_{st} was derived from the measured peak energy deposition in the strands $E_{s_{meas}}$ and the ratio of the peak energy deposition in the cable stacks over the peak energy deposition in strands $(E_{st}/E_s)_{sim}$ obtained by FLUKA simulations (see Appendix C) with the following equation:

$$E_{st} = (E_{st}/E_s)_{sim} \cdot E_{s_{meas}}, \quad (6.8)$$

The peak temperature reached in the cables stacks was then derived from the energy deposition using the heat capacity of the cables.

Cooling profile

The cooling of the strands and the cable stacks after the beam impact were simulated in ANSYS.

The main cooling mechanism of the strands was identified to be heat conduction along the strands and the voltage drop measurement cables. The evolution of the strand average temperature rise normalized to its maximum $\Delta T_{avg}/\Delta T_{max}$ obtained by the model was compared to measurements at two beam intensities. The comparison between such measurements done on the two Nb_3Sn strands after the impact of 1.3×10^{12} (blue) and 2.6×10^{12} protons (red) with the model (dashed line) is shown in Fig. 6.28. At the beam impact time (time=0 s), the average temperature rise is maximum thus $\Delta T_{avg}/\Delta T_{max}=1$. The model and the measurements are in good agreement.

Assuming a initial energy deposition with a Cauchy-Lorentz profile with $\gamma=1.8$ mm and $x_0=0$ mm, the temperature evolution of a Nb_3Sn strand after the impact of 2.6×10^{12} protons was simulated. In Fig. 6.29 is shown the evolution of the temperature at different longitudinal positions along the strand (0 mm being at the beam impact location) as function of time after the beam impact. The cooling constant $t_{1/2}$ defined as the time when the peak temperature is reduced by half, at the strand's impact location (0 mm), was estimated to about 84 ms and 2 mm away from the impact to about 490 ms.

6.4 Measurements of insulation and superconductor degradation due to beam impact

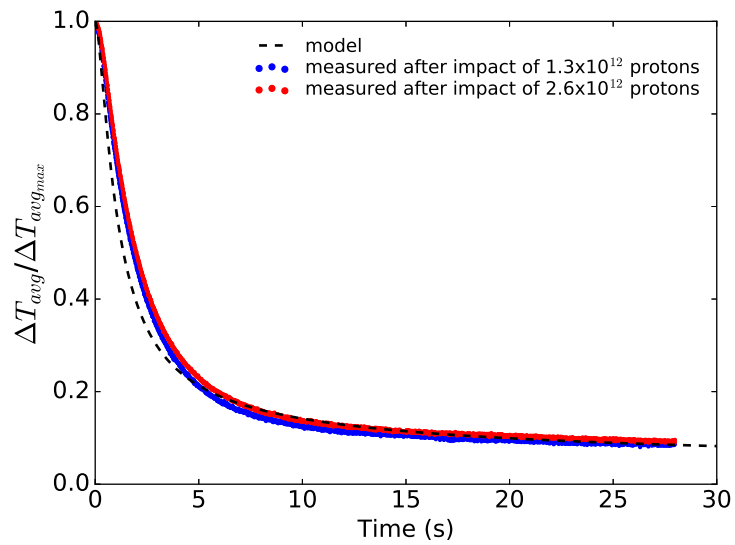


Figure 6.28: Comparison of the strand average temperature rise normalized to its maximum $\Delta T_{avg}/\Delta T_{max}$ as function of time after the beam impact obtained by the model (dashed line) and by two measurements done on Nb_3Sn strands after the impact of 1.3×10^{12} protons (blue) and 2.6×10^{12} protons (red). At the beam impact time (time=0 s), the average temperature rise is maximum, i.e. $\Delta T_{avg}/\Delta T_{max}=1$ and then the strand starts to cool down, i.e. $\Delta T_{avg}/\Delta T_{max}$ decreases. The model and the measurements are in a good agreement.

6. EXPERIMENTAL ROAD MAP

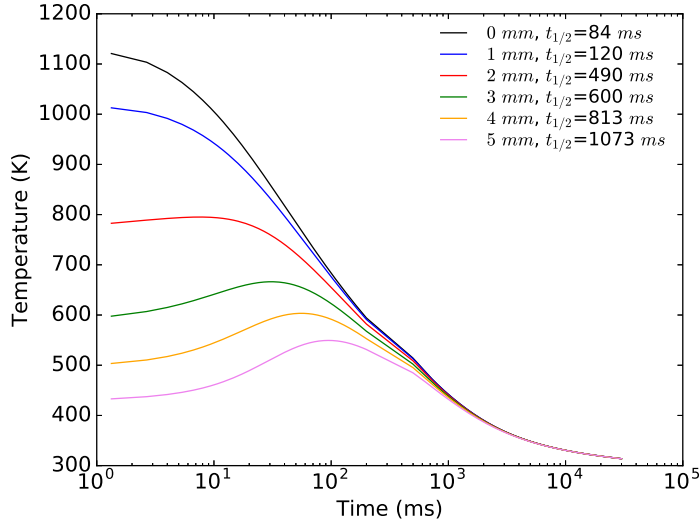


Figure 6.29: Temperature at different longitudinal position of the strand as a function of time after the impact of 2.6×10^{12} protons, as obtained from ANSYS simulation. The position along the strand are referring to the beam impact location, 0 mm being at the centre of the beam impact location (black). $t_{1/2}$ being the time at which the peak temperature is reduced by half.

The main cooling mechanism of the cable stacks was identified to be heat conduction longitudinally along the cable and transversally toward adjacent cables. A stack of three cables was modelled in ANSYS as three copper rectangular parallelepiped of 200 mm length and 2 mm thickness with between each parallelepiped a $300 \mu\text{m}$ thick layer of polyimide. A sketch of the three cable stack model is shown in Fig.6.30. The temperature at the cable extremities was fixed to room temperature. The copper and polyimide heat capacity and thermal conductivity were obtained from [75]. A hot spot with a peak temperature of about 1050 K induced by a energy deposition with Cauchy-

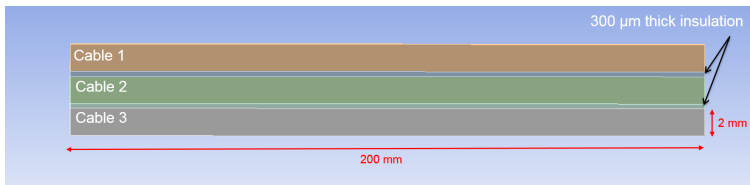


Figure 6.30: Model of a three cable stack. The cables are 200 mm long and 2 mm thick. A $300 \mu\text{m}$ thick polyimide insulation layer is inserted between each cables. Cable 2 is the central cable aligned with the beam axis.

6.4 Measurements of insulation and superconductor degradation due to beam impact

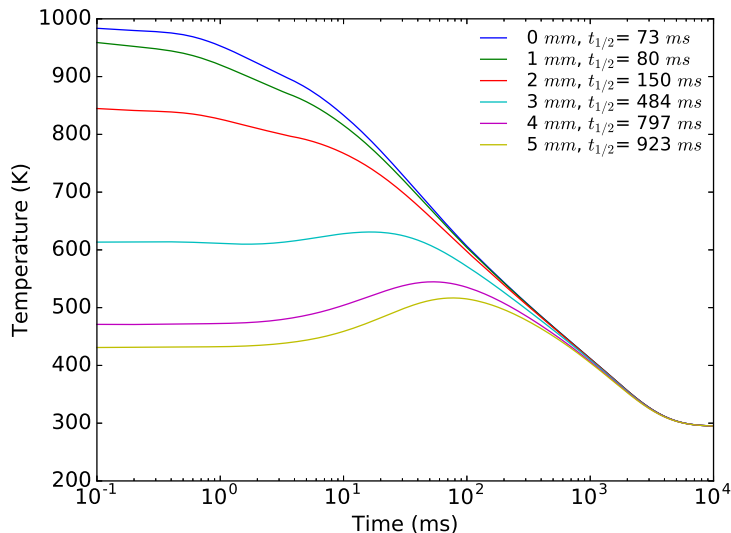


Figure 6.31: Temperature evolution as obtained from ANSYS simulation, at different longitudinal positions of a insulated Nb-Ti cable after beam impact. The energy deposition has an horizontal Cauchy-Lorentz distribution with $\gamma=1.8$ mm and $x_0=0$ mm. In the centre of the beam impact location (0 mm, black curve), the cooling time $t_{1/2}$ was estimated to 73 ms, and at 2 mm from the centre of the beam impact location (2 mm, red curve) to 150 ms.

Lorentz distribution with $\gamma=1.8$ mm and $x_0=0$ mm was set as initial condition. The evolution of the temperature at different longitudinal positions along the middle cable (cable 2) as function of time after the beam impact is shown in Fig. 6.31. The cooling constant $t_{1/2}$ of the hot spot in the cable was estimated to 73 ms.

6.4.4 Analysis of irradiated samples

After few weeks of radioactive cool-down, the set-up was removed from the tunnel and the samples were extracted for analysis.

To measure the degradation of the insulation, dielectric strength measurements were performed on the cable stacks using voltages up to 35 kV. The measurement set-up and process were similar to the one described in section 6.2. After the dielectric strength tests, the stacks were dismantled for visual inspection, to localize the beam impact and the breakthrough. As the moulds and cable stacks were activated (maximum dose at contact was about 100 mSv/h), the measurements and inspections were performed in a radioactive control area and special precautions had to be taken.

6. EXPERIMENTAL ROAD MAP

The reduction of the critical current was measured via magnetization measurements performed on beam impacted region of the strand with a length of 4 mm. The 4 mm long central part of the strands were extracted from the 3 cm long strand. The same preparation procedure was followed as for the sample of the capacitive discharge experiment: first the strands were cut using a wire cutter and then both extremities of the extracted part were polished away. The measurements were performed with an applied magnetic field perpendicular to the strand axis reaching a maximum of 7 T with a sweep rate of 0.3 T min^{-1} . Magnetization was measured at at 2 K, 4 K and 6 K for Nb-Ti and 2 K, 4 K, 10 K and 15 K for Nb₃Sn.

7

Insulation degradation results and analysis

The degradation of the insulating property of the polyimide is a consequence of its decomposition when exposed to high temperature. The decomposition reaction produces solid products which consist mainly (95%) of glassy carbon, which is a good conductor [98] and therefore reducing the polyimide dielectric strength. Mass loss of the polyimide is also a consequence its decomposition. A model of the mass loss as function of temperature and exposure time has been developed (see section 5.3.2)

In this chapter the results of the visual inspection and of the dielectrics strength of the cable insulation measurements for all stacks heated in the furnace and beam experiment are presented. Then the mass loss model is benchmarked to the measured mass loss in the furnace experiment. Comparing the measured mass loss and dielectric strength, a mass loss threshold above which dielectric strength degrades is determined. Finally predictions of the insulation degradation derived from the mass loss model and threshold are compared to the measured degradation of the samples impacted by proton beam.

7.1 Dielectric strength measurements and visual inspection after heating

Fig. 7.1 shows a comparison of the side views of the cable stacks after heating in the furnace. The peak temperatures reached are indicated. For temperatures up to 623 K, no change can be identified visually. Changes can be identified from 678 K, when the adhesive film coated on the insulation starts turning black. From 728 K, all three

7. INSULATION DEGRADATION RESULTS AND ANALYSIS

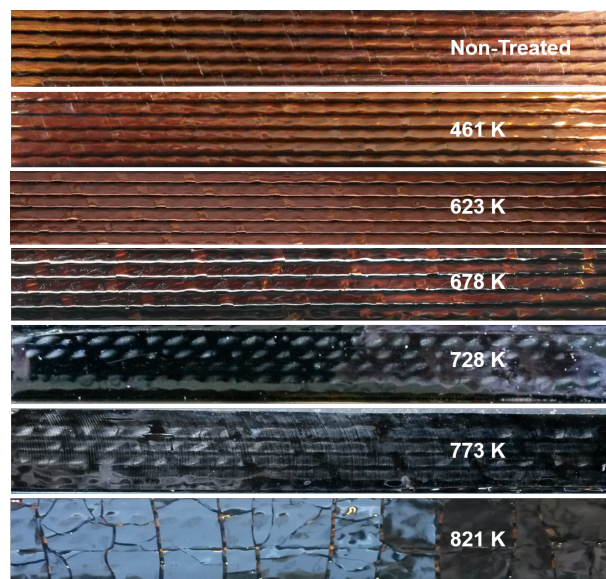


Figure 7.1: Cable stacks (side view) before and after heating with different peak temperature. Changes can be identified from 678 K, when the adhesive film coated on the insulation starts turning black. Above 728 K, all three insulation layers turn black and above 821 K cracks appear.

insulation layers turn black and from 821 K cracks appear. Picture of the stacks heated up to 864 K is not available. The results of the measurements of the dielectric strength after heating of the cable stacks in the furnace are shown in Fig. 7.2. Crosses indicate that no breakdown was achieved with voltage up to 20 kV, round markers indicate that a breakdown was observed. The dashed line indicates the minimum breakdown voltage as a function of temperature.

The results of the breakdown voltage measurements on samples impacted by the proton beam are shown in Fig. 7.3. The black markers indicate the breakdown voltages measured on samples exposed to the beam. The green crosses indicate that the breakdown took place at the position of the beam impact. Visual inspection of each cable were performed to localize the position of the beam impact and of the voltage breakdown. Fig. 7.4 shows a dismantle cable stack after the irradiation and the dielectric strength measurements. The five white spot indicated by the white arrows mark the impact of the proton beam, the peak temperatures reached in these zones were between 950 K and 1050 K. The black traces indicated by the black arrows mark the consequences of the breakdown.

The dielectric strength of non-treated samples was found to be between 16.3 kV and 28.5 kV which is in good agreement with earlier measurements [85]. After heating

7.1 Dielectric strength measurements and visual inspection after heating

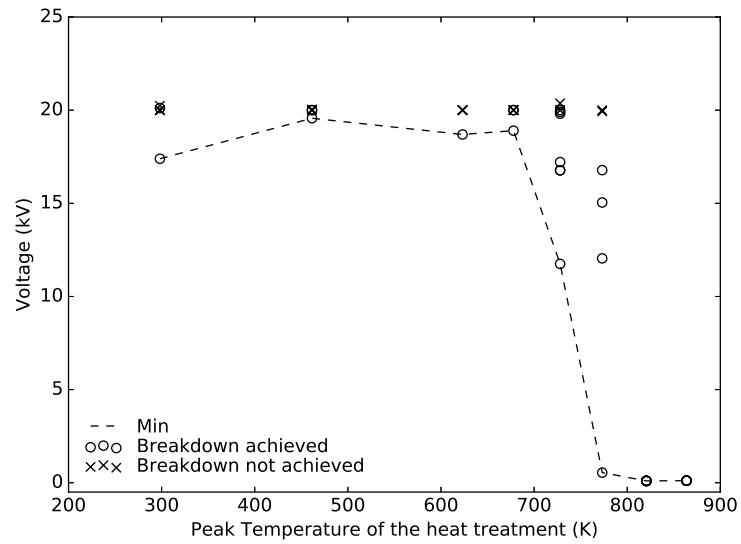


Figure 7.2: Results of the dielectric strength measurements after heating for several hours at different peak temperatures in a furnace. The crosses indicate that no breakdown was achieved with voltage up to 20 kV, the round markers indicate that a breakdown was observed. The dashed line indicates the minimum breakdown voltage. The minimum breakdown voltage of reference samples is about 17 kV. Degradation of the insulation was observed for peak temperatures above 678 K.

7. INSULATION DEGRADATION RESULTS AND ANALYSIS

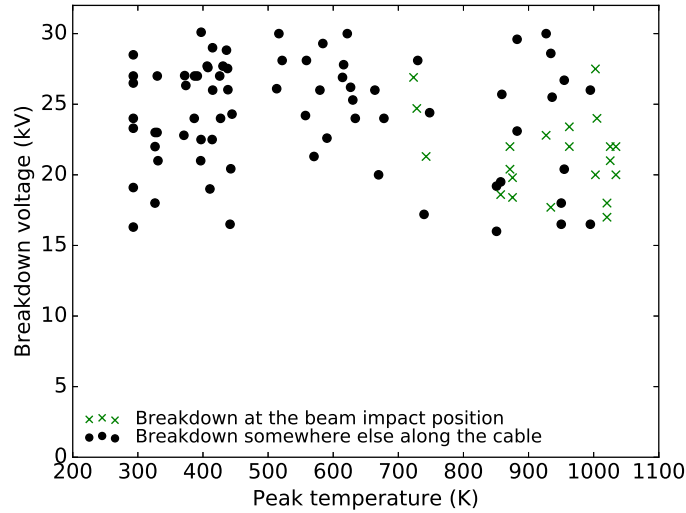


Figure 7.3: Breakdown voltage as function of the peak temperature reached in the cable stacks after interaction with a 440 GeV $0.6 \mu\text{s}$ proton beam. No degradation can be observed, however, above 850 K breakdown of the insulation took place at the location of beam impact for about 55% of the samples indicating a weakening of the insulation.

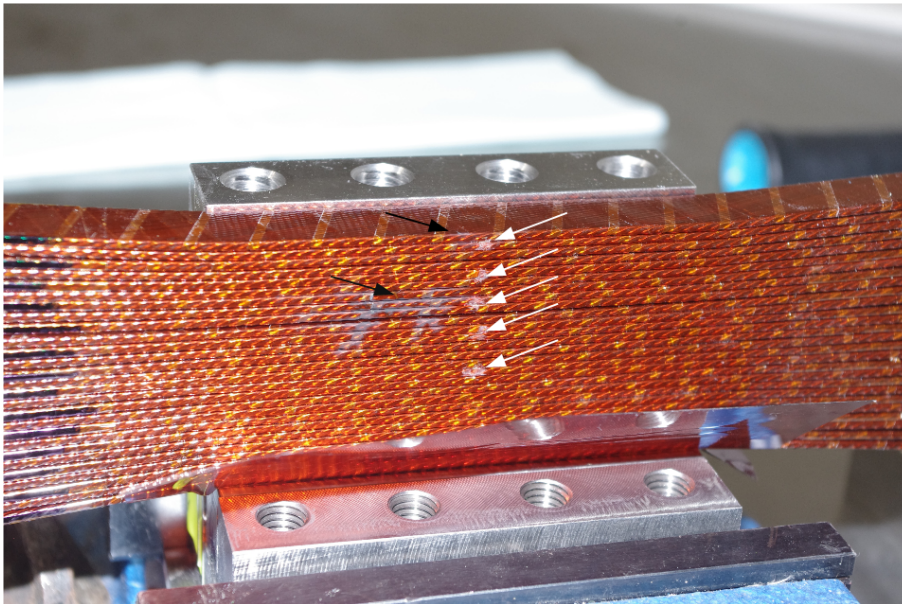


Figure 7.4: Side view of a Nb-Ti cable stack after beam impact. The five white spots at the centre of the stack indicated by the white arrows the impact of the proton beam, the peak temperatures reached in these zones were between 950 K and 1050 K. The black traces indicated by the black arrows are the consequences of the breakdown.

during several hours, degradation of the insulation was observed for peak temperatures above 678 K, the breakdown voltage was measured at 11.7 kV. At 773 K, a breakdown voltage of 0.5 kV was measured, which indicates the destruction of the sample insulation. From 821 K, the cables were in electrical contact after the heating, with resistance cable to cable ranging from 30 k Ω to 3 M Ω . These results confirm the interpretation after the visual inspection of the stacks (see Fig. 7.1). No degradation was measured on the samples exposed to beam reaching temperatures up to 1035 K. However, for peak temperatures above 850 K, the breakdown of the insulation took place at the location of beam impact for about 55% of the samples indicating a weakening of the insulation. Multiple beam impacts at the same spot, might lead to a degradation and later failure of the insulation.

The variation of the measured breakdown voltages within each measurement set can be explained by in-homogeneities in the samples. These variations have to also be expected in LHC magnets due to the significant length of the used cables (e.g. \sim 2400 m for one dipole magnet aperture).

7.2 Mass loss

Mass loss measurements were performed on insulation tapes with a thickness of 50 μm and 125 μm heated in the furnace experiment. Measurement were performed on ten tape samples per peak temperatures, five of each thickness. By inserting the temperature profiles of the polyimide samples during their exposure to high temperature (see Fig. 6.8) in the mass loss model (see equation (5.7)) and solving it numerically, the expected polyimide sample mass losses were calculated. The comparison between the model and the measurement is shown in Fig. 7.5. The dashed lines show the expectation from the mass loss model. The round markers are the average of the mass loss measured over the ten samples and the error bars are the standard deviation of the measured mass loss. The measurements and the model are in good agreement.

To determine the mass loss threshold above which the insulating property of the polyimide starts to degrade, the mass loss and the lowest breakdown voltages measured on samples heated to different peak temperature in a furnace were compared (see Table 7.1). Below 678 K, the mass loss of the samples was not measurable. The minimum resolution of the balance was 0.5×10^{-3} . For a mass loss below 4×10^{-3} no degradation of the dielectric strength was measured. A mass loss between 4×10^{-3} and 2.9×10^{-2} indicates a reduction of the dielectric strength and above 2.9×10^{-2} the polyimide dielectric strength is lost.

7. INSULATION DEGRADATION RESULTS AND ANALYSIS

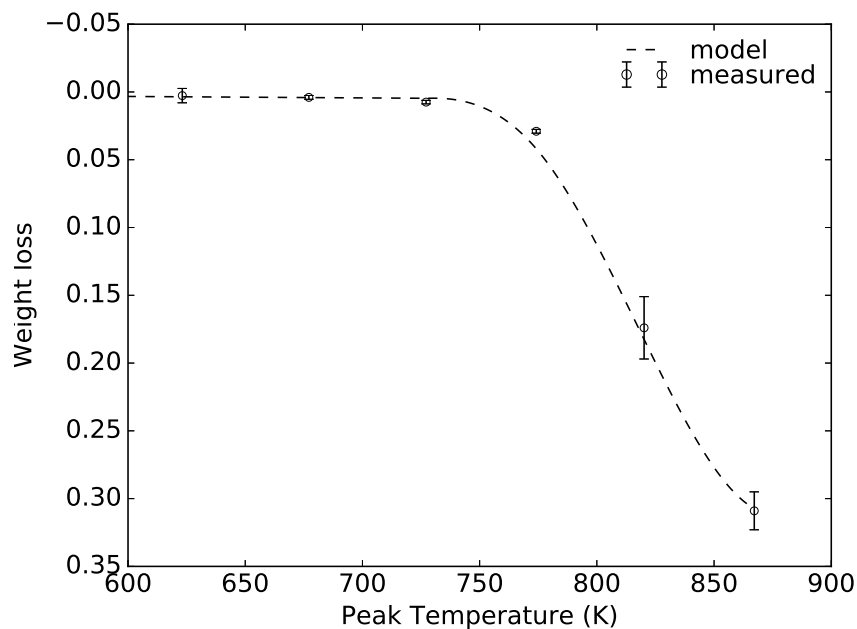


Figure 7.5: Mass loss of polyimide sample as function of peak temperature. The dashed lines show the expectation from the model, the round markers are the average of the mass loss measured over the ten samples after heating in the furnace and the error bars are standard deviation of the measured mass loss.

Table 7.1: Lowest breakdown voltage measured on cable stacks and average mass loss of polyimide tape measured after heating to peak temperature in the left column.

Peak temperature (K)	Average mass loss (%)	Lowest breakdown voltage (kV)
Non Treated	-	17.4
461	-	19.6
623	-	18.7
678	$4 \times 10^{-3} \pm 1.4 \times 10^{-3}$	18.9
728	$7.5 \times 10^{-3} \pm 1.3 \times 10^{-3}$	11.7
773	$2.9 \times 10^{-2} \pm 0.14 \times 10^{-2}$	0.5
821	$17.4 \times 10^{-2} \pm 2.3 \times 10^{-2}$	0
864	$30.9 \times 10^{-2} \pm 1.4 \times 10^{-2}$	0

From the mass loss model and threshold, degradation of polyimide insulation impacted by a proton beam can be predicted. Solving the mass loss model with the temperature profile of the cable stack obtained from the thermal model with highest peak temperature (1035 K) and time constant $t_{1/2}=73$ ms (see Fig. 6.31) results in a mass loss of 4×10^{-5} , two orders of magnitude below the degradation loss threshold. No degradation is expected for such mass loss, which is compatible with observations. However it is interesting to mention that for a peak temperature of 1280 K, the model predicts a mass loss in the order of 4.2×10^{-3} , which is slightly above the degradation determined from the furnace experiment.

7. INSULATION DEGRADATION RESULTS AND ANALYSIS

8

Critical current density degradation results and analysis

In this chapter the results of the magnetization and microscopic measurements performed on Nb-Ti and Nb₃Sn strands after capacitive discharge and beam impact are presented and discussed. The magnetization of the samples was measured in order to assess the degradation of their superconducting properties (critical current density J_c , pinning force density F_p , critical field H_{c20} and critical temperature T_{c0}). Microscopic analyses were performed to observed changes of the superconductor microstructure and chemical composition. The detailed description of the experimental set-ups can be found in section 6.3.2 and 6.3.3.

8.1 Nb-Ti results and discussion

8.1.1 Magnetization measurement results

J_c of the NB-Ti strands is related to its magnetization hysteresis width per unit volume ΔM via equation 5.6 assuming an effective filament diameter of 7 μm . Thus, in order to assess the J_c degradation of the Nb-Ti strand samples, their magnetization was measured at 2 K, 4 K and 6 K under an applied field H_{\perp} perpendicular to the samples with $\mu_0 H_{\perp}$ up to 7 T. The measurements results are shown for samples heated by capacitive discharge ($t_{1/2} \sim 6$ s) in Fig 8.1 and for samples heated by interaction with a proton beam pulse in Fig 8.2. For the capacitive discharge case, no degradation is observed up to 651 K and for the beam impact case up to 879 K. Above these temperatures in both cases, ΔM decreases and therefore J_c too. The sample reaching 935 K due to beam impact is an exception, no degradation is observed. It suspected

8. CRITICAL CURRENT DENSITY DEGRADATION RESULTS AND ANALYSIS

that during the sample preparation before the magnetization measurements, the sample was cut at the wrong position - not centred on the beam impacted region. Therefore this sample is excluded from the analysis. An increase of ΔM at external fields below 2 T is visible in the samples heated by the capacitive discharge to peak temperatures above 1068 K. This is caused by an increase of the effective filament diameter, d_f , as verified by microscopy analysis.

The pinning force density F_p is derived from the measured ΔM using equation 5.1 and 5.6. The magnetic field and temperature scaling law of the pinning force density F_p (see equation 5.2) was fitted to the F_p derived from the measurement performed at 2 K, 4 K and 6 K using eight fitting parameters (p , q , $H_{c2}(2K)$, $H_{c2}(4K)$, $H_{c2}(6K)$, $C(2K)$, $C(4K)$ and $C(6K)$). As an example, Fig 8.3 shows F_p of the Nb-Ti reference sample as a function of applied external field H_{\perp} at 2 K, 4 K and 6 K. The value of the fitting parameters p , q and the set of C and H_{c2} are indicated in the figure. The scaling law fits well the measurements.

The fitting parameters p and q versus the peak temperature are shown in Fig 8.4. The p and q value obtained for the capacitive discharge are in the expected range, i.e. 0.5–0.9 for p and 0.75–1.1 for q [67], up to 833 K. A decrease of p and q is observed in the sample heated to 916 K. For samples heated to temperature equal or above 1068 K, large values of q are obtained, while p shows a relatively small decrease. For all the samples heated by beam interaction, p and q stay relatively stable except for the samples heated up to 925 K and 933 K for which p and q drop below the expected values. p is about 0.3 while the expected minimum is 0.5 and q is about 0.7 while the expected minimum is 0.75.

The H_{c2} values obtained from the F_p scaling law as a function of the magnetization measurement temperature are shown for the samples heated by capacitive discharge in Fig. 8.5 (a). The dashed lines are obtained from the critical upper field scaling law (see equation 5.3) fitted to the H_{c2} values with H_{c20} and T_{c0} as fitting parameters. The resulting H_{c20} and T_{c0} values as a function of the peak temperature reached in the samples are shown in Fig. 8.5 (b). H_{c20} of the reference sample is about 15.4 T, which is higher than the expected 14.5 T. This can be explained by the error induced by the extrapolation done on the measured data from 7 T up to the critical field at 2 K and 4 K. Even though the absolute H_{c20} values are subject to an error of ± 1 T, the relative change of H_{c20} along the set of samples is still of interest. No significant variation of H_{c20} were observed up to peak temperatures of 833 K. It decreases from 916 K reaching about 4.5 T for a peak temperature of 1157 K. T_{c0} varies between 8 and 9 K with the exception of the sample heated up to 916 K where $T_{c0}=10.4$ K.

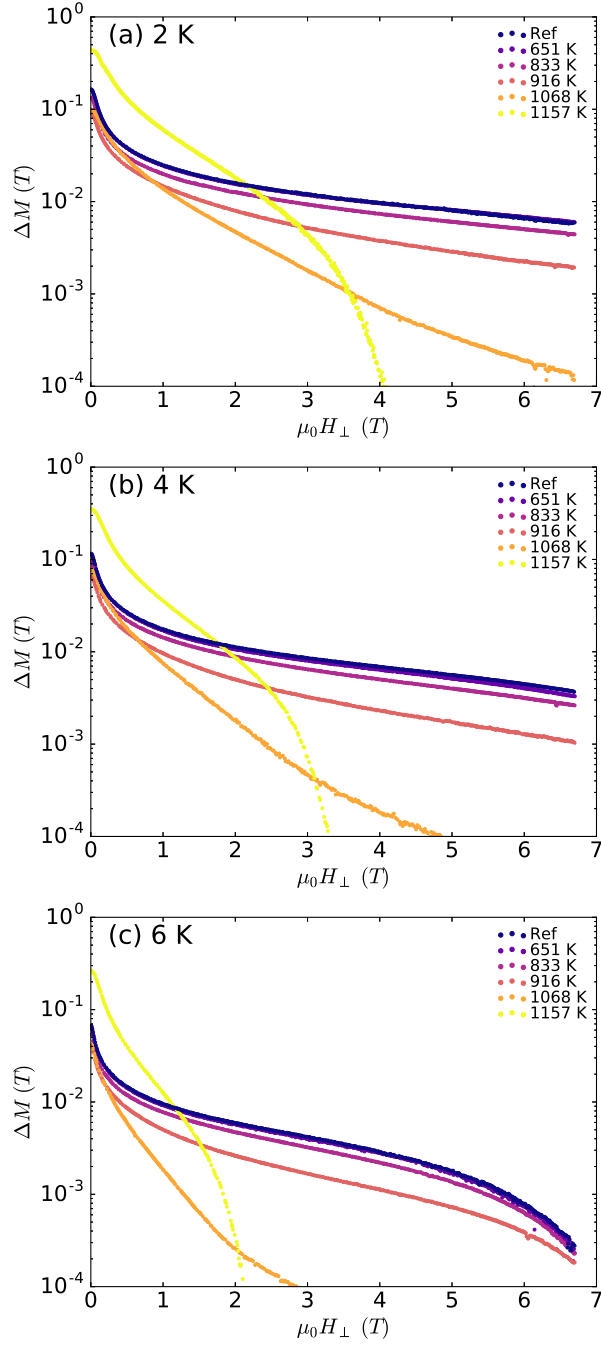


Figure 8.1: Hysteresis width of the magnetization per unit volume, ΔM , of Nb-Ti strands as a function of the external magnetic field H_{\perp} up to $\mu_0 H_{\perp} = 7$ T, after heating due to a capacitive discharge ($t_{1/2} = 6$ s) measured at 2 K (a), 4 K (b) and at 6 K (c).

8. CRITICAL CURRENT DENSITY DEGRADATION RESULTS AND ANALYSIS

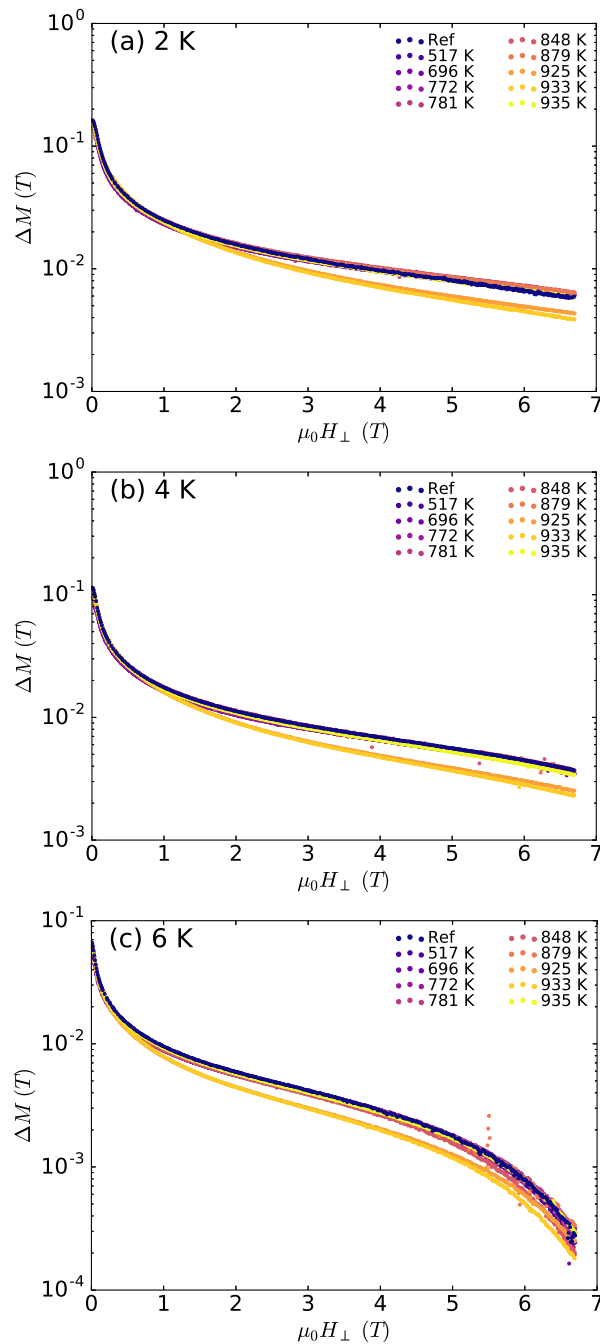


Figure 8.2: Hysteresis width of the magnetization per unit volume, ΔM , of Nb-Ti strands as a function of the external magnetic field H_{\perp} up to $\mu_0 H_{\perp} = 7$ T, after heating due to interaction with a proton beam ($t_{1/2} = 84$ ms) measured at 2 K (a), 4 K (b) and at 6 K (c).

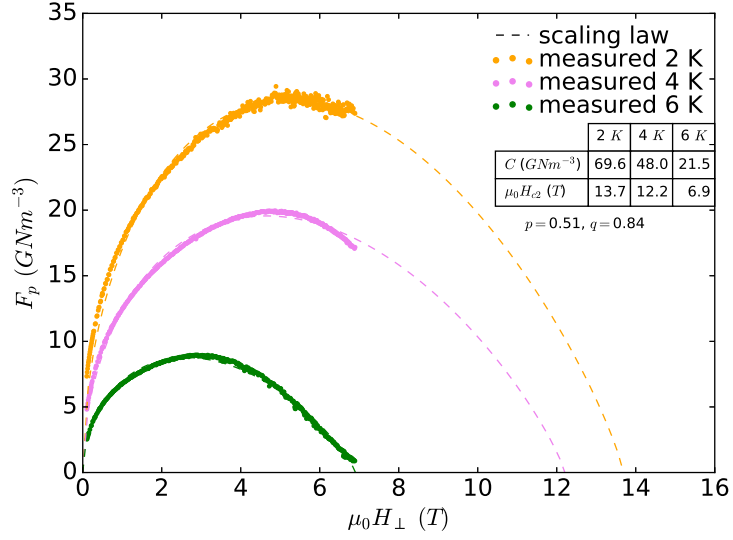


Figure 8.3: Comparison of F_p as function of $\mu_0 H_{\perp}$ of the reference Nb-Ti sample obtained by measurement and by the scaling law at 2 K, 4 K and 6 K. The obtained fitting parameters p , q , $C(T)$ and $H_{c2}(T)$ are indicated.

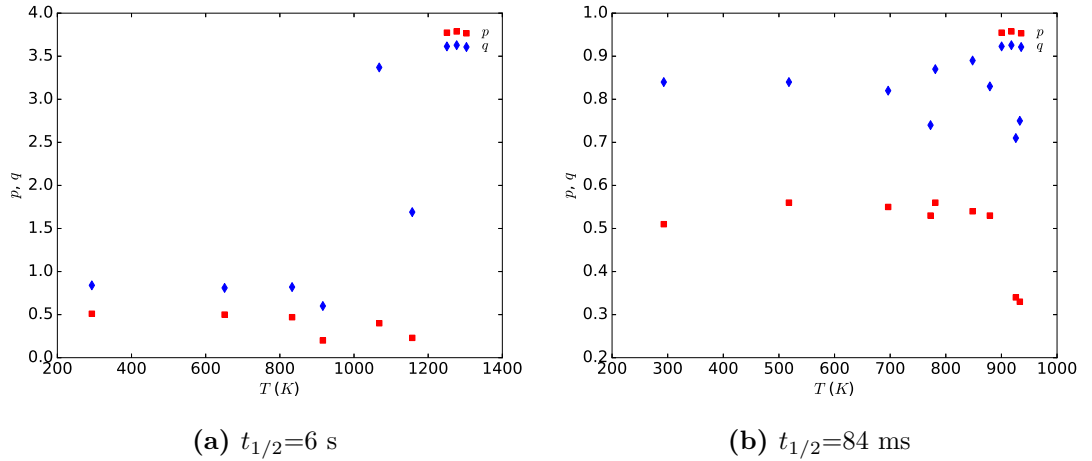


Figure 8.4: The fitting parameters p and q of the F_p scaling law (see equation 5.2) as function of the peak temperature reached in Nb-Ti strands after heating due to capacitive discharge ($t_{1/2}=6$ s) and being exposed to proton beam ($t_{1/2}=84$ ms).

8. CRITICAL CURRENT DENSITY DEGRADATION RESULTS AND ANALYSIS

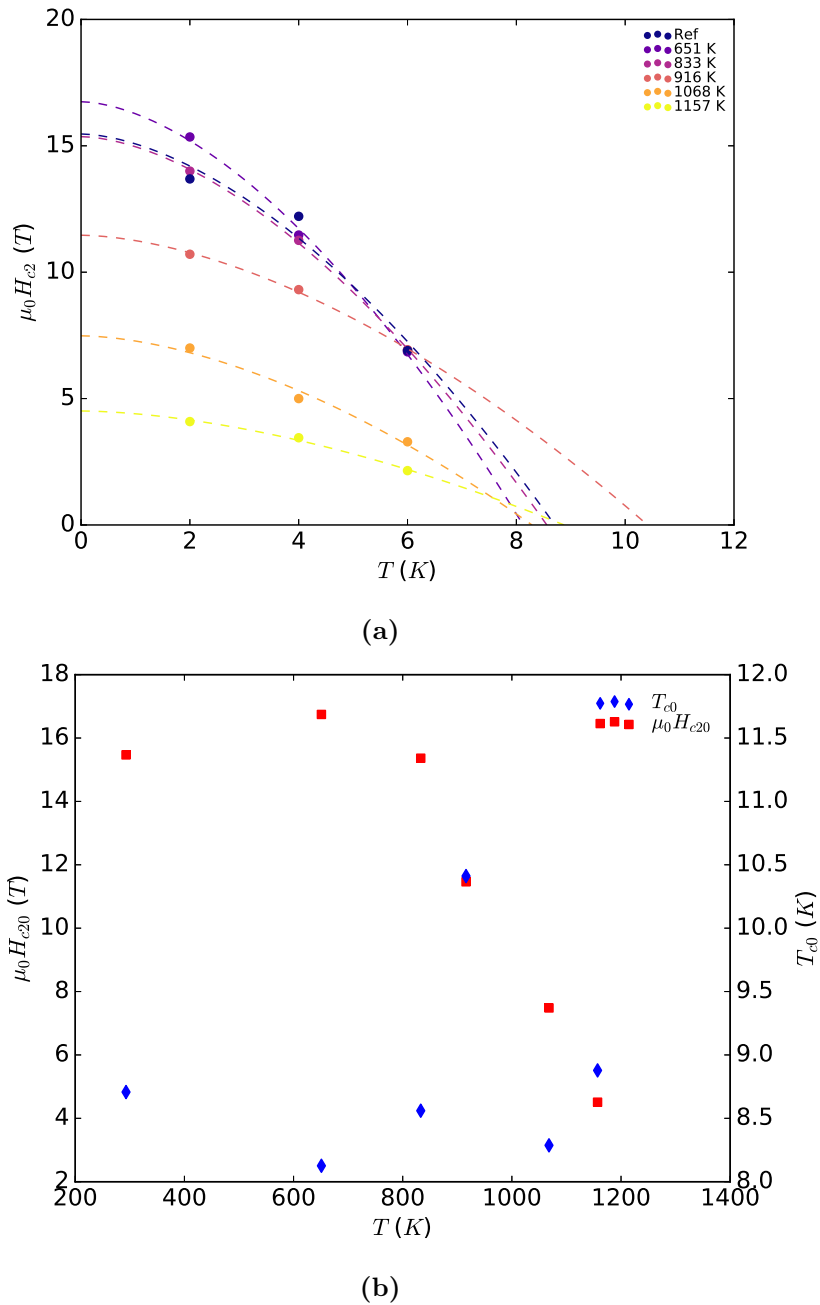


Figure 8.5: H_{c2} , H_{c20} and T_{c0} obtained for the Nb-Ti samples after heating due to capacitive discharge. (a) $\mu_0 H_{c2}$ as a function of the magnetization measurement temperature. The dashed lines are obtained from the critical upper field scaling law (equation 5.3). (b) $\mu_0 H_{c20}$ and T_{c0} as function of peak temperature achieved in the samples obtained from the fitting of equation 5.3 to the H_{c2} values.

H_{c2} of the Nb-Ti samples after being exposed to proton beam as a function of the magnetization measurement temperature is shown in Fig 8.6 (a) and H_{c20} and T_{c0} as function of peak temperature in Fig 8.6 (b). The H_{c20} and T_{c0} sample to sample variations are dominated by the extrapolation method uncertainties.

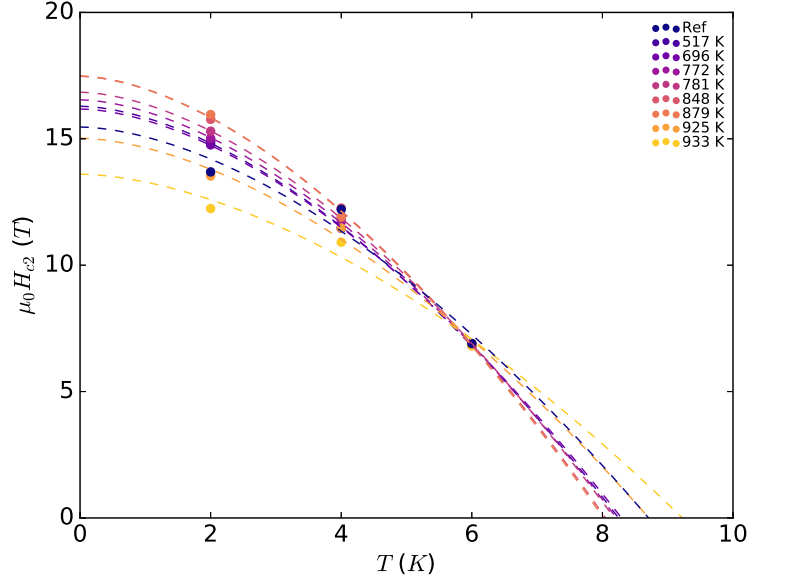
The pinning force density F_p measured at 2 K, 4 K and 6 K versus the reduced field b is shown for capacitive discharge in Fig. 8.7 and proton beam interaction in Fig. 8.8. b is defined as $b = H_{\perp}/H_{c2}$. No significant change of F_p is observed up to a peak temperature of 651 K in the capacitive discharge case and up to 879 K for the beam impact case. Above these temperature for both cases, the maximum of F_p is significantly reduced and shifted from 0.5 b to a lower b value, reaching $\sim 0.1 b$ for the 1068 K sample heated via capacitive discharge and $\sim 0.3 b$ for the 933 K sample impacted by a proton beam. Such F_p variations indicate a change in the pinning behaviour of the superconductor and, thus, a change in the superconductor microstructure. An increase of the maximum of the pinning force density at 2 K can be observed after interaction with a proton beam for the 848 K and 879 K samples.

The relative change of magnetization of Nb-Ti strands measured at 2 K, 4 K and 6 K, at an applied field of 3 T and 5 T as a function of the peak temperature for different heating time constants is shown in Fig. 8.9. The relative reduction of the magnetization after a 5 minutes long heat exposure was extracted from [101]. A $t_{1/2} \sim 6$ s long exposure with a peak temperature of ~ 833 K and a $t_{1/2} \sim 84$ ms long exposure with a peak temperature of ~ 930 K lead to a similar relative change of the magnetization, thus, of J_c of about 30% at 5 T and 4 K (see Fig. 8.9 (d)). From Fig. 8.9, it can be observed that for the same peak temperature the reduction of J_c increases with the exposure time.

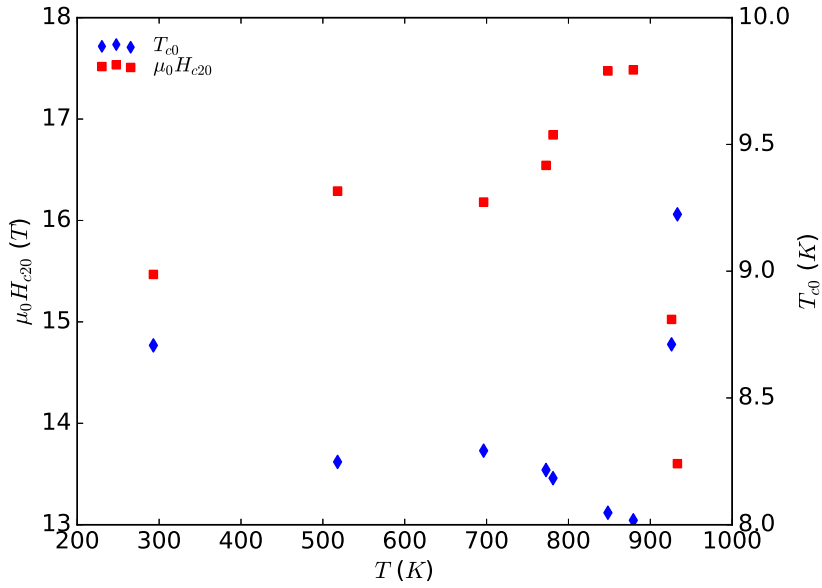
8.1.2 Microscopic analysis results

Optical microscopic analysis was performed on the Nb-Ti reference sample and on the sample heated by capacitive discharge to a peak temperature of 1157 K (see Fig. 8.10). Both samples were polished and etched before inspection. In Fig. 8.10 (a) to (c), the filament structure (grey) embedded in the copper matrix (light orange), the single filaments and even the copper grains of the reference sample are clearly visible. In Fig. 8.10 (d) the cross section of the heated strand is shown, part of the copper was oxidized and appears black (left). An increase of the copper grain size compared to the reference sample can be seen in Fig. 8.10 (e). The merging of the filaments is clearly visible in Fig. 8.10. Using polarized light in Fig. 8.10 (f) exhibits several phases in the

8. CRITICAL CURRENT DENSITY DEGRADATION RESULTS AND ANALYSIS



(a)



(b)

Figure 8.6: H_{c2} , H_{c20} and T_{c0} obtained for the Nb-Ti samples after being exposed to proton beam. (a) $\mu_0 H_{c2}$ as a function of the magnetization measurement temperature. The dashed lines are obtained from the critical upper field scaling law (equation 5.3). (b) $\mu_0 H_{c20}$ and T_{c0} as function of peak temperature achieved in the samples obtained from the fitting of equation 5.3 to the H_{c2} values.

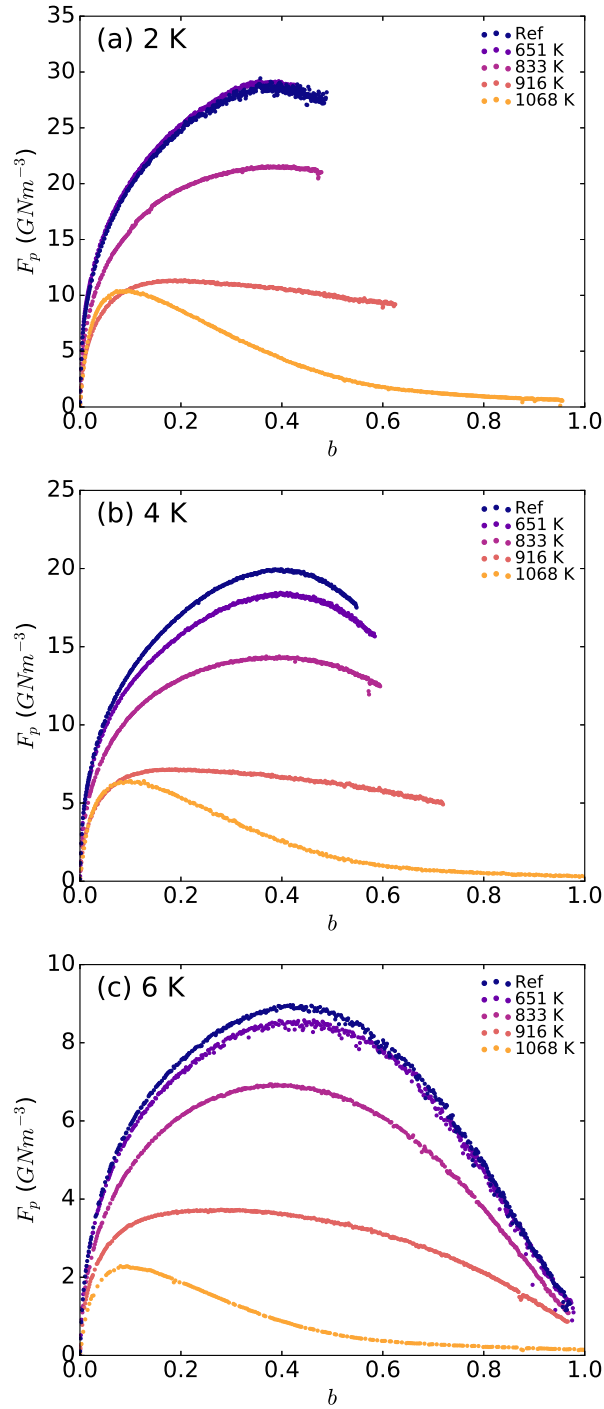


Figure 8.7: Pinning force density F_p of Nb-Ti strands vs. reduced field b after heating due to a capacitive discharge $t_{1/2}=6$ s measured at 2 K (a), 4 K (b) and at 6 K (c).

8. CRITICAL CURRENT DENSITY DEGRADATION RESULTS AND ANALYSIS

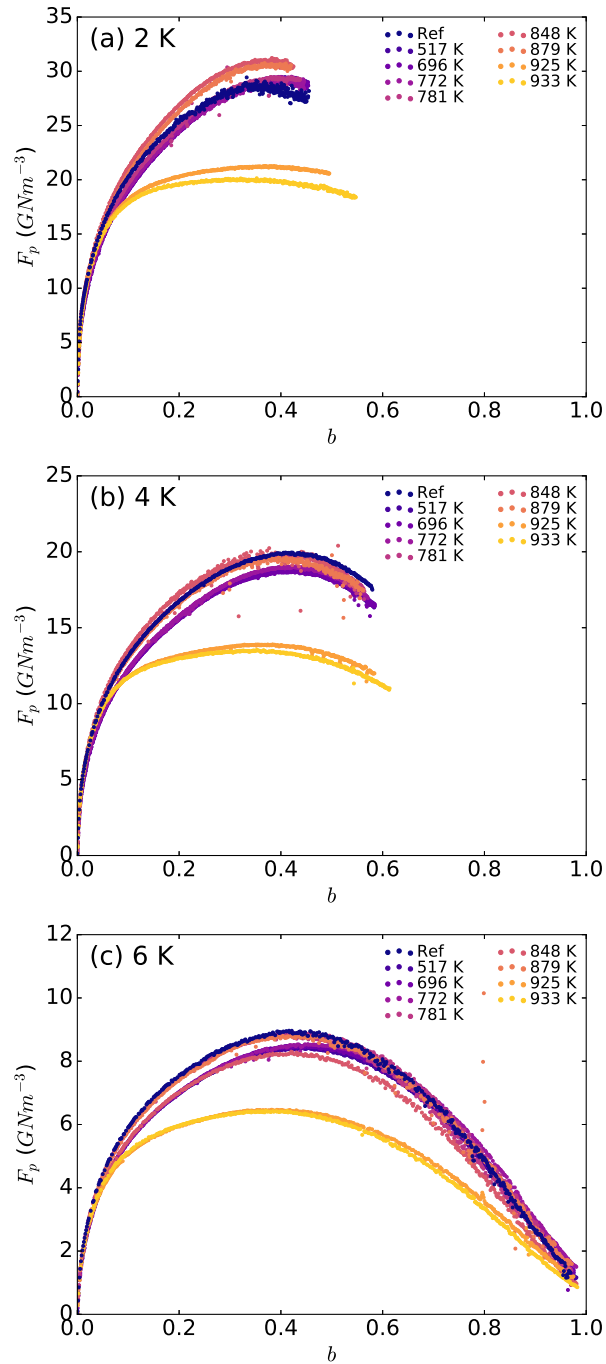


Figure 8.8: Pinning force density F_p of Nb-Ti strands vs. reduced field b after heating due to interaction with a proton beam $t_{1/2}=84$ ms measured at 2 K (a), 4 K (b) and at 6 K (c).

8.1 Nb-Ti results and discussion

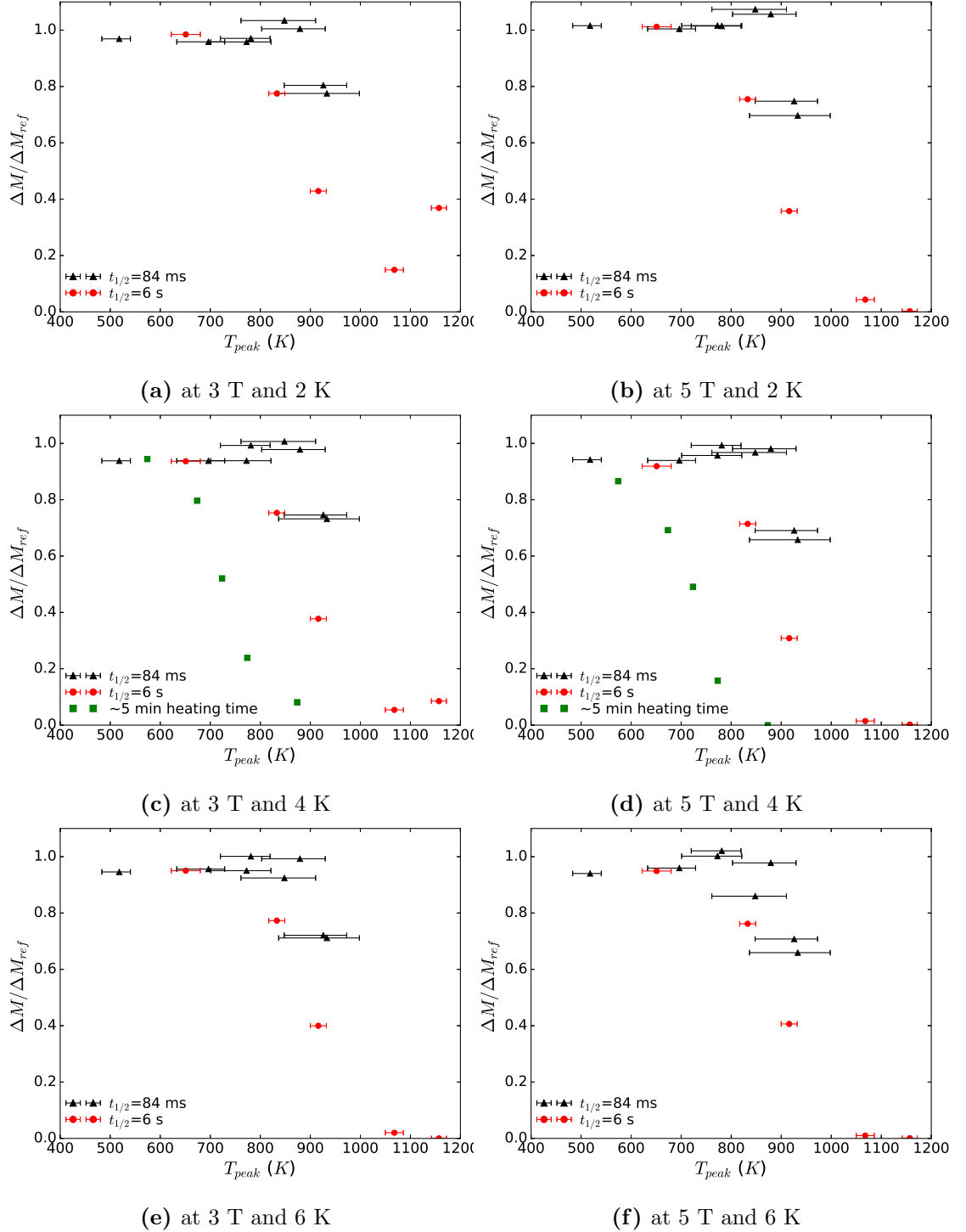


Figure 8.9: Relative change of magnetization measured at different temperatures and applied field vs. peak temperature reached in Nb-Ti strands for three different heating timescales. The data for the 5 minutes heating measured at 4 K are from [101].

8. CRITICAL CURRENT DENSITY DEGRADATION RESULTS AND ANALYSIS

merged filaments: fine particles of Nb (white), Cu-Ti inter-metallic compound (light grey) and residuals of the Nb-Ti filaments (dark grey).

The results of an energy dispersive X-ray spectrometry (EDX) and backscattered electron (BSE) analysis are shown in Fig. 8.11 and Fig. 8.12. In the pictures obtained with BSE the lighter phases appear in dark colour and heavier in light colour. The weight fraction composition was obtained from the EDX. The samples were polished before measurements. On both picture of Fig. 8.11, the copper matrix, the Nb-Ti filaments and the Nb diffusion barrier around each filament appear in dark grey, grey and white, respectively. An EDX analysis shows that the Ti weight fraction in the Nb-Ti filaments is 47% as expected (see Table 5.1) and that the copper matrix composed of 100% of Cu (see Fig. 8.11). In the pictures of Fig. 8.12, a group of filaments of the heated sample and a zoom on the edge of the group of filaments are shown. The formerly well separated Nb-Ti filaments built a conglomerate of different phases (different greys).

The composition of the different phases was analysed via EDX, however the volume of the observed phases is in the range or smaller than the minimum resolution of the analysis of $1 \mu\text{m}^3$. Therefore, the weight fraction composition given in the table below Fig. 8.12 is a mix of the compositions of the surrounding phases, which allows only for a qualitative interpretation of the results. In the right pictures in Fig. 8.12, the grey phase (spectrum 8 and 9) is the copper matrix, the dark grey phases (spectrum 10) are a Cu-Ti inter-metallic compound, the white phases (spectrum 11) are fine white particles of Nb and the light grey phases (spectrum 12) are the residuals of the Nb-Ti filaments. These phases are the consequences of the diffusion processes that took place during the heating over several seconds.

Fig. 8.13 shows the results of BSE measurements for different samples heated by the capacitive discharge. The peak temperatures are indicated. Edges of two Nb-Ti filaments with the niobium barrier (white) and the copper matrix between the filaments are visible on the reference sample. In the filaments, dark ribbons of α -Ti precipitates with a thickness of a few nm and a length in the range of 100 nm embedded in a lighter matrix of Nb-Ti grains are visible. In the picture obtained for peak temperature of 833 K and 916 K, the dark ribbons become less visible indicating a variation of the microstructure inside the filaments. In the samples heated to peak temperature of 978 K, formations of what is suspected to be Cu-Ti inter-metallic compounds (dark grey) at the interface between the filament and the copper matrix - indicated by black arrows in the figure - is visible. Small islands of dark features (~ 50 nm to ~ 100 nm large) which are presumably made of Ti have developed along the filament boundary - indicated by blue arrows in the figure. At a peak temperature of 1068 K, the microstructure inside the filament has disappeared, Cu-Ti compounds have developed more around

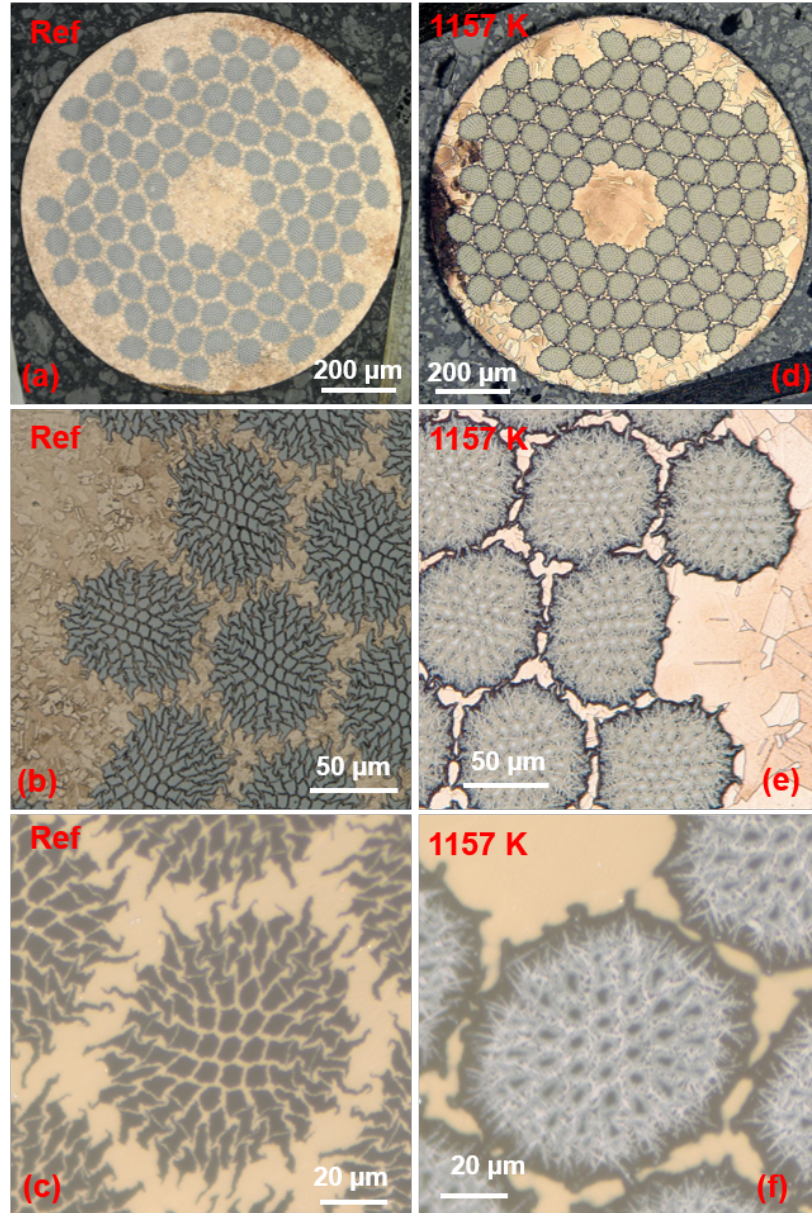
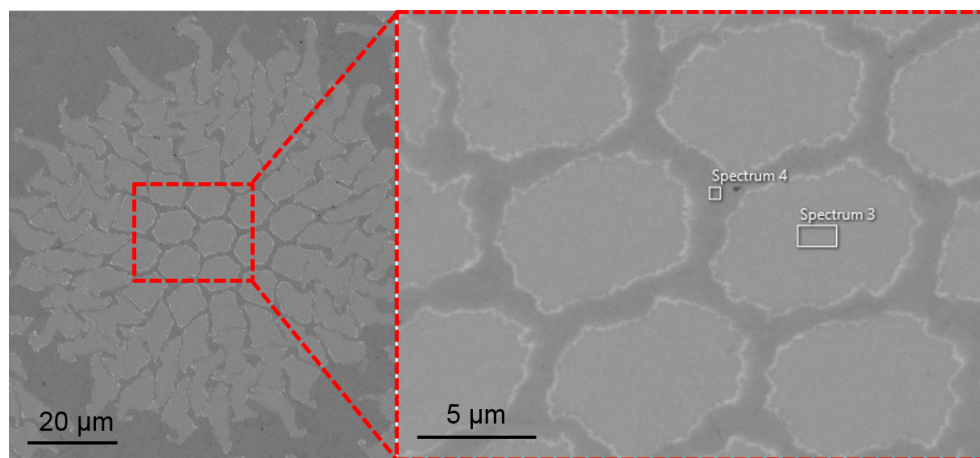


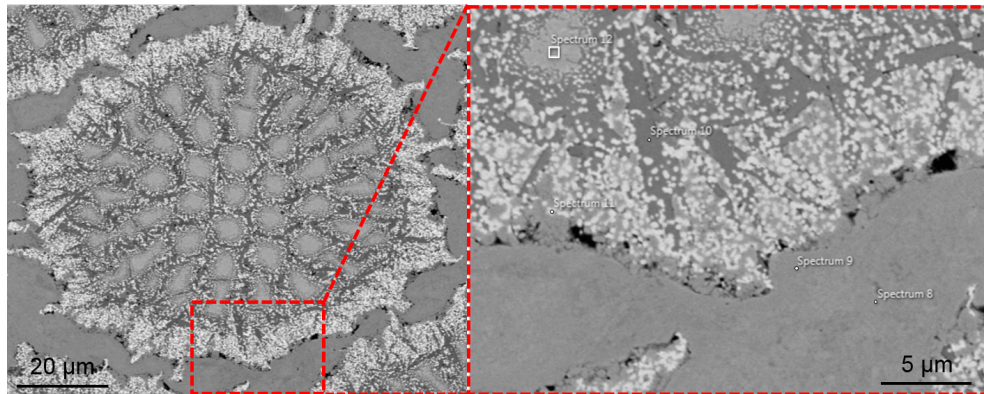
Figure 8.10: Pictures obtained with optical microscope of the Nb-Ti reference sample (a-b-c) and the sample heated by capacitive discharge to a peak temperature of 1157 K (d-e-f). The samples were polished and etched. (a) Cross section of the reference sample, in grey the groups of filaments and in orange the copper matrix. (b) Zoom on several groups of filaments of the reference sample, the single filaments and the copper grains are visible. (c) Zoom on one group of filaments of the reference sample view with polarized light. (d) Cross section of the heated sample. Part of the copper matrix was oxidized (black). (e) Zoom on several groups of filaments of the heated sample, one can see that the filaments have merged and the copper grains are larger than in the reference sample. (f) Zoom on one group of filaments of the heated sample view with polarized light. Different phases are visible in the merged filaments: fine particles of Nb (white), Cu-Ti inter-metallic compound (light grey) and residuals of the Nb-Ti filaments (dark grey).

8. CRITICAL CURRENT DENSITY DEGRADATION RESULTS AND ANALYSIS



	Element weight fraction (%)		
	Nb	Ti	Cu
Spectrum 3	53.0±0.4	47.0±0.4	-
Spectrum 4	-	-	100±0.2

Figure 8.11: Composition analysis of the different phases present in the Nb-Ti reference sample. The pictures were obtained with BSE. The sample was polished before the measurement. A group of filaments (left) and a zoom is shown (right). Lighter phases appear in darker grey and heavier phases in lighter grey. The zones in which the EDX analysis was performed are indicated. The results of the EDX analysis performed in several zone of the samples are presented in the table below the pictures.



	Element weight fraction (%)		
	Nb	Ti	Cu
Spectrum 8	-	-	100.0
Spectrum 9	-	-	100.0
Spectrum 10	4.7±0.3	32.6±0.3	62.7±0.4
Spectrum 11	77.3±0.4	6.6±0.3	16±0.3
Spectrum 12	49.1±0.4	41.2±0.4	9.7±0.2

Figure 8.12: Composition analysis of the different phases present in the Nb-Ti sample heated by capacitive discharge to a peak temperature of 1157 K. The sample was polished before the measurement. The pictures were obtained with BSE and show a group of filaments (left) and a zoom of the indicated region (right). Lighter phases appear in darker grey and heavier phases in lighter grey. The zones in which the EDX analysis were performed are indicated. The results of the EDX analysis performed in several zone of the sample are presented in the table below the pictures.

8. CRITICAL CURRENT DENSITY DEGRADATION RESULTS AND ANALYSIS

the filaments. At locations where the inter-filament distance is small, filament merging can be observed.

8.1.3 Discussion

No degradation of ΔM and, thus, of J_c of Nb-Ti was measured for samples heated by capacitive discharge ($t_{1/2} \sim 6$ s) up to peak temperatures of 651 K and by interaction with a single proton beam pulse ($t_{1/2} \sim 84$ ms) up to peak temperatures of 879 K.

The degradation of J_c increases with exposure time which suggests that the main degradation mechanisms are diffusion processes. Diffusion processes in Nb-Ti are exponentially dependant to temperature [117], thus, even a small temperature differences can have a large impact on the degradation of Nb-Ti. For instance in the beam experiment, at peak temperature of 879 K no degradation has been observed while at a peak temperature of 925 K, less than 50 K more, the J_c at 5 T and 2 K was reduced by about 30% (see Fig. 8.9(b)).

In the second long heating (capacitive discharge) case, two main degradation mechanisms could be identified. For peak temperatures from 833 K to 916 K, a modification of the pinning behaviour and a change of the filaments microstructure were observed. Both are consistent with a size variation of the α -Ti precipitates inside the filaments. For higher peak temperatures, a decrease of H_{c20} and the formation of Cu-Ti inter-metallic compounds were observed, which can be explained by the diffusion of Ti outside the filament leading to a reduction of Ti inside the filament. In the most extreme case which was measured (1157 K) the diffusion process lead to filament merging. The effective filament diameter d_f was modified, which agrees well with the observed increase of ΔM at low external magnetic fields.

In the millisecond long heating (beam impact) case, no decrease of H_{c20} but a decrease of the maximum of F_p and its shift toward lower b was observed for peak temperatures above 925 K. A variation of the α -Ti precipitate size could explained such behaviour.

8.2 Nb₃Sn results and discussion

8.2.1 Magnetization measurement results

The hysteresis width of the magnetization per unit volume, ΔM , as function of external magnetic field measured at 2 K, 4 K, 10 K and 15 K on the Nb₃Sn strands with a diameter of 0.85 mm after heating due to a capacitive discharge is shown in Fig. 8.14. At 15 K, the critical field H_{c2} of the samples is between 3 T and 5 T, within the

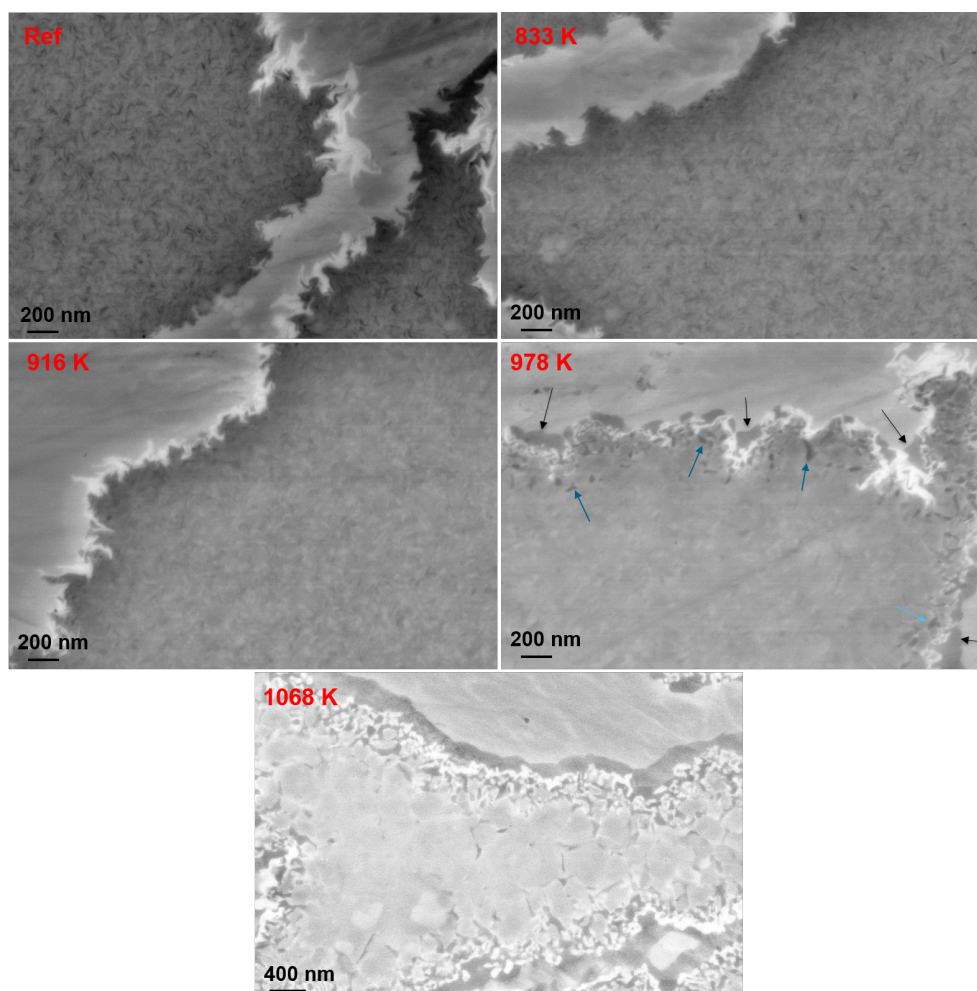


Figure 8.13: Picture obtained with SEM BSE of the edge of Nb-Ti filaments in samples heated by capacitive discharge to several peak temperatures. The lighter phases appear dark and the heavier light. Filament edges with the Nb diffusion barrier and the inter filament copper matrix is visible in the reference sample. A microstructure inside the Nb-Ti filaments composed of dark ribbon of α -Ti precipitates with few nm thickness and a length in the order of 100 nm is visible. In the samples heated up to 833 K and 916 K, the dark ribbons become less visible. Formation of a compound at the interface between the filament and the copper matrix (black arrows), and of small islands of dark features along the filament boundary are visible in the sample heated up to 978 K. At a peak temperature of 1068 K, the microstructure inside the filament has disappeared, the compound at the interface between filaments and copper matrix has developed further such that at location where the inter-filament distance is small, filament merging can be observed.

8. CRITICAL CURRENT DENSITY DEGRADATION RESULTS AND ANALYSIS

measurement range. At 2 K, 4 K and 10 K, ΔM of the reference sample and of the sample heated up to 823 K overlap. The ΔM of two samples can only be distinguished at 15 K for an applied field above 2 T, with a maximum difference below 10%. Thus, the sample heated up to 823 K is considered not degraded. On the other hand the samples heated to peak temperatures above 823 K exhibit a degradation of ΔM at all measured temperatures. Fig. 8.15 shows the ΔM measured at 2 K, 4 K, 10 K and 15 K on the Nb₃Sn strands after heating due to the interaction with a proton beam. Two types of strands were exposed to the beam: strands with a diameter of 0.85 mm are indicated by round markers and strands with a diameter of 0.7 mm are indicated by crosses. At 2 K and 4 K, degradation of ΔM is observed on the 0.85 mm strand heated to temperature of 1026 K and on the 0.7 mm strands to temperature above 677 K. At 10 K and 15 K, degradation is observed above 700 K for the 0.85 mm strands and above 677 K for the 0.7 mm strands.

As for the analysis of the Nb-Ti strands, the pinning force density F_p was derived from the ΔM measurements using equations 5.1 and 5.6. H_{c2} of each strand was obtained from the F_p scaling law (see equation 5.2) according to the Kramer model [68], with p fixed to 0.5 and q to 2. The pinning force density F_p at 2 K, 4 K, 10 K and 15 K as a function of the reduced field $b=H/H_{c2}$ for the samples heated by capacitive discharge is shown in Fig. 8.16 and for the samples heated by interaction with beam in Fig. 8.17. At 15 K, it can be seen that F_p goes to zero at the critical field ($b=1$) for all samples. A reduction of the magnitude of F_p is observed with increasing peak temperature but its maximum stays for all samples around $b=0.2$.

In Fig. 8.18 (a) the critical field H_{c2} , obtained from the F_p scaling law, as a function of temperature for the strands heated by capacitive discharge is shown. The dashed lines correspond to the critical field scaling law (equation 5.3) fitted to the H_{c2} excluding 2 K values. The H_{c2} values at 2 K were excluded, as they are too high to be physical, for instance the $\mu_0 H_{c2}$ at 2 K of the reference sample is about 38 T which is higher than the $\mu_0 H_{c20}$ of Nb₃Sn (29.5 T [80]). Fig. 8.18 (b) shows H_{c20} and T_{c0} obtained from the critical field scaling law as function of the strand peak temperature. A reduction of the H_{c2} and H_{c20} is observed on samples heated to peak temperature above 823 K. $\mu_0 H_{c20}$ drops from about 29.5 T for the reference sample down to 24.8 T for the sample heated up to 1264 K. A small decrease of T_{c0} is observed, from 16.6 K (reference samples) down to 16.2 K for the sample heated up to 1264 K.

The critical field H_{c2} as function of temperature for the strands impacted by beam is shown in Fig. 8.19 (a). As for the capacitive discharge case, the dashed line are the critical field scaling law fitted to the H_{c2} excluding the 2 K values. The H_{c20} and T_{c0} of the strands are shown as function of the strand peak temperature in Fig. 8.19 (b). The

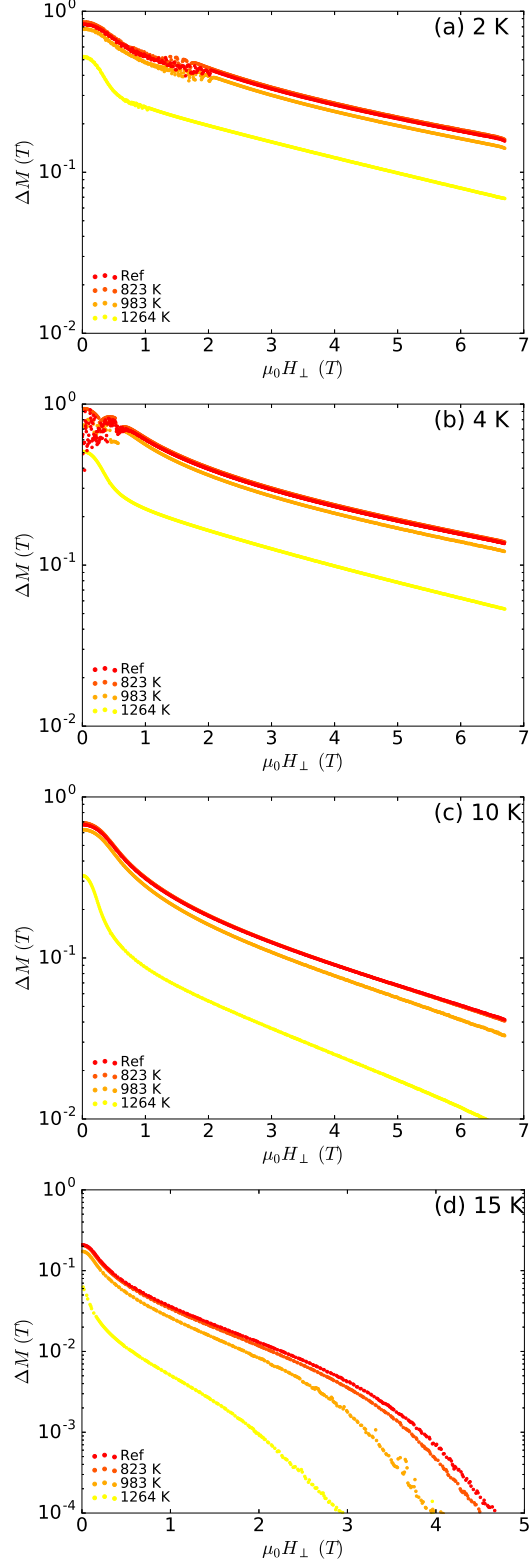


Figure 8.14: Hysteresis width of the magnetization per unit volume, ΔM , of Nb₃Sn strands as a function of the external magnetic field H_{\perp} up to $\mu_0 H_{\perp} = 7$ T after heating due to a capacitive discharge ($t_{1/2} = 6$ s) measured at 2 K (a), 4 K (b), 10 K (c) and 15 K (d).

8. CRITICAL CURRENT DENSITY DEGRADATION RESULTS AND ANALYSIS

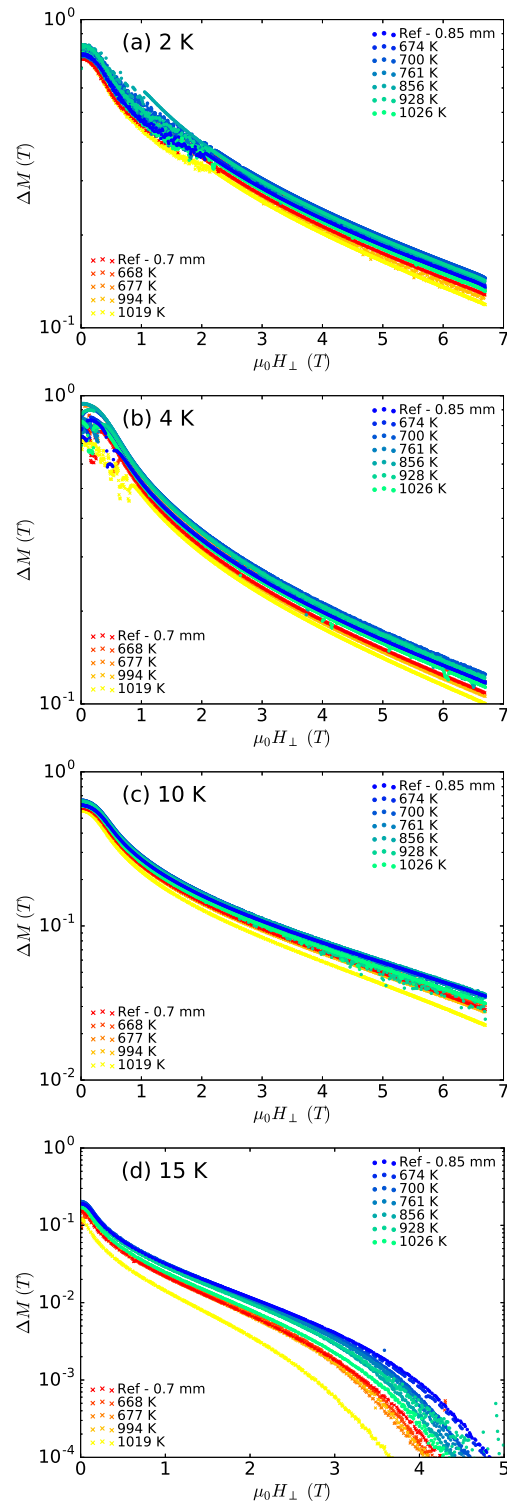


Figure 8.15: Hysteresis width of the magnetization per unit volume, ΔM , of Nb₃Sn strands as a function of the external magnetic field H_{\perp} up to $\mu_0 H_{\perp} = 7$ T after heating due to interaction with a proton beam ($t_{1/2} = 84$ ms) measured at 2 K (a), 4 K (b), 10 K (c) and 15 K (d). Strands with a diameter of 0.85 mm are indicated by round markers and strands with a diameter of 0.7 mm by crosses.

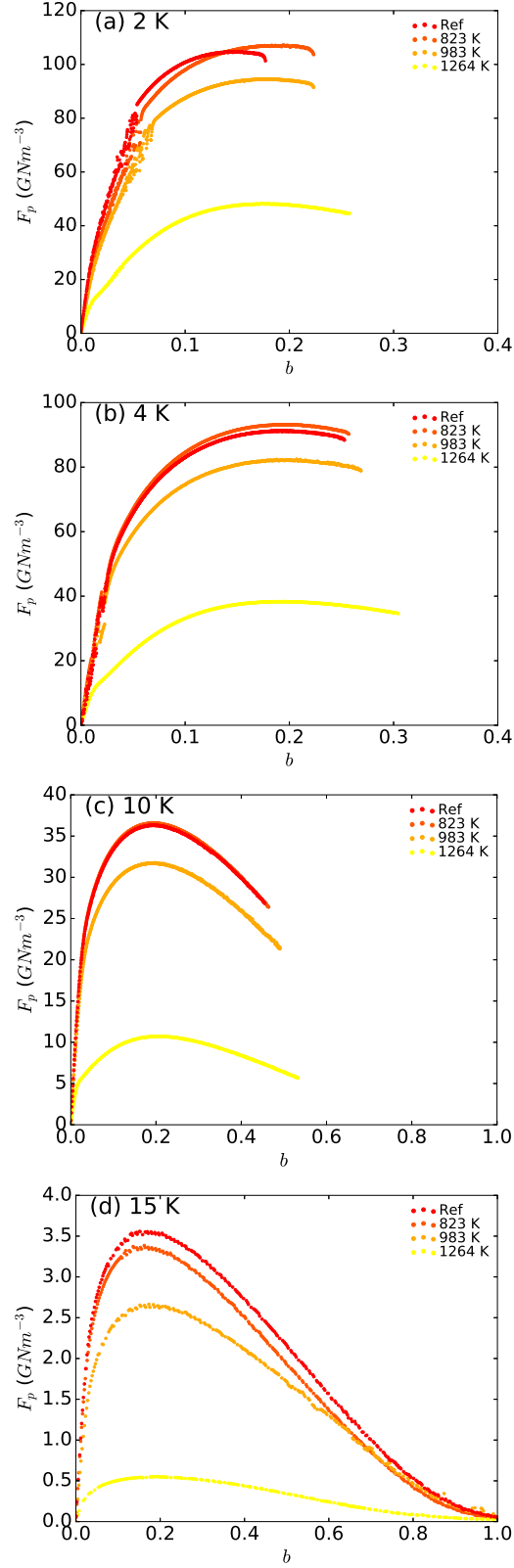


Figure 8.16: Pinning force density F_p of Nb₃Sn strands vs. reduced field b after heating due to a capacitive discharge $t_{1/2}=6$ s measured at 2 K (a), 4 K (b), 10 K (c) and 15 K (d).

8. CRITICAL CURRENT DENSITY DEGRADATION RESULTS AND ANALYSIS

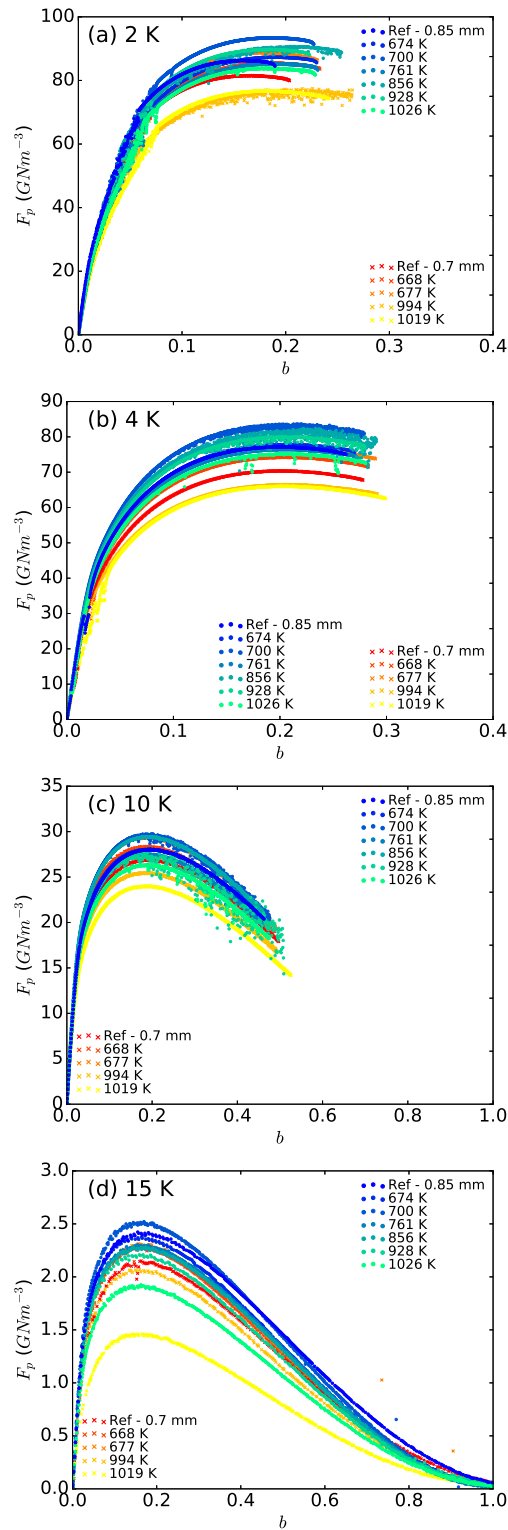
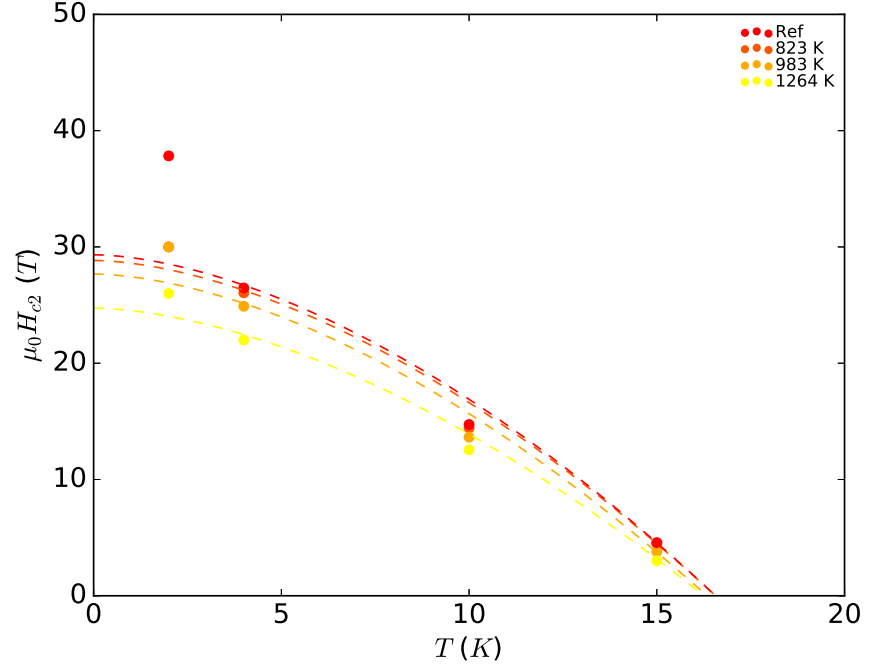
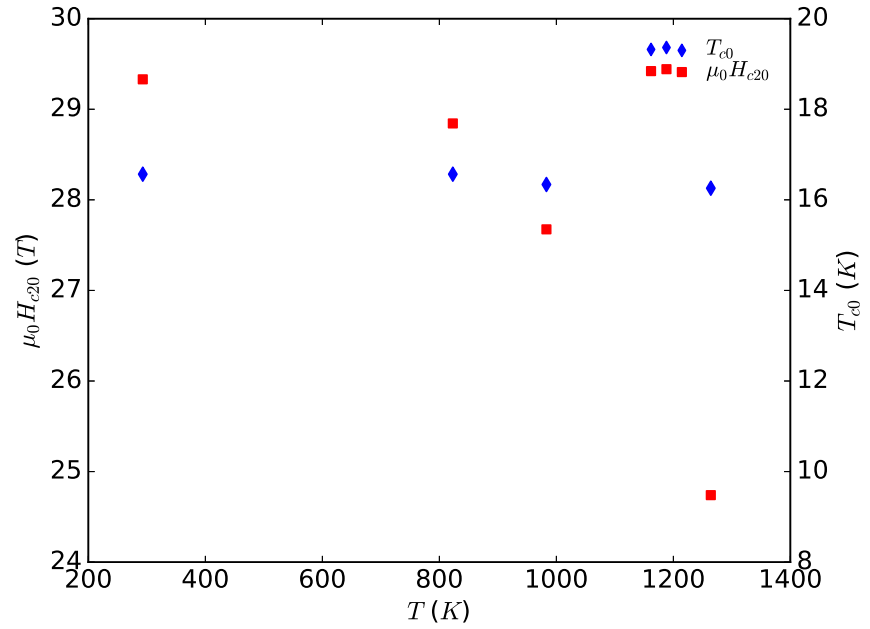


Figure 8.17: Pinning force density F_p of Nb_3Sn strands vs. reduced field b after heating due to interaction with a proton beam $t_{1/2}=84$ ms measured at 2 K (a), 4 K (b) and at 10 K (c) and 15 K (d). Strands with a diameter of 0.85 mm are indicated by round markers and with a diameter of 0.7 mm by crosses.



(a)



(b)

Figure 8.18: H_{c2} , H_{c20} and T_{c0} obtained for the Nb₃Sn strands after heating due to capacitive discharge. (a) $\mu_0 H_{c2}$ as a function of the magnetization measurement temperature. The round markers are the H_{c2} obtained from the F_p scaling law, the dashed lines are obtained by fitting the critical field scaling law (equation 5.3) excluding the H_{c2} value at 2 K. (b) $\mu_0 H_{c20}$ and T_{c0} as function of peak temperature reached in the samples obtained from the fitting of equation 5.3 to the H_{c2} values.

8. CRITICAL CURRENT DENSITY DEGRADATION RESULTS AND ANALYSIS

cross and round markers indicate the T_{c0} and H_{c20} of the 0.7 mm diameter strands and the diamond and square markers of the 0.85 mm diameter strands. T_{c0} stays relatively constant at $\sim 16.6 \pm 0.2$ K for all 0.7 mm diameter strands and at $\sim 16.8 \pm 0.2$ K for 0.85 mm diameter strands. H_{c20} exhibits a decreasing trend with increasing peak temperature. The $\mu_0 H_{c20}$ of the 0.85 mm strands drops from 28.3 T for the reference sample down to 26.7 T for the samples heated up to 1026 K.

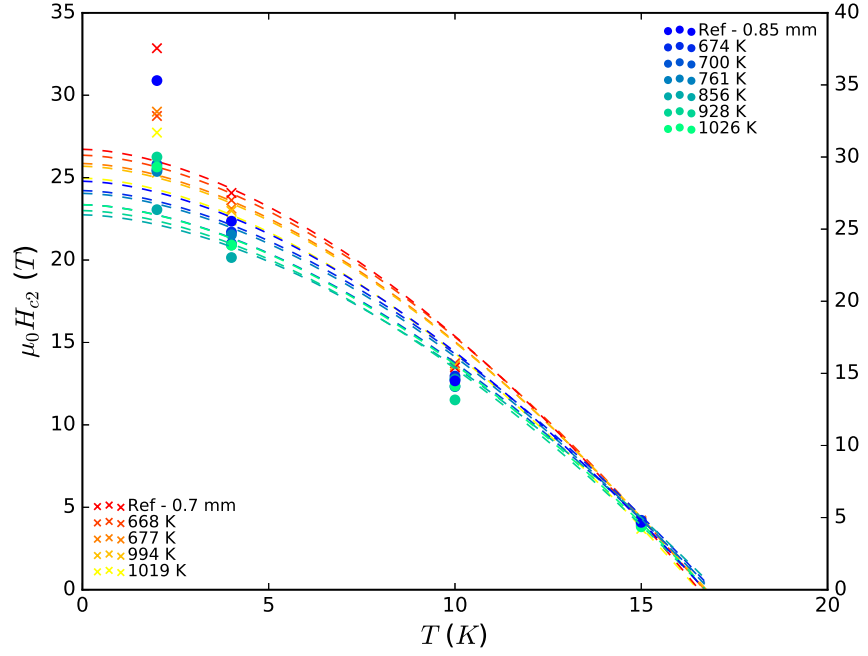
The relative change of magnetization of Nb₃Sn strands as function of the peak temperature reached due to the capacitive discharge and the beam impact are compared in Fig. 8.20 and Fig. 8.21. Fig. 8.20 shows the measurement at 2 K and 4 K, with an applied field of 3 T and 5 T and and Fig. 8.21 at 10 K with an applied field of 3 T and 5 T and at 15 K with an applied field of 1 T and 2 T. At 2 K and 4 K, the samples heated by capacitive discharge show a degradation up to 60%, while the degradation of the samples heated by beam impact is below 10%. Some sample shows even an improvement up to 10% after beam impact. At 10 K and 15 K, the relative reduction of ΔM is higher. At 15 K with an applied field of 2 T, the ΔM of the strands heated to 1264 K by capacitive discharge is degraded by more than 90%, while the beam impacted strands heated up to 1019 K is degraded by more than 40%. It can be observed at all measured temperature and applied field that Nb₃Sn strands heated to similar temperatures have a comparable relative degradation of ΔM for both exposure time, $t_{1/2}=6$ s and $t_{1/2}=84$ ms. For instance, an exposure to a peak temperature of about 1000 K due to capacitive discharge and due to interaction with a proton beam lead to a ΔM degradation of about 30% at 1 T and 15 K.

8.2.2 Microscopic analysis results

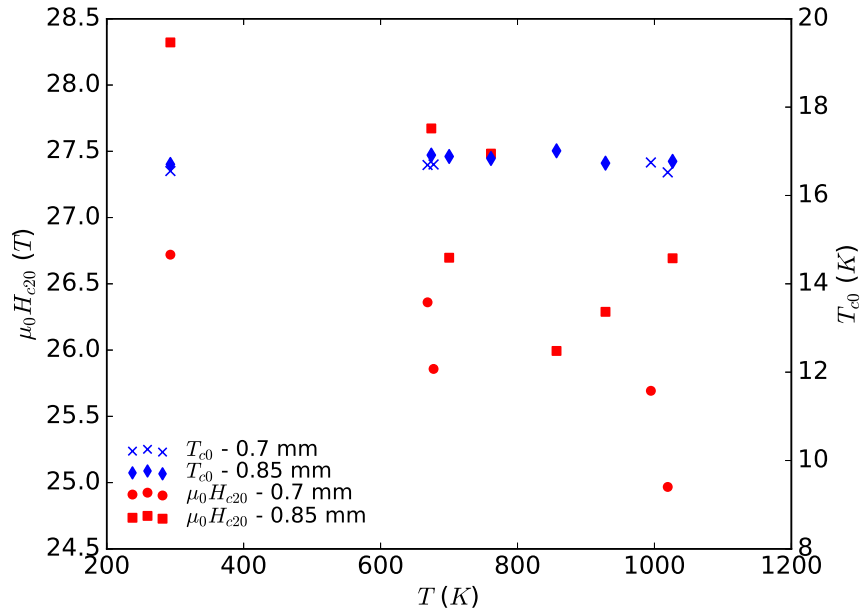
Composition and grain size measurements were performed via microscopic analysis on the Nb₃Sn reference sample and the samples heated by capacitive discharge to 1264 K.

As shown on both pictures in Fig. 8.22, Nb₃Sn filaments are hollow cylinders surrounded by a Nb diffusion barrier with a thickness between 1 and 3 μm (indicated by a blue arrow) with inside the cylinder mainly Cu, Sn (dark grey) and void (black). The wall of the cylinder is composed of Nb₃Sn grains with few patches of copper in between (indicated by a red arrow).

The composition of the Nb barrier and of the Nb₃Sn hollow cylinder were measured on both polished reference and heated sample. The composition of the Nb₃Sn hollow cylinder, expressed in atomic percent (at.%), was measured at mid-thickness of the cylinder wall as indicated by the red square in Fig. 8.22, in order to avoid artifacts induced by phases outside the hollow cylinder in the EDX analysis. The composition



(a)



(b)

Figure 8.19: H_{c2} , H_{c20} and T_{c0} obtained for the Nb₃Sn strands after heating due to interaction with a proton beam. (a) $\mu_0 H_{c2}$ as a function of the magnetization measurement temperature. The round and cross markers are the H_{c2} obtained from the F_p scaling law fitting of the 0.85 mm diameter and 0.7 mm diameter strands. The dashed lines are obtained by fitting the critical field scaling law (equation 5.3) excluding the H_{c2} value at 2 K. (b) $\mu_0 H_{c20}$ and T_{c0} as function of peak temperature reached in the samples obtained from the fitting of equation 5.3 to the H_{c2} values.

8. CRITICAL CURRENT DENSITY DEGRADATION RESULTS AND ANALYSIS

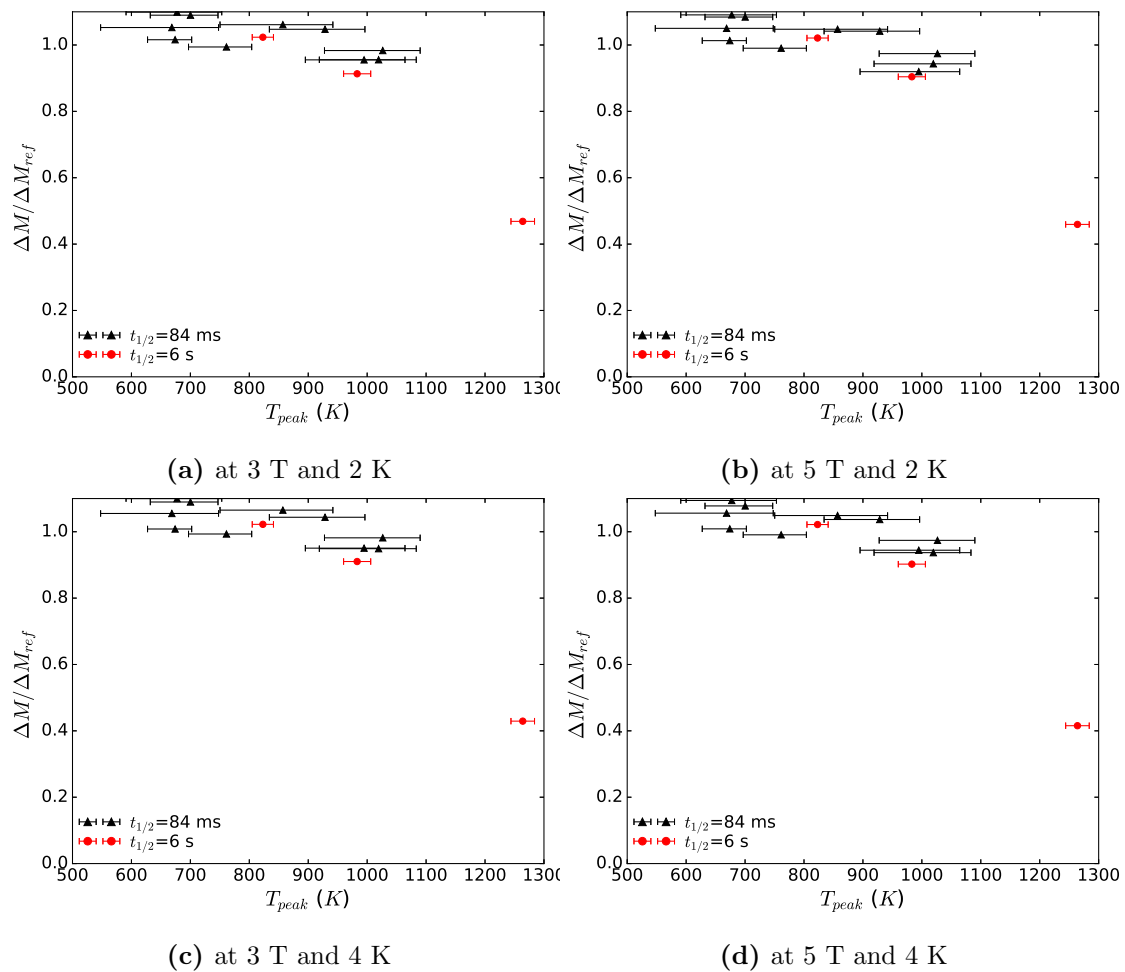


Figure 8.20: Relative change of magnetization vs. peak temperature reached in Nb₃Sn strands during different timescales measured at 2 K and 4 K with an applied field of 3 T and 5 T.

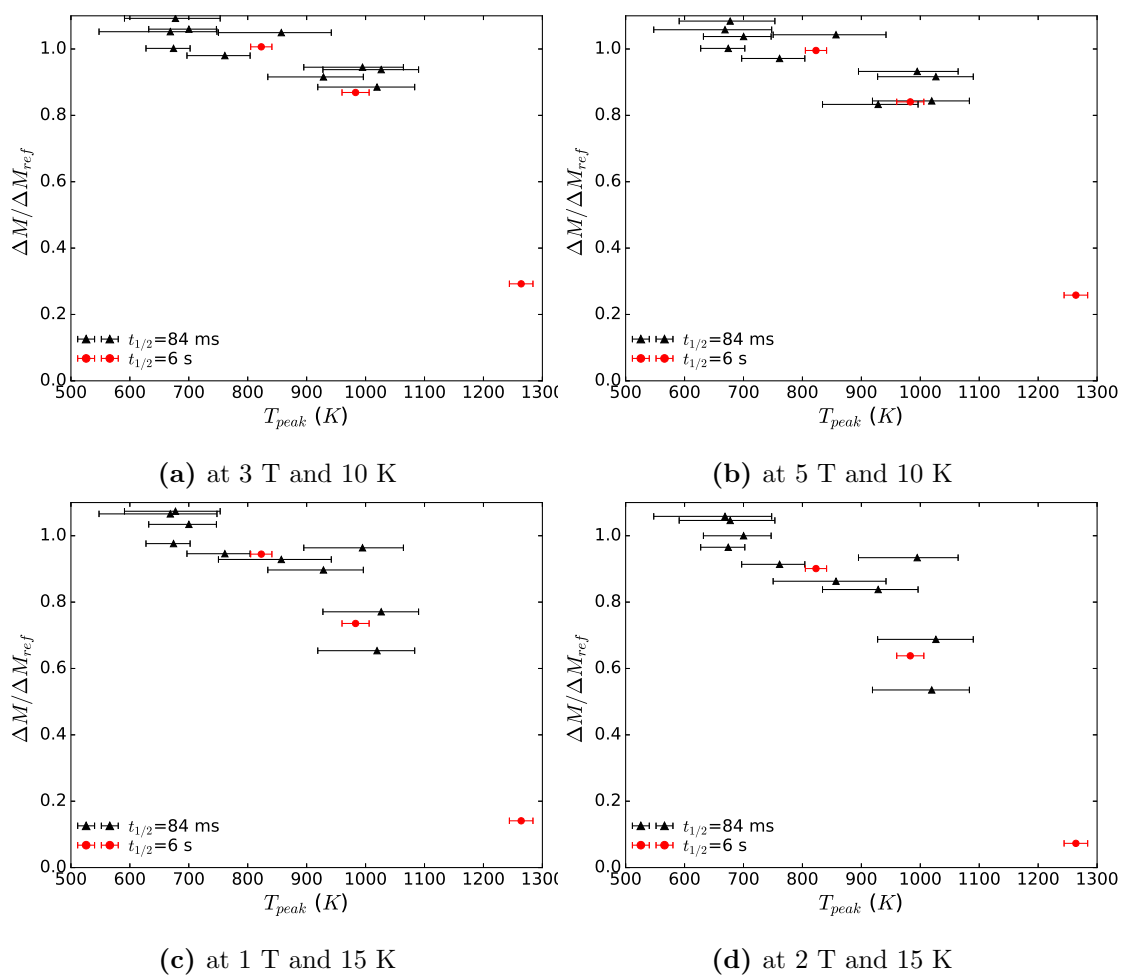


Figure 8.21: Relative change of magnetization vs. peak temperature reached in Nb₃Sn strands during different timescales measured at 10 K with an applied field of 3 T and 5 T and at 15 K with an applied field of 1 T and 2 T.

8. CRITICAL CURRENT DENSITY DEGRADATION RESULTS AND ANALYSIS

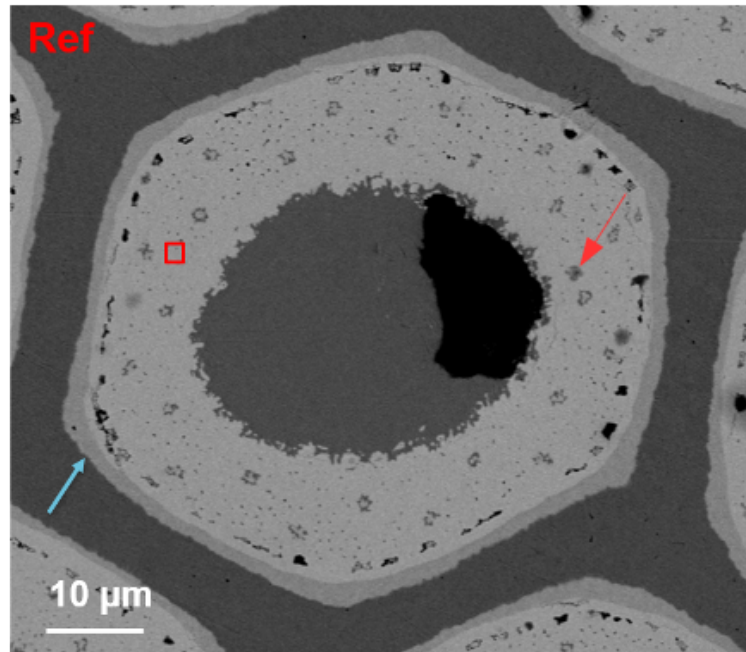


Figure 8.22: Picture of a Nb₃Sn filament of the reference sample obtained via SEM BSE. The Nb₃Sn superconductor hollow cylinder is visible in grey surrounded by the few μm thick Nb diffusion barrier indicated by the blue arrow. Few patches of copper are visible within the cylinder wall indicated by the red arrow. Inside the filament is a mixture Cu and Sn (dark grey) and a void (black). The red square located at mid-thickness of the superconductor cylinder wall illustrate on which zone of the filaments the EDX analysis were performed.

results are reported in Table 8.1. In the reference sample, the Sn content is 24.7 at.%, which is within the optimum range of 24.5 at.% to 25 at.% [81, 83, 118]. The Sn content in the heated sample is slightly lower (24.2 at.%), however the difference between the two samples is within the measurement error of about 1 at.%. In both samples, the diffusion barrier is composed of 100 % of Nb. From the EDX analysis, no composition change above 1 at.% of the Nb₃Sn filaments can be observed.

The grain sizes were measured on broken samples via SEM BSE. Fig. 8.23 shows SEM pictures of the reference and the heated samples at different locations in the hollow cylinder of the filament: the inner part, the mid-thickness and the outer part close to the Nb barrier. The measured grain size are given in Table. 8.2. For all three locations, a growth of the grain was observed between the reference and the heated samples however the measured growth is within the standard deviation of the measurements.

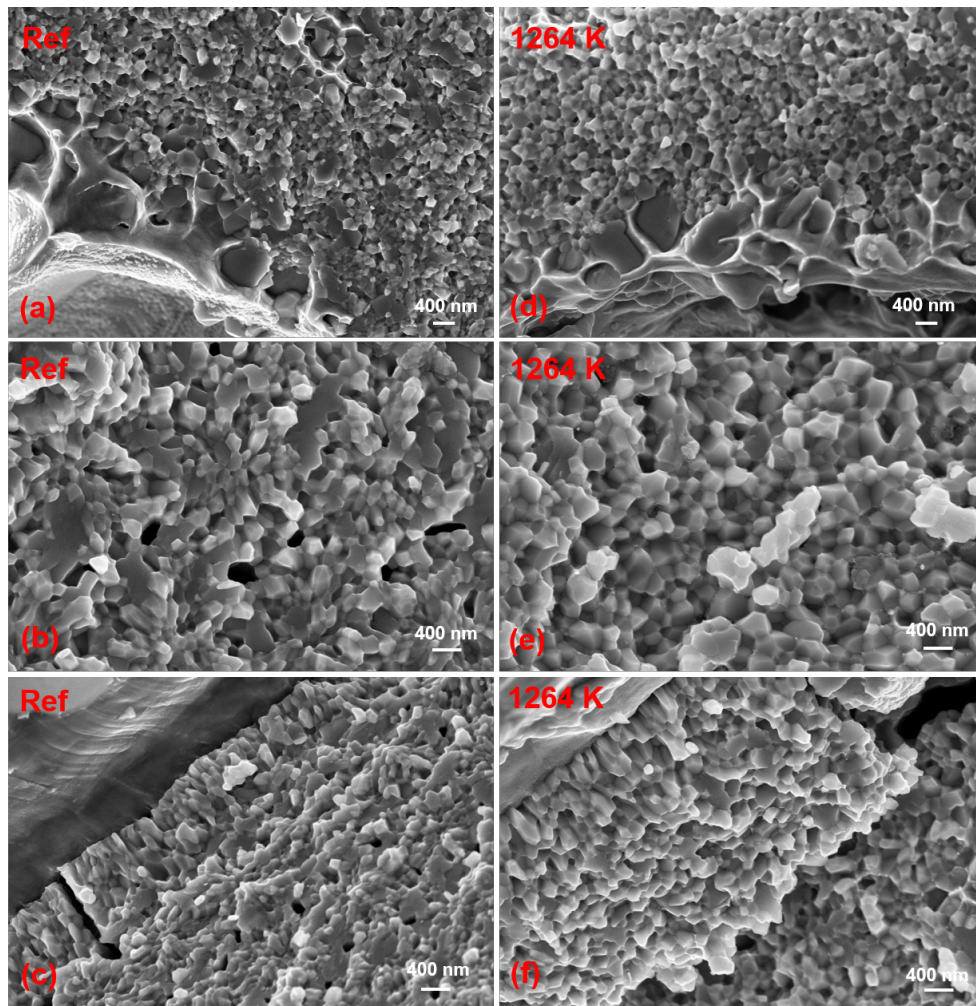


Figure 8.23: Pictures of the reference sample (a to c) and the sample heated by capacitive discharge to 1264 K (d to f), at different locations of the hollow cylinder of the filament, obtained via SEM BSE. (a) and (d) are from the inner part of the wall of the cylindrical filament, (b) and (e) are from the mid-thickness of the wall and (c) and (f) are from the outer part of the wall closed to the Nb barrier. The samples were broken before observation. Grain sizes were measured from these pictures (see Table 8.2).

8. CRITICAL CURRENT DENSITY DEGRADATION RESULTS AND ANALYSIS

Table 8.1: Composition in atomic percent (at.%) of the Nb₃Sn filament measured at mid-thickness of the filament hollow cylinder wall (indicated by the red square in Fig. 8.22) for both reference sample and sample heated by capacitive discharge to 1264 K. The measurement error is estimated to 1 at.%.

	Ref	1264 K
Nb (at.%)	75.3	75.8
Sn (at.%)	24.7	24.2

Table 8.2: Average grain sizes with their standard deviation measured on both reference sample and sample heated by capacitive discharge to 1264 K at different locations in the hollow cylinder of the filament: the inner part, the mid-thickness and the outer part close to the Nb barrier. The grain sizes were obtained from the pictures shown in Fig. 8.23

	Ref	1264 K
Inner part	117±37 nm	158±46 nm
Mid-thickness	141±28 nm	153±38 nm
Outer part	118±44 nm	140±38 nm

8.2.3 Discussion

Degradation of ΔM , equivalent to a degradation of J_c , in Nb₃Sn strands is observed on samples heated by the capacitive discharge ($t_{1/2} \sim 6$ s) to peak temperatures above 823 K (see Fig. 8.14) and on samples exposed to a proton beam pulse ($t_{1/2} \sim 84$ ms) to peak temperatures above 700 K (see Fig. 8.15). At 15 K with an applied field of 2 T, a degradation of the critical current density of $\sim 40\%$ has been measured on strands heated by capacitive discharge to peak temperature of 983 K and a 10% degradation has been measured on strands heated by interaction with the proton beam to peak temperature of 761 K.

A reduction of the maximum of the pinning force density F_p is observed in both experiments with increasing peak temperature (see Fig. 8.16 and Fig. 8.17). As shown in [81] and [119], the maximum of F_p is proportional to the inverse of the grain size. In the capacitive discharge case, the maximum of F_p measured at 4 K decreases from ~ 90 GN m⁻³ for the reference sample to ~ 35 GN m⁻³ for the sample heated up to 1264 K. This would be equivalent to a grain growth by a factor four. However no such change in grain size could be observed via SEM BSE analysis of the two samples (see Table 8.2 and Fig. 8.23). Grain growth is a time depend process, the longer the sample is exposed to high temperature the more the grains are growing. Therefore if such growth is not observed after a second long heating due to a capacitive discharge, no

grain growth can be expected after a millisecond long heating due to interaction with a proton beam. Thus, grain growth is excluded to be the origin of the degradation.

In both experiments, a degradation of H_{c20} with increasing temperature was observed (see Fig. 8.18 and Fig. 8.19). In the capacitive discharge experiment, H_{c20} decreases from 29.5 T for the reference sample to 24.8 T for the sample heated up to 1264 K. In the proton beam experiment, H_{c20} goes from 28.3 T for the reference strand of 0.85 mm diameter down to 26.7 T for the strand heated up to 1026 K, and from 26.7 T for the reference strand of 0.7 mm diameter down to 25 T for the strand heated up to 1019 K. Two degradation mechanisms could explain such decrease of H_{c20} : variation of Nb-Sn composition and an increase of the strain applied on the Nb₃Sn. As shown in [81, 118], the critical field H_{c20} , temperature T_{c0} and current density J_c are a function of the Nb-Sn composition of the filament (e.g tin content). Exposure of a Nb₃Sn superconductor to a high temperature could induce a diffusion of tin outside the filaments resulting in a drop of the filament tin content and a decrease of H_{c20} . The critical field H_{c20} and J_c are also varying with the strain applied on the Nb₃Sn filaments [81, 105, 120]. To explain the H_{c20} drop between the reference strand and the strand heated up to 1264 K by the capacitive discharge, the filament tin content would have to decrease by about 1 at.% or the strain state of the Nb₃Sn filament would have to increase by 0.2-0.4%. Composition measurements via SEM EDX were performed on the strands heated by capacitive discharge, a reduction of 0.5 at.% tin content was measured (see Table 8.1). However the observed reduction is within the measurement error, therefore, no conclusive result was achieved.

As shown in Fig. 8.20 and Fig. 8.21, similar level of J_c degradation are observed for Nb₃Sn strands heated to comparable temperatures but for different exposure time ($t_{1/2}=6$ s and $t_{1/2}=84$ ms). Variation of tin content is a diffusion processes which is time dependent, the longer the exposure time to high temperature is, the higher is the variation of tin content and the higher is the degradation of J_c . Therefore, tin content variation cannot be the only degradation mechanism of the strands heated by interaction with a proton beam. One of the other possible mechanisms for the J_c degradation in the beam impacted samples is mechanical stress. The high thermal gradients and the very fast temperature rise ($0.6 \mu\text{s}$) in the strands induced by the beam impact can generate quasi-static and dynamic stresses. The maximum thermal gradient induced by beam impact in the strand central part is about 50 K mm^{-1} . This could lead to deformations of the copper matrix resulting in a residual stress on the filaments or even cracks in the superconductor. Further studies are required to identify the origin of the degradation.

8. CRITICAL CURRENT DENSITY DEGRADATION RESULTS AND ANALYSIS

9

Conclusion

Superconducting magnets are essential for many accelerators, in particular for high energy proton machines. The energy in both, beam and magnets, has increased significantly over the past decades, and will further increase. Therefore the protection of superconducting magnets from beam as well as from their own stored energy becomes increasingly important. The design of magnet protection systems is based on the magnets damage limits. If these limits are too conservative, this can have an impact on the cost and the performance of accelerators.

Studies of HL-LHC injection and extraction beam losses have shown that the energy deposition in Nb-Ti superconducting coils can reach 100 J cm^{-3} inducing a peak temperature of about 120 K. With the limited knowledge on beam induced damage to superconducting magnet before this thesis, damage of the superconducting magnets with these type of events could not be excluded.

Therefore in this thesis, for the first time the damage mechanisms and limits of superconducting magnets due to beam impact were experimentally studied. The polyimide insulation and Nb-Ti and Nb₃Sn superconducting strands have been identified as the most critical parts of the magnet. Damage experiments have been performed at room temperature to study the effect of heating over different time scales - hours, several seconds and tens of milliseconds - on the dielectric strength of the polyimide insulation and the critical current density of Nb-Ti and Nb₃Sn superconducting strands.

Following heating over hours a degradation of the dielectric strength of the polyimide insulation was observed above 728 K, due to a chemical decomposition process strongly depending on temperature and length of the exposure. Above 821 K the insulation was completely lost. No degradation was measured for millisecond heating due to beam impact. Nevertheless, a weakening of the insulation at the point of the beam

9. CONCLUSION

impact could be identified peak temperature above 850 K which is equivalent to an energy deposition of 1.9 kJ cm^{-3} .

A first degradation of the critical current density of Nb-Ti strands was observed for peak temperatures above 651 K in case of the heating for a few seconds due to a capacitive discharge. In case of beam impact a change of J_c was only observed for peak temperature above $\sim 900 \text{ K}$ equivalent to 2.2 kJ cm^{-3} . The most probable explanation for the observed degradation are variation of the size and the spacing of the α -Ti precipitates. At temperatures exceeding 833 K with 6 seconds of cooling, a reduction of the upper critical field was measured most likely due to the variation of the Ti content of the filaments caused by diffusion. For samples heated up to a temperature of 1157 K with a second long cooling, filament merging was observed, due to diffusion of the Nb and Ti into the copper matrix.

Degradation of the critical current density and upper critical field in Nb₃Sn strands were observed for peak temperatures above 823 K after heating over few seconds due to a capacitive discharge. Grain growth was excluded as origin of this. Other explanations like the variation of the tin content or increase of the applied strain on the Nb₃Sn need to still be investigated. After heating for tens of milliseconds due to proton beam impact, degradation was observed for temperatures above $\sim 700 \text{ K}$ equivalent to 1.4 kJ cm^{-3} . Heating via beam impact or capacitive discharge to similar peak temperatures induces a comparable critical current density degradation. This is a fundamentally different behaviour than that observed for Nb-Ti strands, indicating, that the degradation due to beam impact is probably dominated by stresses and potentially cracks caused by the fast heating and the high thermal gradients induced by local heating at the position of the beam impact.

These results show that no damage is expected in Nb-Ti superconducting magnets in case of injection and extraction failures in HL-LHC. However the validity of such results need to be confirmed with experiments at liquid helium temperature and on a full scale magnet.

The experimental work done in this thesis has set the bases of the understanding of superconducting magnets damage mechanisms due to beam impact. The studies are still on going. An experiment to irradiate superconductor samples at liquid helium temperature with a proton beam in the CERN HiRadMat facility will be performed during the summer 2018.

Appendix A

Appendix: Technical drawings of the stainless steel moulds

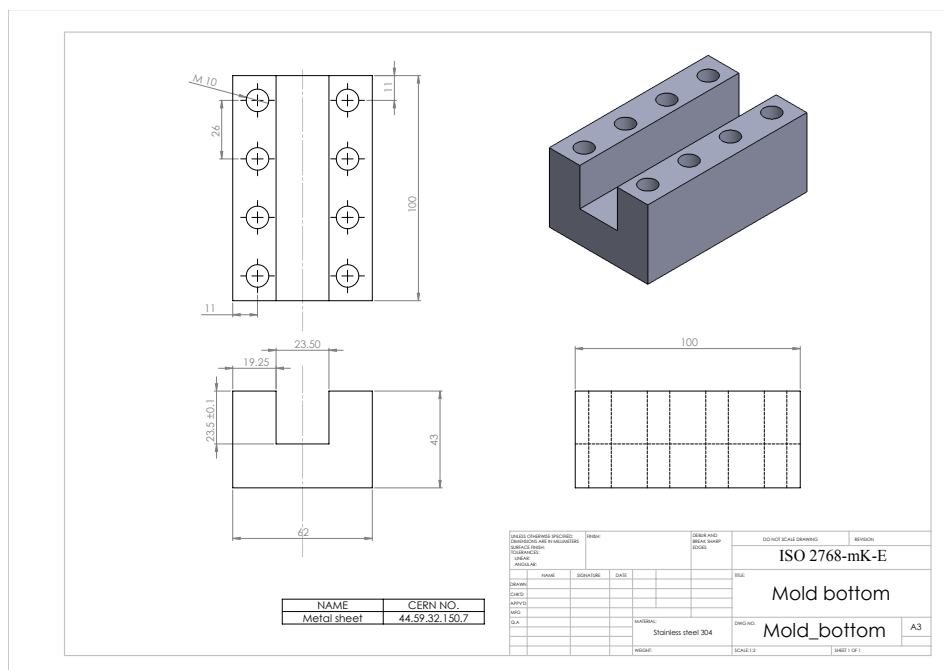


Figure A.1: Technical drawing of the lower part of the mould used in the furnace experiment.

A. APPENDIX: TECHNICAL DRAWINGS OF THE STAINLESS STEEL MOULDS

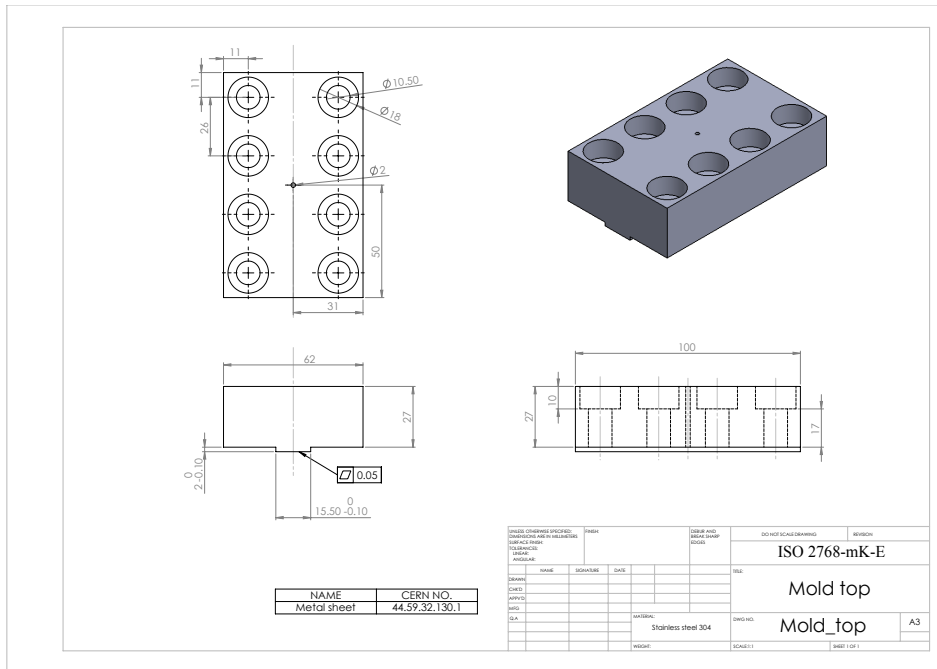


Figure A.2: Technical drawing of the upper part of the mould used in the furnace experiment.

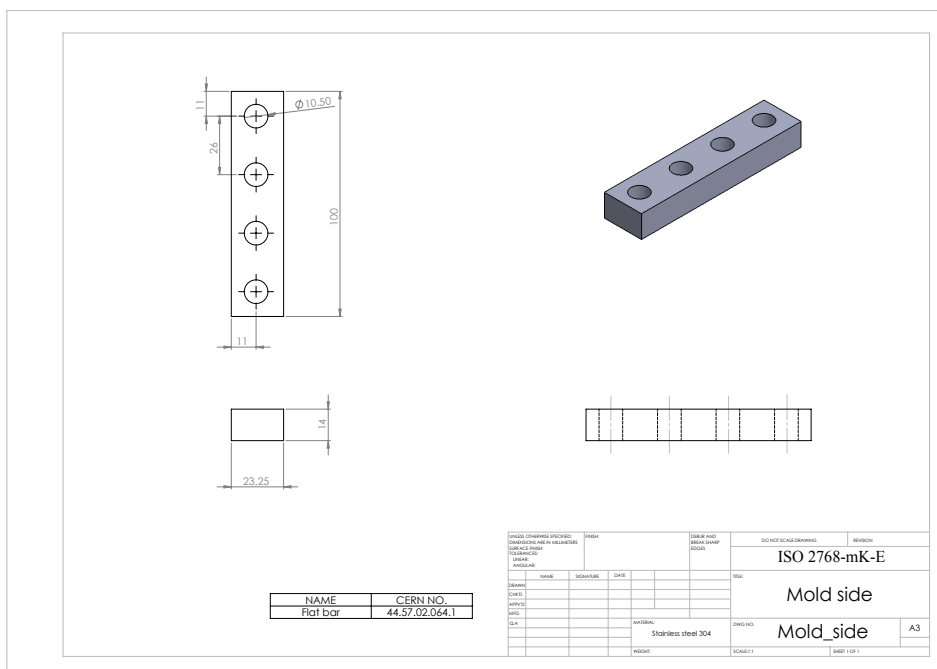


Figure A.3: Technical drawing of the side parts of the mould used in the furnace experiment.

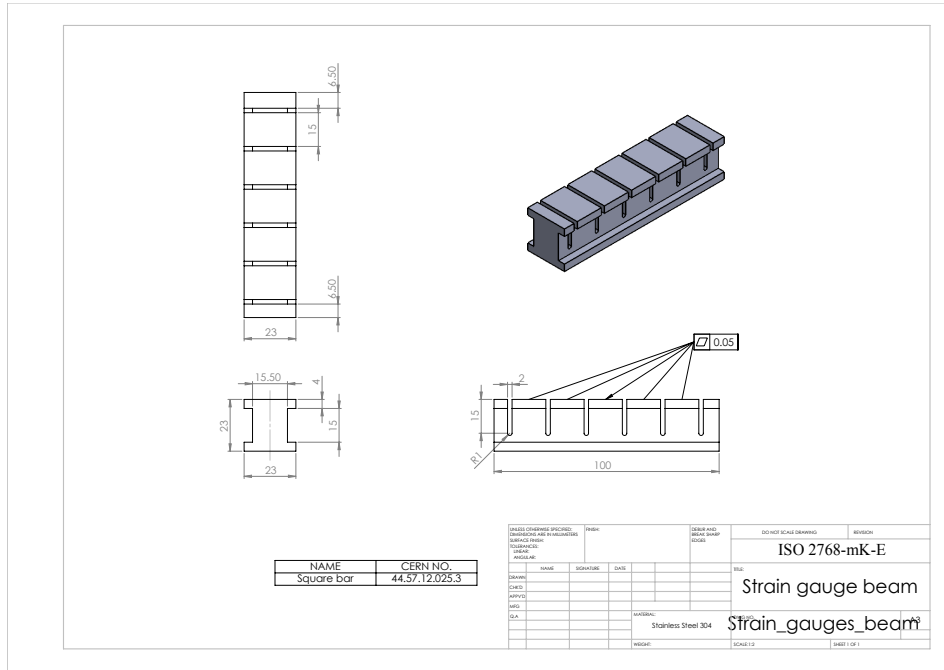


Figure A.4: Technical drawing of the strain gauge beam of the mould used in the furnace experiment.

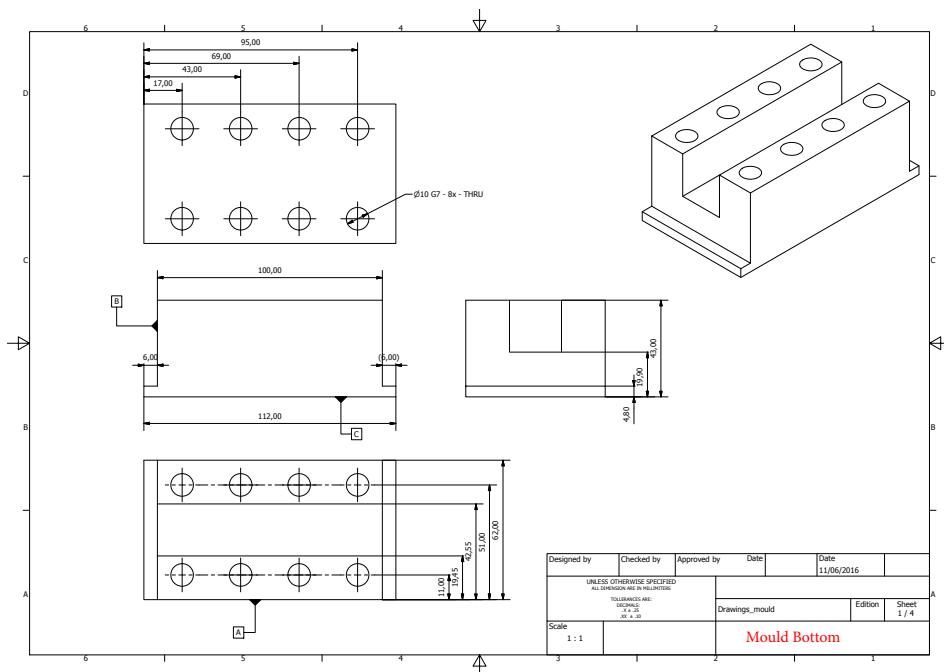


Figure A.5: Technical drawing of the lower part of the mould used in the beam experiment.

A. APPENDIX: TECHNICAL DRAWINGS OF THE STAINLESS STEEL MOULDS

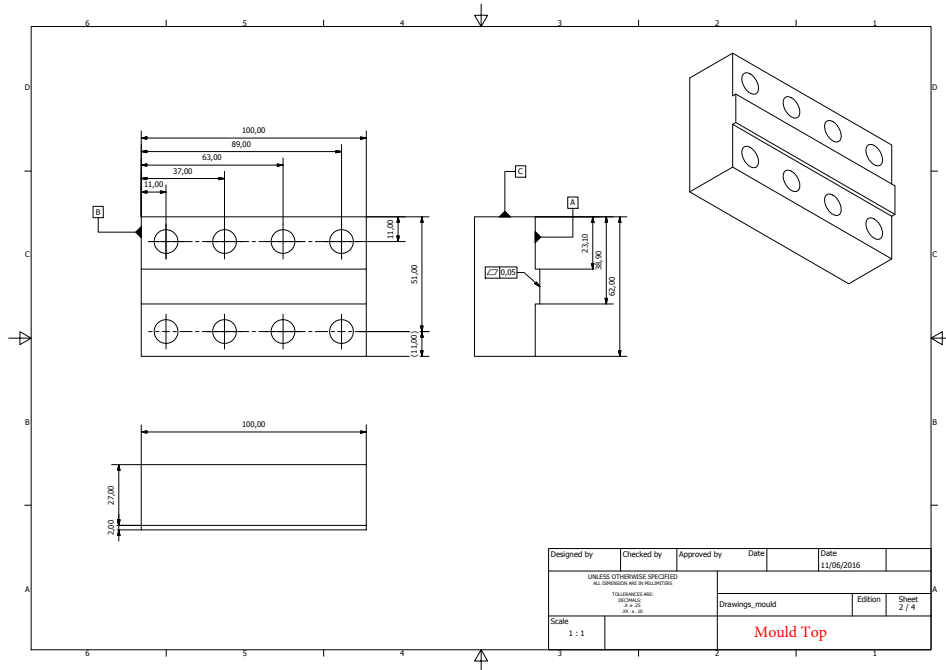


Figure A.6: Technical drawing of the upper part of the mould used in the beam experiment.

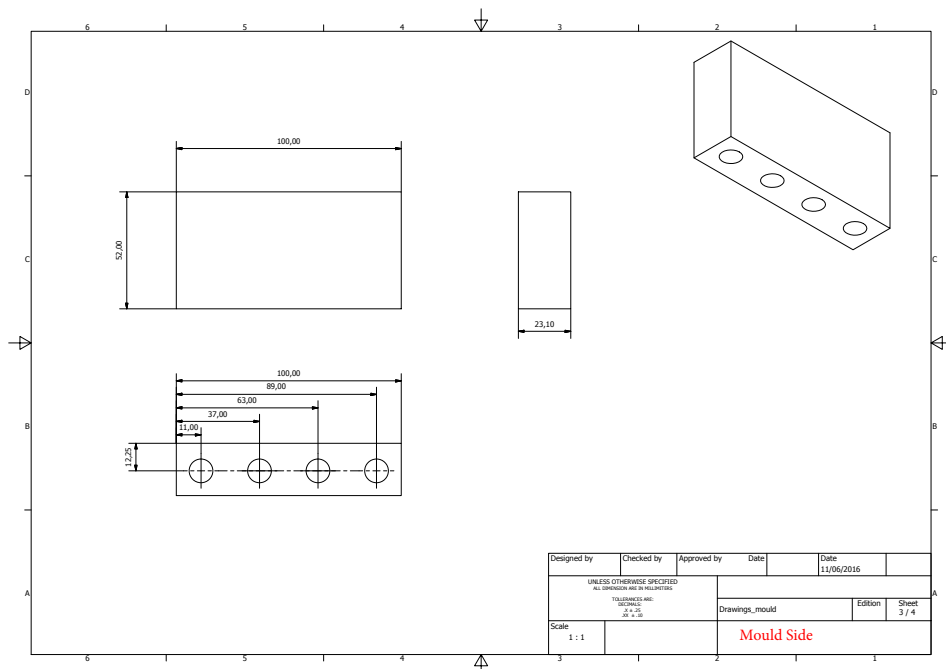


Figure A.7: Technical drawing of the side parts of the mould used in the beam experiment.

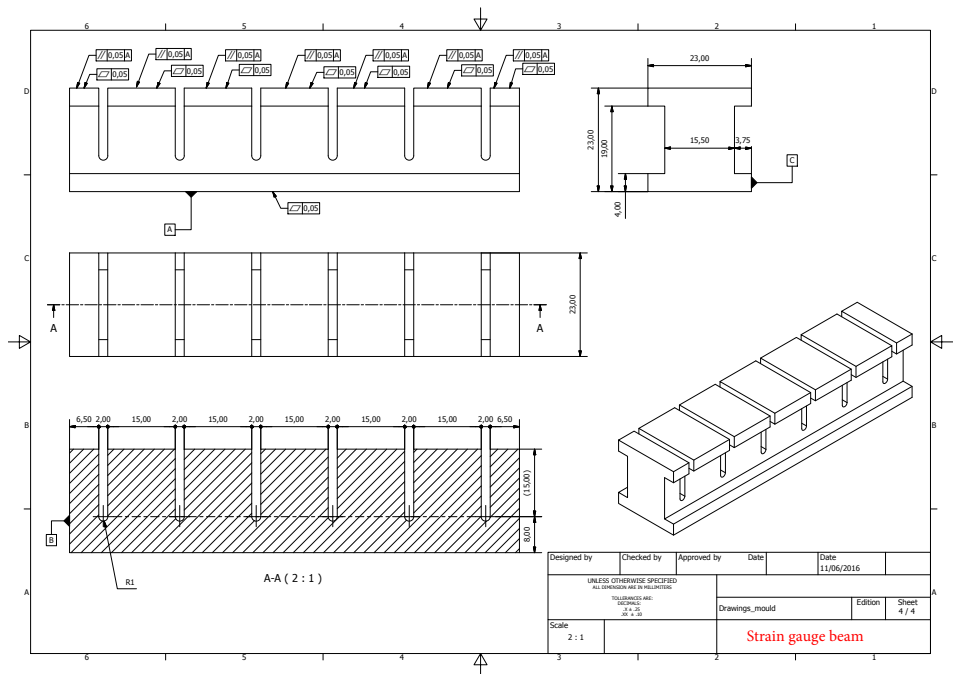


Figure A.8: Technical drawing of the strain gauge beam of the mould used in the beam experiment.

**A. APPENDIX: TECHNICAL DRAWINGS OF THE STAINLESS
STEEL MOULDS**

Appendix B

Appendix: List of the superconducting strands used in the beam experiment

Table B.1: List of the eleven strands of set-A with the beam intensities by which they were impacted. The strands are connected in series with a shunt resistor and a power supply. Each strand set is independent of the other set. All the strands are equipped with voltage taps.

Strand Label	Type	Beam Intensity (10^{11} protons)	Pulse #
U1	Nb-Ti	-	-
U2	Nb-Ti	6	1
U3	Nb-Ti	6	2
U4	Nb-Ti	6	3
U5	Nb-Ti	6	4
U6	Nb-Ti	6	5
U7	Nb-Ti	6	6
U8	Nb-Ti	13	7
U9	Nb-Ti	13	8
U10	Nb-Ti	13	9
U11	Nb-Ti	-	-

B. APPENDIX: LIST OF THE SUPERCONDUCTING STRANDS USED IN THE BEAM EXPERIMENT

Table B.2: List of the twenty three strands of set-B with the beam intensities by which they were impacted.. The strands are connected in series with a shunt resistor and a power supply. Each strand set is independent of the other set. The strands are equipped with voltage tabs except strands L3, L6, L9, L12, L15 and L18. For the six beam pulses with the highest intensity (26×10^{11} protons), additional strands 1.2 mm above and below the targeted strand were installed.

Strand Label	Type	Beam Intensity (10^{11} protons)	Pulse #
L1	Nb-Ti	-	-
L2	Nb ₃ Sn	26	10
L3	Nb ₃ Sn		
L4	Nb ₃ Sn		
L5	Nb ₃ Sn	26	11
L6	Nb ₃ Sn		
L7	Nb ₃ Sn		
L8	Nb ₃ Sn	26	12
L9	Nb ₃ Sn		
L10	Nb ₃ Sn		
L11	Nb-Ti	26	13
L12	Nb-Ti		
L13	Nb-Ti		
L14	Nb-Ti	26	14
L15	Nb-Ti		
L16	Nb-Ti		
L17	Nb-Ti	26	15
L18	Nb-Ti		
L19	Nb-Ti		
L20	Nb ₃ Sn	13	16
L21	Nb ₃ Sn	13	17
L22	Nb ₃ Sn	13	18
L23	Nb-Ti	-	-

Appendix C

Appendix: Energy deposition simulation for the beam experiment

Energy deposition simulations with FLUKA were used to choose pulse intensities and beam size required to reach peak temperatures in the samples between 350 K and 1100 K. Moreover to derive the peak temperatures reached in the sample during the beam experiment from the strand resistance measurements, several assumption had to be made based on the simulations.

The geometry of the experimental set-up was implemented in FLUKA including the samples and the tank. A cross section of the upper-half of the experimental set-up superposed to the energy deposition per proton induced by Gaussian beam with a $1 \sigma_{r.m.s.}$ transverse size of 1 mm is shown in Fig. C.1. The beam comes from the left, enters the tank through its front wall, travels through the three first cable stacks, the plate with the superconducting strand and the three last cable stacks, to finally exit the tank through its back wall. The energy deposition is maximum along the beam axis ($y = 0$) and reaches its peak value in the third cable stacks and slowly decay after. The gap between the last cable stack and the tank back wall allows the particle shower to open, thus reducing its energy deposition in the tank wall.

The peak energy deposition per proton as function of the longitudinal position of the cable stacks, their mould, the single strands and the tank walls is given Fig. C.2. The ratios of the peak energy deposition in the cable stacks over the peak energy deposition in strands $(E_{st}/E_s)_{sim}$ used to calculated the peak temperature reached in the cable stacks during the beam experiment were derived from these simulation results. The

C. APPENDIX: ENERGY DEPOSITION SIMULATION FOR THE BEAM EXPERIMENT

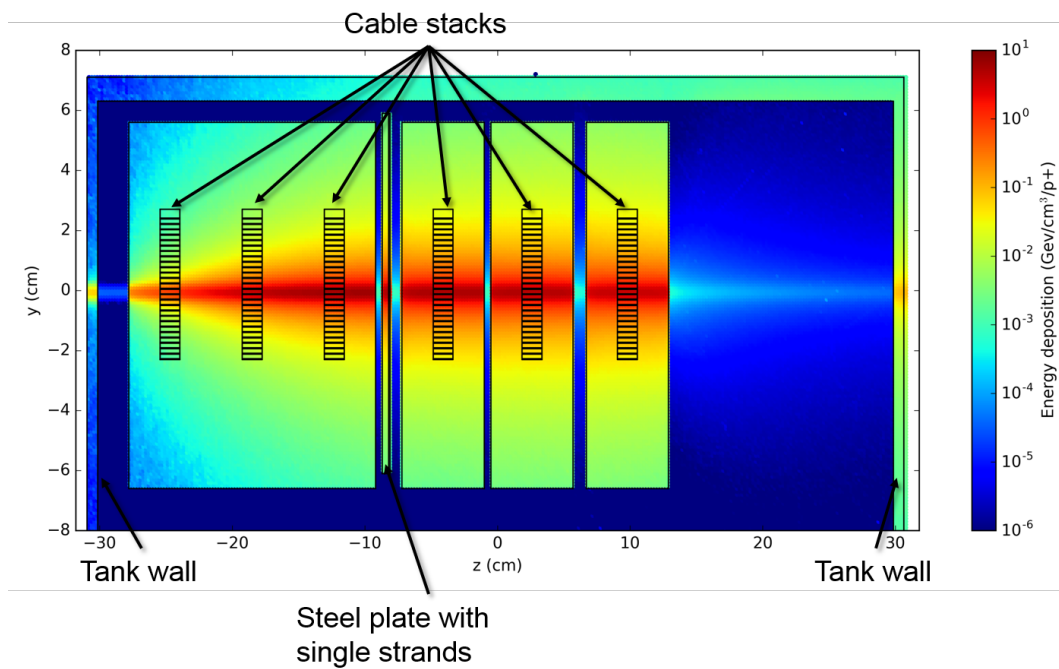


Figure C.1: Energy deposition per proton along the beam axis induced by a 440 GeV proton beam with a $1 \sigma_{r.m.s.}$ transverse size of 1 mm in the experimental set-up. The beam is coming from the left through the tank front wall, travelling through the three first cable stacks with their steel moulds, the steel plate with the superconducting strands and the three last cable stacks, to finally exit the tanks by its back wall. The lower-half of the set-up with six other cable stacks and a steel plate with the strands is not shown as the energy deposition is negligible.

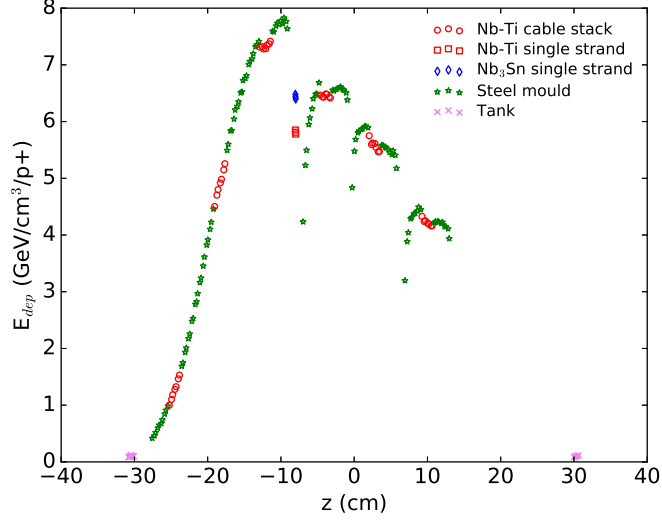


Figure C.2: Peak energy deposition per proton along the beam axis in the cable stacks, the steel moulds, the single superconducting strands and the aluminium tank walls. The peak energy deposition increases until the third stack and then decreases. For strands with the same vertical and longitudinal position, the energy deposition is higher in the Nb₃Sn strand than in Nb-Ti ones because they have a higher density.

ratio is dependent on the type of the targeted strand (Nb₃Sn or Nb-Ti). The expected peak temperatures as function of the longitudinal position of the cable stacks, the single strands and the tank walls for the three chosen pulse intensities (6×10^{11} , 1.3×10^{12} , 2.6×10^{12} protons) are shown in Fig. C.3.

The vertical transverse profile of the energy deposition per proton normalized to its maximum in each sample along the beam axis as obtained from FLUKA is shown in Fig. C.4. The width of the normalized energy deposition is increasing as the beam travel through the set-up. At 5.2 mm away from the beam axis (distance between two beam pulse), the energy deposition in the cable stack 1 is less than 5% of its maximum, in the cable stack 3 is about 10% and in the cable stack 6 is about 16.5%. In other words the impact of 2.6×10^{12} protons on cable stacks 3 and 6 induced a temperature rise along the beam axis up to about 1000 K and 750 K respectively. While the temperature rise 5.2 mm away from the beam axis is about 370 K in both stacks.

C. APPENDIX: ENERGY DEPOSITION SIMULATION FOR THE BEAM EXPERIMENT

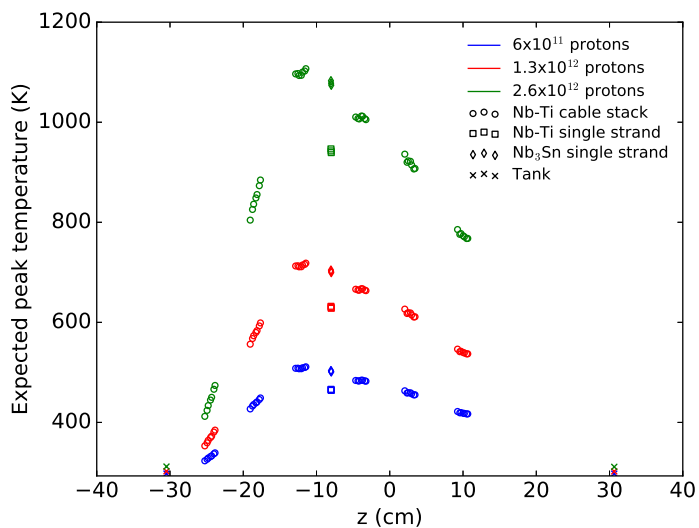


Figure C.3: Expected peak temperature for the three chosen pulse intensities along the beam axis in the cable stacks, the single superconducting strands and the aluminium tank walls. The pulse intensities are 6×10^{11} (blue), 1.3×10^{12} (red), 2.6×10^{12} protons (green). The $1 \sigma_{r.m.s.}$ vertical and horizontal transverse beam size is 1 mm. For the three pulse intensities, the peak temperature increases until the third stack and then decreases. For strands with the same vertical and longitudinal position, the temperature is higher in the Nb₃Sn strand than in Nb-Ti ones because they have a higher density and a smaller heat capacity.

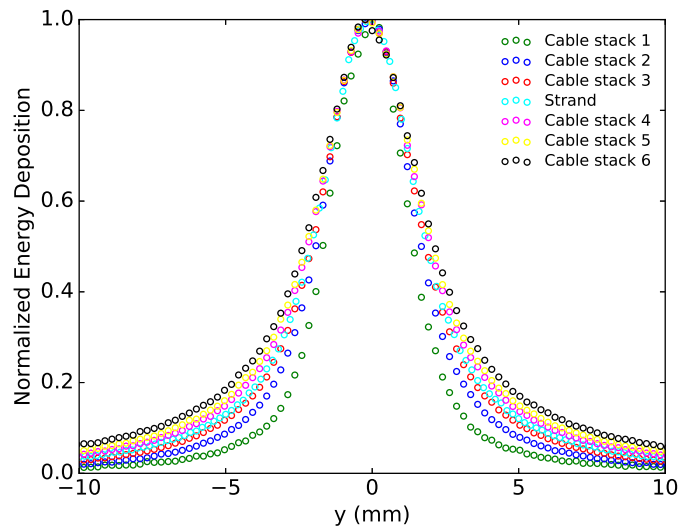


Figure C.4: Vertical profile of the energy deposition per proton normalized to its maximum in each sample along the beam axis as obtained from FLUKA simulation with a 440 GeV proton beam with a $1 \sigma_{r.m.s.}$ transverse size of 1 mm. The width of the normalized energy deposition is increasing as the beam travels through the setup from the cable stack 1 (green) to the cable stack 6 (black).

**C. APPENDIX: ENERGY DEPOSITION SIMULATION FOR THE
BEAM EXPERIMENT**

Appendix D

Appendix: Relation between relative resistance variation of a strand and its energy deposition profile

In the beam experiment (see 6.4) to determine the peak temperature reached in the strand, the relation between the relative resistance variation $\frac{\Delta R}{R_i}$ of a strand with a vertical position y_s to its profile of energy deposition $E(x, y)$ was used. This relation is described in the following steps:

- For each strand, $\frac{\Delta R}{R_i}$ can be expressed as function of the strand average resistivity before the beam impact ρ_0 and at the time of the beam impact ρ_s .

$$\frac{\Delta R}{R_i}(y_s) = \frac{\rho_s - \rho_0}{\rho_0} \quad (\text{D.1})$$

where ρ_0 is the resistivity of copper at room temperature.

- The resistivity of the strand at the beam impact time is equal to:

$$\rho_s = \frac{1}{V_s} \int_{L_s/2}^{L_s/2} dx \int_{y_s-R_s}^{y_s+R_s} \rho_{Cu}(x, y) dy \int_{-\sqrt{R_s^2-(y-y_s)^2}}^{\sqrt{R_s^2-(y-y_s)^2}} dz \quad (\text{D.2})$$

where V_s , L_s and R_s are the strand volume, length and radius and $\rho_{Cu}(x, y)$ the copper resistivity at the position (x, y) in the strand.

D. APPENDIX: RELATION BETWEEN RELATIVE RESISTANCE VARIATION OF A STRAND AND ITS ENERGY DEPOSITION PROFILE

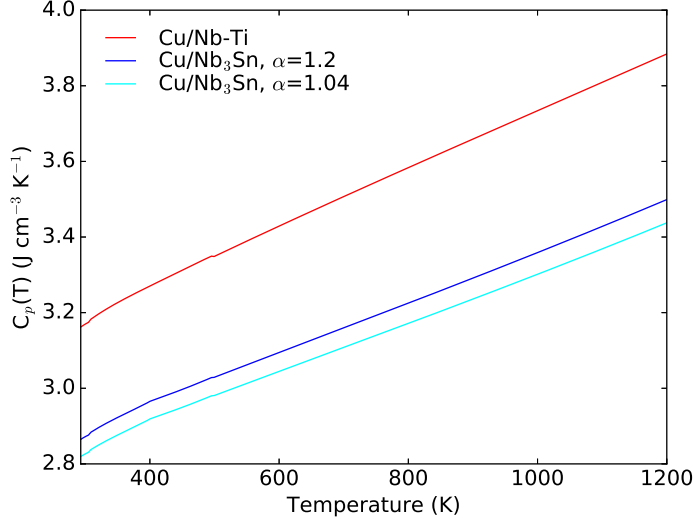


Figure D.1: Heat capacity as function of temperature of the Nb-Ti cables and strands (Cu/Nb-Ti) and two types of Nb₃Sn strands with different copper to superconductor ratio α (Cu/Nb₃Sn, $\alpha=1.2$ and Cu/Nb₃Sn, $\alpha=1.04$). The heat capacity of the superconducting strands and cables were obtained via the equation D.3 using the heat capacity of copper, Nb-Ti and Nb₃Sn [75].

- Using the temperature dependence of the copper resistivity (see equation 6.2) and the heat capacity of the strands (see equation D.3), the energy deposition $E(x, y)$ can be derived from the $\rho_{Cu}(x, y)$.

The heat capacity of the superconducting strands and of the cables was obtained with:

$$C_p(T) = (\alpha C_{pCu}(T) + C_{pSC}(T))/(1 + \alpha) \quad (D.3)$$

where α is the copper to superconductor ratio and C_{pCu} and C_{pSC} are the heat capacities of the copper and of the superconducting material, Nb-Ti and Nb₃Sn respectively. Fig. D.1 shows the C_p as function of temperature for the Nb-Ti cables and strands (Cu/Nb-Ti) and for the two types of Nb₃Sn strands (Cu/Nb₃Sn, $\alpha=1.2$ and Cu/Nb₃Sn, $\alpha=1.04$).

Appendix E

Appendix: Glossary

ALICE	A Large Ion Collider Experiment	MKD	LHC Magnet Kicker Dump
ATLAS	A Large Toroidal LHC Apparatus	MKI	LHC Magnet Kicker Injection
CMS	Compact Muon Solenoid	MPS	Machine Protection System
BCT	Beam Current Transformer	MQ	LHC Main Quadrupole magnet
BIS	Beam Interlock System	MQM	LHC Dispersion suppressor and matching section quadrupole magnet
BLM	Beam Loss Monitoring system	MQX	LHC Low beta insertion quadrupole
BPM	Beam Position Monitor	MQY	LHC Magnet Quadrupole wide aperture
BSE	Back-Scattered Electron	MSI	LHC Magnet Septum Injection
BTV	Beam Television	MSD	LHC Magnet Septum Dump
CLIQ	Coupling Loss Induced Quench	OFHC	Oxygen-Free High-Conductivity
DAQ	Data Acquisition	PIT	Powder In Tube process
EDX	Energy Dispersive X-ray spectrometry	PS	Proton Synchrotron
FCC	Futur Circular Collider	QPS	Quench Protection System
FMCM	Fast Magnet Current change Monitors	RRP	Restacked Rod Process
HE-LHC	High Energy LHC	SEM	Scanning Electron Microscope
HL-LHC	High Luminosity LHC	SPS	Super Proton Synchrotron
IP	Interaction Point in the LHC ring	SQUID	Superconducting QUantum Interference Device
IR	Interaction Region in the LHC ring	TVS	Voltage Suppressor Diodes
IT	Internal Tin process	TCDS	LHC extraction absorber protecting the extraction septum magnets
LBDS	LHC Beam Dumping System	TCDQ	LHC extraction absorber protecting quadrupole magnets
LEIR	Low Energy Ion Ring	TDI	LHC Injection beam absorber
LHC	Large Hadron Collider	VSM	Vibrating Sample Magnetometer
LHC-b	LHC beauty - an experiment of the LHC	UFO	Unidentified Falling Object
LINAC	LInear ACcelerator		
LIU	LHC Injector Upgrade project		
MB	LHC Main Bending magnet		

E. APPENDIX: GLOSSARY

References

- [1] R. SCHMIDT, R. ASSMANN, E. CARLIER, B. DEHNING, R. DENZ, B. GODDARD, E.B. HOLZER, V. KAIN, B. PUCCIO, B. TODD, ET AL. **Protection of the CERN Large Hadron Collider**. *New Journal of Physics*, **8**(11):290, 2006. 1, 11, 12, 50
- [2] F. BURKART. *Expected damage to accelerator equipment due to the impact of the full LHC beam: Beam instrumentation, experiments and simulations*. PhD thesis, CERN, 2016. 1
- [3] A. LECHNER, C. BRACCO, V. VLACHOUDIS, A. ALNUAIMI, F. CERUTTI, L.S. ESPOSITO, A. CHRISTOV, AND N.V. SHETTY. **Energy deposition studies for fast losses during LHC injection failures**. In *Conf. Proc. IPAC'13, Shanghai, China, TUPFI027*, 2013. 2, 15
- [4] A. LECHNER, C. BRACCO, F. MACIARIELLO, N.V. SHETTY, F. VELOTTI, A. PERILLO MARCONE, G. STEELE, J. UYTHOVEN, B. GODDARD, AND M. BARNES. **Protection of superconducting magnets in case of accidental beam losses during HL-LHC injection**. In *Conf. Proc. IPAC'15, Richmond, VA, USA, TUPTY049*, 2015. 2, 15
- [5] B. AUCHMANN, G. STEELE, AND A. VERWEIJ. **Quench and damage levels for Q4 and Q5 magnets near Point 6**. Technical report, EDMS 1355063, CERN, 2014. 2, 16
- [6] O. BRÜNING, P. COLLIER, P. LEBRUN, S. MYERS, R. OSTOJIC, J. POOLE, AND P. PROUDLOCK. **LHC design report vol. 1**. Technical report, CERN, Geneva, Switzerland, 2004. 5, 8, 45, 47, 48
- [7] ATLAS COLLABORATION ET AL. **Observation of a new particle in the search for the Standard Model Higgs boson with the ATLAS detector at the LHC**. *arXiv preprint arXiv:1207.7214*, 2012. 5
- [8] CMS COLLABORATION ET AL. **Observation of a new boson at a mass of 125 GeV with the CMS experiment at the LHC**. *Physics Letters B*, **716**(1):30–61, 2012. 5
- [9] T. BÄR. *Very fast losses of the circulating LHC beam, their mitigation and machine protection*. PhD thesis, Universität Hamburg, 2014. 8
- [10] T. ARGYROPOULOS. **LHC operation: experience and new tools**. In *Proceedings of the 2017 8th LHC operations Evian Workshop*, 2018. 8
- [11] L. ROSSI O. BRÜNING. *The High Luminosity Large Hadron Collider: the new machine for illumination the mysteries of the universe*. World Scientific, 2015. 8, 9
- [12] A.L. MACPHERSON. **LHC Availability and performance in 2012**. In *Proceedings of the 2012 Evian workshop on LHC beam operation*, 2013. 8
- [13] M. SOLFAROLI. **2017 Operation**. In *Proceedings of the 2018 Chamonix Workshop on LHC Performance*, 2018. 8

REFERENCES

- [14] J. COUPARD, H. DAMERAU, A. FUNKEN, S. GILARDONI, B. GODDARD, K. HANKE, A. LOMBARDI, I. KOBZEVA, D. MANGLUNKI, S. MATAGUEZ, M. MEDDAHI, B. MIKULEC, R. SCRIVENS, G. RUMOLO, E. SHAPSHNIKOVA, AND M. VRETENAR. **LHC Injectors Upgrade, Technical Design Report**. Technical report, CERN, 2014. 9
- [15] G. APOLLINARI, I. BÉJAR ALONSO, O. BRÜNING, M. LAMONT, AND L. ROSSI. **High-Luminosity Large Hadron Collider (HL-LHC): preliminary Design Report**. Technical report, Fermi National Accelerator Laboratory (FNAL), Batavia, IL (United States), 2015. 10, 13
- [16] R. ASSMANN, L. ROSSI, F. ZIMMERMANN, O. DOMINGUEZ SANCHEZ, G. DE RIJK, J.M. JIMENEZ, R. BAILEY, O. BRÜNING, L. TAVIAN, E. TODESCO, ET AL. **First thoughts on a higher-energy LHC**. Technical report, CERN, 2010. 9
- [17] E. TODESCO AND F. ZIMMERMANN. **The Higher-Energy Large Hadron Collider**. In *EuCARD-AccNet-EuroLumi Workshop: The High-Energy Large Hadron Collider (HE-LHC10)*, 2010. 9
- [18] M. BENEDIKT. **Future Circular Collider study**. Technical report, FCC-DRAFT-MGMT-2016-008, 2014. 9
- [19] F. ZIMMERMANN. **HE-LHC baseline parameters**. FCC Week 2017. 10
- [20] M. BENEDIKT. **Future Circular Collider study, status and plans**. FCC Week 2017. 10
- [21] B. AUCHMANN, T. BÄR, M. BEDNAREK, G. BELLODI, C. BRACCO, R. BRUCE, F. CERUTTI, V. CHETVERTKOVA, B. DEHNING, P.P. GRANIERI, ET AL. **Testing beam-induced quench levels of LHC superconducting magnets**. *Physical Review Special Topics-Accelerators and Beams*, **18**(6):061002, 2015. 12
- [22] O. BRÜNING, P. COLLIER, P. LEBRUN, S. MYERS, R. OSTOJIC, J. POOLE, AND P. PROUDLOCK. **LHC design report vol. 1, powering and protection**. Technical report, CERN, Geneva, Switzerland, 2004. 12
- [23] F. RODRIGUEZ-MATEOS AND F. SONNEMANN. **Quench heater studies for the LHC magnets**. In *Particle Accelerator Conference, 2001. PAC 2001. Proceedings of the 2001*, **5**, pages 3451–3453. IEEE, 2001. 12, 44
- [24] E. RAVAIOLI. *CLIQ. A new quench protection technology for superconducting magnets*. PhD thesis, Universiteit Twente, 2015. 12
- [25] K. DAHLERUP-PETERSEN, A. MEDVEDKO, A. EROKHIN, B. KAZMIN, V. SYTCHEV, AND L. VASSILIEV. **Energy extraction in the CERN Large Hadron Collider: a project overview**. In *Pulsed Power Plasma Science, 2001. PPPS-2001. Digest of Technical Papers*, **2**, pages 1473–1476. IEEE, 2001. 12
- [26] O. BRÜNING, P. COLLIER, P. LEBRUN, S. MYERS, R. OSTOJIC, J. POOLE, AND P. PROUDLOCK. **LHC design report vol. 1, beam cleaning and collimation system**. Technical report, CERN, Geneva, Switzerland, 2004. 12
- [27] O. BRÜNING, P. COLLIER, P. LEBRUN, S. MYERS, R. OSTOJIC, J. POOLE, AND P. PROUDLOCK. **LHC design report vol. 1, insertion magnet**. Technical report, CERN, Geneva, Switzerland, 2004. 12
- [28] V. KAIN. *Machine protection and beam quality during the LHC injection process*. PhD thesis, Universität Wien, 2005. 12
- [29] T. BÄR, F. ZIMMERMANN, V. VLACHOUDIS, C. ZAMANTZAS, J. WENNINGER, A. LECHNER, M.J. BARNES, J. UYTHOVEN, E. NEBOT DEL BUSTO, N. GARREL, ET AL. **UFOs in the LHC: observations, studies and extrapolations**. In *Conf. Proc., New Orleans, Louisiana, USA, THPPP086*, 2012. 12

REFERENCES

- [30] T. BÄR, A. LECHNER, N. GARREL, A. FERRARI, V. KAIN, L. NORDERHAUG DROSDAL, V. VLACHOUDIS, J. WENNINGER, B. VELGHE, C. ZAMANTZAS, ET AL. **UFOs in the LHC after LS1**. In *Proceedings of Chamonix 2012 workshop on LHC Performance*. CERN, 2012. 12
- [31] G. PAPOTTI, E.B. HOLZER, B. AUCHMANN, M. KALLIOKOSKI, A. LECHNER, AND M. ALBERT. **Macroparticle-induced losses during 6.5 TeV LHC operation**. Technical report, CERN, 2016. 12
- [32] B. TODD. *A beam interlock system for CERN high energy accelerators*. PhD thesis, Brunel University, 2006. 13
- [33] O. BRÜNING, P. COLLIER, P. LEBRUN, S. MYERS, R. OSTOJIC, J. POOLE, AND P. PROUDLOCK. **LHC design report vol. 1, beam dumping system**. Technical report, CERN, Geneva, Switzerland, 2004. 13, 16
- [34] M. WERNER, M. ZERLAUTH, R. SCHMIDT, V. KAIN, AND B. GODDARD. **A fast magnet current change monitor for machine protection in HERA and the LHC**. *ICALEPS, Geneva*, 2005. 13
- [35] E. CALVO, C. BOCCARD, D. COCQ, L. JENSEN, R. JONES, J.J. SAVIOZ, D. BISHOP, AND G. WATERS. **The LHC orbit and trajectory system**. *Proceedings DIPAC*, page 187, 2003. 13
- [36] B. DEHNING, E. EFFINGER, J. EMERY, G. FERIOLO, G. GUAGLIO, E.B. HOLZER, D. KRAMER, L. PONCE, V. PRIETO, M. STOCKNER, ET AL. **The LHC beam loss measurement system**. In *Particle Accelerator Conference*, pages 4192–4194. IEEE, 2007. 13
- [37] B. DEHNING, T. BÖHLEN, E. EFFINGER, J. EMERY, F. FOLLIN, E.B. HOLZER, S. JACKSON, D. KRAMER, G. KRUK, P. LE ROUX, ET AL. **First Experience with the LHC beam loss monitoring system**. In *Particle Accelerator Conference, TH5RFP034*, 2009. 13
- [38] O. BRÜNING, P. COLLIER, P. LEBRUN, S. MYERS, R. OSTOJIC, J. POOLE, AND P. PROUDLOCK. **LHC design report vol. 1, injection system**. Technical report, CERN, Geneva, Switzerland, 2004. 15
- [39] J. UYTHOVEN, J. HRIVNAK, F. MACIARIELLO, A. MEREGHETTI, A. PERILLO MARCONE, G. STEELE, B. GODDARD, N.V. SHETTY, AND M. BARNES. **Upgrades to the LHC injection and beam dumping systems for the HL-LHC project**. In *Conf. Proc. IPAC2014, Dresden, Germany, MOPRO032*, 2014. 15
- [40] W. WETERINGS, T. ANTONAKAKIS, C. MAGLIONI, B. BALHAN, B. GODDARD, R. VERSACI, AND J. BORBURGH. **Upgrade of the LHC beam dumping protection elements**. In *Conf. Proc. Conf. Proc. IPAC2012, New Orleans, USA, MOPPD081*, 2012. 16
- [41] A. FERRARI AND P. SALA. **Physics of showers induced by accelerator beams**. In *Proceedings of the 1995 Frederic Joliot Summer School in Reactor Physics, August*, pages 22–30, 1995. 18
- [42] W. FRASS. **Passage of particles through matter**. Technical report, University of Oxford, Departement of Physics, 2009. 18, 20, 21
- [43] C. PATRIGNANI, PARTICLE DATA GROUP, ET AL. **Review of particle physics**. *Chinese physics C*, **40**(10):100001, 2016. 20, 21, 22, 23, 24
- [44] T.T. BÖHLEN, F. CERUTTI, M.P.W. CHIN, A. FASSÒ, A. FERRARI, P.G. ORTEGA, A. MAIRANI, R. SALA, G. SMIRNOV, AND V. VLACHOUDIS. **The FLUKA code: developments and challenges for high energy and medical applications**. *Nuclear Data Sheets*, **120**:211–214, 2014. 23, 24
- [45] A. FERRARI, R. SALA, A. FASSO, AND J. RANFT. **FLUKA: a multi-particle transport code (Program version 2005)**. Technical report, CERN, 2005. 23, 24

REFERENCES

- [46] **The official FLUKA site**, <http://www.fluka.org/>. 23, 24
- [47] S. ROESLER, R. ENGEL, AND J. RANFT. **The monte carlo event generator DPMJET-III**. In *Advanced Monte Carlo for Radiation Physics, Particle Transport Simulation and Applications*, pages 1033–1038. Springer, 2001. 24
- [48] B. GODDARD, V. MERTENS, J. WENNINGER, V. KAIN, AND J. UYTHOVEN. **TT40 damage during 2004 high intensity SPS extraction**. Technical report, CERN, 2005. 25
- [49] R. SCHMIDT, J. BLANCO SANCHO, F. BURKART, D. GRENIER, D. WOLLMANN, N.A. TAHIR, A. SHUTOV, AND A.R. PIRIZ. **First experimental evidence of hydrodynamic tunneling of ultra-relativistic protons in extended solid copper target at the CERN HiRadMat facility**. *Physics of Plasmas*, **21**(8):080701, 2014. 25, 75
- [50] F. BURKART, R. SCHMIDT, V. RAGINEL, D. WOLLMANN, N.A. TAHIR, A. SHUTOV, AND A.R. PIRIZ. **Analysis of 440 GeV proton beam-matter interaction experiments at the High Radiation Materials test facility at CERN**. *Journal of Applied Physics*, **118**(5):055902, 2015. 26, 75
- [51] P. SIEVERS. **Elastic stress waves in matter due to rapid heating by an intense high-energy particle beam**. *LAB. II/BT/74-2*, CERN, 1974. 27
- [52] W. KALBREIER, W.C. MIDDELKOOP, AND P. SIEVERS. **External targets at the SPS**. Technical report, SIS-74-1266, 1974. 27
- [53] H. BARGMANN. **Dynamic response of external targets under thermal shock**. *CERN Technical Note No. LAB II/ BT/ Int*, pages 73–3, 1973. 27
- [54] A. BERTARELLI, A. DALLOCCHIO, AND T. KURTYKA. **Dynamic response of rapidly heated cylindrical rods: longitudinal and flexural behavior**. *Journal of Applied Mechanics*, **75**(3):031010, 2008. 27
- [55] A. DALLOCCHIO. *Study of thermo-mechanical effects induced in solids by high energy particle beams: analytical and numerical methods*. PhD thesis, Turin Polytechnic, 2008. 27
- [56] A. BERTARELLI, E. BERTHOME, V. BOCCONE, F. CARRA, F. CERUTTI, N. CHARITONIDIS, C. CHAR-RONDIERE, A. DALLOCCHIO, P. CARMONA FERNANDEZ, P. FRANCON, ET AL. **An experiment to test advanced materials impacted by intense proton pulses at CERN HiRadMat facility**. *Nuclear Instruments and Methods in Physics Research Section B: Beam Interactions with Materials and Atoms*, **308**:88–99, 2013. 27, 75
- [57] A. BERTARELLI, F. CARRA, F. CERUTTI, A. DALLOCCHIO, M. GARLASCHE, M. GUINCHARD, N. MARIANI, S.D. DOS SANTOS MARQUES, L. PERONI, M. SCAPIN, ET AL. **Behaviour of advanced materials impacted by high energy particle beams**. In *Journal of Physics: Conference Series*, **451**, page 012005. IOP Publishing, 2013. 27
- [58] A. BERTARELLI. **Beam-induced damage mechanisms and their calculation**. *arXiv preprint arXiv:1608.03056*, 2016. 27
- [59] S. FONER AND B. SCHWARTZ. *Superconductor materials science: metallurgy, fabrication, and applications*, **68**. Springer Science & Business Media, 2012. 29, 33
- [60] H. KAMERLINGH ONNES. **Communications Leiden 120b**. Technical report, Royal Netherlands Academy, 1911. 29
- [61] W. MEISSNER AND R. OCHSENFELD. **Ein neuer effekt bei eintritt der supraleitfähigkeit**. *Naturwissenschaften*, **21**(44):787–788, 1933. 29

REFERENCES

- [62] K. OSAMURA. *Composite superconductors*, **3**. CRC Press, 1993. 30, 32, 39, 55
- [63] M.T. NAUS. *Optimization of internal-Sn Nb₃Sn composites*. PhD thesis, University of Wisconsin, 2002. 30, 40, 43
- [64] V.L. GINZBURG AND L.D. LANDAU. **Phenomenological theory**. *J. Exp. Theor. Phys. USSR*, **20**:1064, 1950. 31
- [65] R. KLEINER W. BUCKLE. *Superconductivity*. Wiley-VCH, 2004. 31
- [66] H. WADA, K. ITOH, K. TACHIKAWA, Y. YAMADA, AND S. MURASE. **Enhanced high-field current carrying capacities and pinning behavior of NbTi-based superconducting alloys**. *Journal of Applied Physics*, **57**(9):4415–4420, 1985. 32, 37, 39
- [67] L. BOTTURA. **A practical fit for the critical surface of NbTi**. *IEEE Transactions on Applied Superconductivity*, **10**(1):1054–1057, 2000. 32, 36, 100
- [68] E.J. KRAMER. **Scaling laws for flux pinning in hard superconductors**. *Journal of Applied Physics*, **44**(3):1360–1370, 1973. 32, 116
- [69] M. LUBELL. **Empirical scaling formulas for critical current and critical field for commercial NbTi**. *IEEE Transactions on Magnetics*, **19**(3):754–757, 1983. 32
- [70] A. GODEKE, B. TEN HAKEN, H.H. TEN KATE, AND D.C. LARBALESTIER. **A general scaling relation for the critical current density in Nb₃Sn**. *Superconductor Science and Technology*, **19**(10):R100, 2006. 32
- [71] A. DEVRED. **Practical low-temperature superconductors for electromagnets**. Technical Report CERN-2004-006, CERN, 2004. 33, 34
- [72] C.P. BEAN. **Magnetization of hard superconductors**. *Physical Review Letters*, **8**(6):250, 1962. 33
- [73] T. BOUTBOUL, S. LE NAOUR, D. LEROY, L. OBERLI, AND V. PREVITALI. **Critical current density in superconducting Nb-Ti strands in the 100 mT to 11 T applied field range**. *IEEE Transactions on Applied Superconductivity*, **16**(2):1184–1187, 2006. 34, 73
- [74] B. BORDINI, D. RICHTER, P. ALKNES, A. BALLARINO, L. BOTTURA, AND L. OBERLI. **Magnetization measurements of high-Jc Nb₃Sn strands**. *IEEE Transactions on Applied Superconductivity*, **23**(3):7100806–7100806, 2013. 34, 73
- [75] G. MANFREDA. **Review of ROXIE’s material properties database for quench simulation**. *TE Technology department internal note*, **35**, 2011. 36, 68, 88, 148
- [76] J.K. HULM AND R.D. BLAUGHER. **Superconducting solid solution alloys of the transition elements**. *Physical Review*, **123**(5):1569, 1961. 36
- [77] P.J. LEE AND D.C. LARBALESTIER. **Niobium-Titanium superconducting wires: nanostructures by extrusion and wire drawing**. *Wire Journal International(USA)*, **36**(2):61–66, 2003. 36, 37, 38
- [78] P.J. LEE. **Abridged metallurgy of ductile alloy superconductors**. *Wiley Encyclopedia of Electrical and Electronics Engineering*, **21**:75–87, 1999. 37
- [79] B.T. MATTHIAS, T.H. GEBALLE, S. GELLER, AND E. CORENZWIT. **Superconductivity of Nb₃Sn**. *Physical Review*, **95**(6):1435, 1954. 37

REFERENCES

- [80] A. GODEKE, M. JEWELL, C. FISCHER, A. SQUITIERI, P.J. LEE, AND D.C. LARBALESTIER. **The upper critical field of filamentary Nb₃Sn conductors.** *Journal of Applied Physics*, **97**(9):093909, 2005. 40, 116
- [81] A. GODEKE. **A review of the properties of Nb₃Sn and their variation with A15 composition, morphology and strain state.** *Superconductor Science and Technology*, **19**(8):R68, 2006. 41, 56, 126, 128, 129
- [82] L.D. COOLEY, P.J. LEE, AND D.C. LARBALESTIER. **Changes in flux pinning curve shape for flux-line separations comparable to grain size in Nb₃Sn wires.** In *AIP Conference Proceedings*, **614**, pages 925–932. AIP, 2002. 42
- [83] C. SANABRIA. *A new understanding of the heat treatment of Nb-Sn superconducting wires.* PhD thesis, The Florida State University, 2017. 40, 126
- [84] R. OSTOJIC. **The LHC insertion magnets.** *IEEE Transactions on Applied Superconductivity*, **12**(1):196–201, 2002. 45
- [85] P. FESSIA, P.P. GRANIERI, S. LUZIEUX, D. TOMMASINI, A. GERARDIN, M. GUINCHARD, F. REGIS, S. SGOBBA, AND A. ZAGHLOUL. **Electrical and mechanical performance of an enhanced cable insulation scheme for superconducting magnets.** *IEEE Transactions on Applied Superconductivity*, **20**(3):1622–1625, 2010. 48, 92
- [86] A. IJSPEERT, M. ALLITT, A. HILAIRE, M. KARPPINEN, J. MAZET, J. PEREZ, J. SALMINEN, M. KARMARKER, AND A. PUNTAMBEKAR. **Principles developed for the construction of the high performance, low-cost superconducting LHC corrector magnets.** *IEEE Transactions on Applied Superconductivity*, **12**(1):90–93, 2002. 48
- [87] J. SALMINEN, A. IJSPEERT, AND A. PUNTAMBEKAR. **Superconducting sextupole corrector magnet for the LHC main dipoles.** Technical report, CERN, 1996. 48
- [88] F. SAVARY, E. BARZI, B. BORDINI, L. BOTTURA, G. CHLACHIDZE, D. RAMOS, S. BERMUDEZ IZQUIERDO, M. KARPPINEN, F. LACKNER, C.H. LÖFFLER, ET AL. **The 11 T dipole for HL-LHC: status and plan.** *IEEE Transactions on Applied Superconductivity*, **26**(4):1–5, 2016. 49
- [89] L. BOTTURA, G. DE RIJK, L. ROSSI, AND E. TODESCO. **Advanced accelerator magnets for upgrading the LHC.** *IEEE Transactions on Applied Superconductivity*, **22**(3):4002008–4002008, 2012. 49
- [90] T. SEIDL, W. ENSINGER, R. LOPEZ, D. TOMMASINI, E. FLOCH, E. MUSTAFIN, A. PLOTNIKOV, D. SEVERIN, C. TRAUTMANN, A. GOBULEV, ET AL. **Radiation hardness of insulating components for the new heavy-ion accelerator facility.** *Proceedings of HB*, 2010. 51
- [91] H. TSUBAKIHARA, T. OKADA, T. SUITA, T. HORIUCHI, K. MATSUMOTO, AND S. TSURUTANI. **Neutron irradiation effects on superconducting Nb-Ti wires for fusion reactor.** *Teion Kogaku (Journal of Cryogenics and Superconductivity Society of Japan)*, **9**(5):221–227, 1974. 51
- [92] W.V. HASSENZAHL, J.D. ROGERS, AND W.C. ARMSTRONG. **The effects of radiation on superconducting Nb-Ti wire.** *IEEE Transactions on Nuclear Science*, **18**(3):683–684, 1971. 51
- [93] F. WEISS, R. FLÜKIGER, W. MAURER, P. HAHN, AND M. GUINAN. **Changes in superconducting properties by room temperature neutron irradiation for binary and alloyed Nb₃Sn multifilamentary wires.** *IEEE Transactions on Magnetics*, **23**(2):976–979, 1987. 51
- [94] T. BAUMGARTNER, M. EISTERER, H.W. WEBER, R. FLÜKIGER, C. SCHEUERLEIN, AND L. BOTTURA. **Performance boost in industrial multifilamentary Nb₃Sn wires due to radiation induced pinning centers.** *Scientific reports*, **5**, 2015. 51

REFERENCES

- [95] T. SPINA, C. SCHEUERLEIN, D. RICHTER, L. BOTTURA, A. BALLARINO, AND R. FLÜKIGER. **Critical current density of Nb₃Sn wires after irradiation with 65 MeV and 24 GeV protons.** In *Journal of Physics: Conference series*, **507**, page 022035. IOP Publishing, 2014. 52
- [96] DUPONT DATASHEET. **Dupont TM, Kapton R.** 52, 53
- [97] N. ARNOLD AND N. BITYURIN. **Model for laser-induced thermal degradation and ablation of polymers.** *Applied Physics A*, **68**(6):615–625, 1999. 52
- [98] R. SRINIVASAN, R.R. HALL, W.D. LOEHLE, W.D. WILSON, AND D.C. ALLBEE. **Chemical transformations of the polyimide Kapton brought about by ultraviolet laser radiation.** *Journal of applied physics*, **78**(8):4881–4887, 1995. 52, 91
- [99] S. HELTZEL AND C. SEMPRIMOSCHNIG. **A detailed study on the thermal endurance of kapton HN® i and Upilex S®.** *High Performance Polymers*, **16**(2):235–248, 2004. 52
- [100] N. REGNIER AND C. GUIBE. **Methodology for multistage degradation of polyimide polymer.** *Polymer degradation and stability*, **55**(2):165–172, 1997. 52
- [101] C. SCHEUERLEIN, I. PONG, C. SENATORE, M. DI MICHIEL, L. THILLY, A. GERARDIN, B. REHMER, L. OBERLI, G. WILLERING, AND L. BOTTURA. **Temperature induced degradation of Nb-Ti/Cu composite superconductors.** In *Journal of Physics: Conference Series*, **234**, page 022031. IOP Publishing, 2010. 54, 105, 109
- [102] B. TEN HAKEN. *Strain effects on the critical properties of high-field superconductors.* PhD thesis, University of Twente, Netherlands, 1994. 55
- [103] J.W. EKIN, F.R. FICKETT, AND A.F. CLARK. **Effect of stress on the critical current of NbTi multifilamentary composite wire.** In *Advances in Cryogenic Engineering*, pages 449–452. Springer, 1977. 55
- [104] J.W. EKIN. **Mechanisms for critical-current degradation in NbTi and Nb₃Sn multifilamentary wires.** *IEEE Transactions on Magnetics*, **13**(1):127–130, 1977. 55, 56
- [105] B. TEN HAKEN, A. GODEKE, AND H.H. TEN KATE. **The influence of compressive and tensile axial strain on the critical properties of Nb₃Sn conductors.** *IEEE Transactions on Applied Superconductivity*, **5**(2):1909–1912, 1995. 57, 129
- [106] N. CHEGGOUR, L.F. GOODRICH, T.C. STAUFFER, J.D. SPLETT, X.F. LU, A.K. GHOSH, AND G. AMBROSIO. **Influence of Ti and Ta doping on the irreversible strain limit of ternary Nb₃Sn superconducting wires made by the restacked-rod process.** *Superconductor Science and Technology*, **23**(5):052002, 2010. 56
- [107] K. COUTURIER, P. FERRACIN, W. SCANDALE, E. TODESCO, AND D. TOMMASINI. **Thermomechanical properties of the coil of the superconducting magnets for the Large Hadron Collider.** *IEEE Transactions on Applied Superconductivity*, **12**(2):1804–1812, 2002. 60
- [108] SCHNEIDER ELECTRIC. *Current Transformer METSECT5VV600.* 67
- [109] R.A. MATULA. **Electrical resistivity of copper, gold, palladium, and silver.** *Journal of Physical and Chemical Reference Data*, **8**(4):1147–1298, 1979. 68
- [110] I. EFTHYMIPOULOS, D. GRENIER, M. MEDDAHI, P. TRILHE, S. EVRARD, H. VINCKE, C. THEIS, N. CHARITONIDIS, C. HESSLER, A. PARDONS, ET AL. **HiRadMat: a new irradiation facility for material testing at CERN.** *IPAC'11*, 2011. 75

REFERENCES

- [111] S. EVRARD ET AL. **HiRadMat safety file - descriptive part, EDMS 1145711, 20011**. Technical report, CERN, 2011. 75
- [112] C.L. TORREGROSA MARTIN, E. FORNASIERE, L. GENTINI, M. BUTCHER, M. CALVIANI, A. PERILLO MARCONE, AND D. HORVATH. **The HRMT27 (Rodtarg) experiment: design, operation and first results**. Technical report, CERN, 2016. 75
- [113] C. HESSLER A. FABICH. **HiRadMat beam parameters, EDMS 1054880**. Technical report, CERN, 2010. 75
- [114] RUUKKI. **Aluminium AW 6082 T6 round**. 78
- [115] AALCO (R). **Aluminium Alloy 6082 - T6 T651 Plate datasheet**. 78
- [116] PFEIFFER VACCUM. **Data sheet : Dust filter DFT 25**. 80
- [117] D.L. MOFFAT AND U.R. KATTNER. **The stable and metastable Ti-Nb phase diagrams**. *Metallurgical and Materials Transactions A*, **19**(10):2389–2397, 1988. 114
- [118] M.G.T. MENTINK, J.E. BONEVICH, M.M.J. DHALLE, D.R. DIETDERICH, A. GODEKE, F. HELLMAN, AND H.H. TEN KATE. **Superconductivity in Nb-Sn thin films of stoichiometric and off-stoichiometric compositions**. *IEEE Transactions on Applied Superconductivity*, **23**(3), 2013. 126, 129
- [119] B.J. SHAW. **Grain size and film thickness of Nb₃Sn formed by solid-state diffusion in the range 650–800 C**. *Journal of Applied Physics*, **47**(5):2143–2145, 1976. 128
- [120] J.W. EKIN. **Effect of transverse compressive stress on the critical current and upper critical field of Nb₃Sn**. *Journal of applied physics*, **62**(12):4829–4834, 1987. 129